



Compendium solar spectrum formation*

Robert J. Rutten^{1,2,3}

* In honor of C. (Kees) de Jager on his 100th birthday

¹ Lingezicht Astrophysics, Deil, The Netherlands

² Institute of Theoretical Astrophysics, University in Oslo, Oslo, Norway

³ Rosseland Centre for Solar Physics, University in Oslo, Oslo, Norway

*Myself when young did eagerly frequent
doctor and saint, and heard great argument
about it and about; but evermore
came out by the same door as in I went.*

Omar Khayyam (1048–1131)

Abstract. The solar spectrum conveys most of our diagnostics to find out how our star works. They must be understood for utilization but solar spectrum formation is complex because the interaction of matter and radiation within the solar atmosphere suffers non-local control in space, wavelength, and time. These complexities are summarized and illustrated with classic literature.

Contents

1	Preamble: format and on-line material	2	44	strong-line $B(\tau)$ flattening
2	Introduction	3	46	epsilon is small
3	RT basics	5	47	no Thomas photoelectric control
	Intensity	5	66	population departure coefficients
	Matter–radiation interactions	5	69	Menzel population departure coefficients
	Bound-bound, bound-free, free-free interactions	6	60	spectral interlocking
	Pair combinations	6	91	coronium, nebulium, Zanstra mechanism
	Equilibria	6	48	coronal clouds
	Bound-bound redistribution	8	49	sophisticated clouds
	Bound-free redistribution	9	65	RE upper photosphere
	Free-free redistribution	9	54	classic abundance determination
	Thomson and Rayleigh scattering	9	58	NLTE masking
	Extinction and emissivity	9	64	line haze modeling
	Emission measure	10	66	ALC7 line formation plots
	Source function	10	76	Ha–Ha scattering
	Line source function	10	71	Carlsson-Stein internetwork shocks
	Transfer equation along the beam	11	80	internetwork shocks in Ca II H and H α
	Transfer equation in optical depth	12	73	bright-point shifts 1600–1700 Å
4	LTE: Holweger models	13	84	non-E quiet chromosphere
5	NLS: Auer & Mihalas modeling	14	85	spicules-II, RBEs, RREs
6	NLS+NLW: Avrett stars	14	94	RBE–RRE–fibril ionization-recombination
7	NLS+NLW+NLT: Oslo simulations	18	86	SDO quiet-chromosphere images
	1D HD RADYN simulation	18	88	CBP foot visibility
	2D MHD Stagger simulation	18	84	transition region versus heated chromosphere
	3D MHD Bifrost simulations	19	78	dynamic fibrils
8	NLS–NLW–NLT chromosphere spectrum	19	98	active-region moss
	Quiet chromosphere	19	35	dark EUV features
	Active chromosphere	22	100	around and upward heating
9	Conclusion	25	101	chromospheric FIP fractionation
			99	IBIS–SDO active-region blinker
			103	VAULT-II Ly α limb movies
			104	Ly α features
			106	filament blobs
			75	flash-spectrum color
			61	Fe I 6302 Å polarimetry doublet
			61	Mg I 4571 Å
			34	Ba II 4554 Å
			34	Mn I lines as activity monitor

Detailing notes, roughly grouped

16	stellar classification
75	Schuster-Schwarzschild approximation
59	Milne-Eddington approximation
25	extinction diagrams
29	dielectronic ionization and recombination
31	radiative losses versus heating
43	$\sqrt{\epsilon}$ law

51	Na I D, Mg Ib, Ca II 8542 Å heights
33	Ca II H & K core reversals
33	Wilson-Bappu effect
56	Mg I 12 micron emission lines
60	optical Fe I lines with $S \approx B$
60	weak Ce II and Fe II emission lines
75	He I D ₃ off-limb
90	optical He I lines on-disk
77	Rydberg HI lines
105	Rydberg HI candidate for ALMA
70	quiet-Sun H α scenes
76	quiet-Sun H α – Ca II 8542 Å comparison
102	Ly α dream
23	solar telescopes
27	solar neutrinos
96	Ellerman bombs
89	Solo campfires
72	coronal heating by acoustic or gravity waves
72	$k - \omega$ diagram
74	solar p -mode history
54	Kieler program for LTE spectrum synthesis
64	Pandora program for NLTE spectrum synthesis
52	MULTI program for NLTE spectrum synthesis
68	RH program for NLTE–PRD spectrum synthesis
82	Bifrost program for radiative MHD simulation
30	CHIANTI package for CE analysis
67	my IDL programs
87	SDO co-alignment programs
95	ALMA–GONG–SDO alignment

1. Preamble: format and on-line material

This is a webposted¹ condensed graduate-level course on solar spectrum formation.² For brevity and to avoid repetition I refer much to teaching materials posted on my website³ using hyperlinks and therefore recommend on-screen on-line pdf reading.⁴ This text contains minimal equations and figures because they are linked in page openers. They make this compendium Wikipedia-style multilayer: you may read further and delve deeper selecting linked explanations, detail, references that suit your interest. In addition this is a two-tier text with a relatively straightforward presentation in the main text (contents above) but detailing many specific topics (list above)⁵ with linked literature and even history in extensive labeled notes.⁶ Together, the links and two-tier format invite study at different levels:

¹ Rationale for webpublishing in [LAR-1 epilogue \(pdf 14\)](#).

² Except polarization spectra, radio spectra, neutrino spectra. For polarization [del Toro Iniesta \(2007\)](#) is a good introduction, [Landi Degl'Innocenti & Landolfi \(2004\)](#) the comprehensive bible. In the workshop it was treated by Rohan Eugene Louis and Debi Prasad Choudhary. Radio diagnostics were treated by P.K. Manoharan. Neutrinos are done ([note 27](#)).

³ robrutten.nl

⁴ An off-line or slow-connection alternative is to download these files first, open them in parallel, and use the pdf page number specified in each link. This may especially suit [SSX](#) which is the largest – but it is no good for other weblinks and ADS page and abstract openers.

⁵ Naturally a personal selection favoring cases that I have been involved in and references I knew before because these I remember best and came first to mind in this hurried writeup for the Calicut school.

⁶ Unlabeled notes are just footnotes [my trademark I'm told]. Note [...] is note in note. Without the 100⁺ (foot) notes this text shrinks to half in pages and a third in references.

- read only the main text of [Sect. 3](#) and go through the [SSF](#) equation displays for a theory overview (as I did in my zoom lecturing). The [\[SSX \(pdf 72\)\]](#) ff graphs of spectrum formation in the ALC7 star ([Sect. 6](#)) are suited exercise and self-examination material;
- also read the main text of [Sects. 4–7](#) with [SSX](#) example inspections for an overview of classic developments;
- also study notes and their sources on topics of interest to you;
- read everything (even [Sect. 8](#)) and open each of the 400⁺ display links and study all 250⁺ references for a full-fledged full-semester comprehensive course on solar spectrum formation and underlying solar physics, with this text serving as convenient pointer and page opener;
- when no longer a student but a researcher (doctor or saint) this text may serve as page- and reference-opening resource.

The on-line⁷ teaching material used here amounts to nine files listed and linked at the top of [Table 1](#).⁸ ISSF was a bachelor-level introduction to [Sac Peak](#) summer students in 1993. IART was my Utrecht course for 2nd-year bachelors students written in Dutch in the 1980s, translated by R.C. Peterson in 1992 and revived by L.H.M. Rouppe van der Voort in 2015. It follows [Rybicki & Lightman \(1986\)](#) with most emphasis on explaining their first chapter summarizing basic RT up to NLS treatment. RTSA was initially written in 1995 for my Utrecht masters course, intended as an easier-to-read rehash of [Mihalas \(1970\)](#)⁹ with emphasis on solar NLS \sqrt{e} scattering and adding NLW in particular for solar bound-free continua. The 2003 update (still incomplete) is linked at [ADS](#) and therefore most frequently used – but at Oslo and elsewhere IART is preferred as less-specialist and broader course material. None of these courses includes NLT nor the multi-level detour term in the line source function ([Eq. 2](#) and [Eq. 3](#) below) which lacks even in [Hubený & Mihalas \(2014\)](#). I included them in more recent summary tutorials ([Rutten 2017a](#), [Rutten 2019](#)).

⁷ Most at https://robrutten.nl/Astronomy_course.html but some exercises at <https://robrutten.nl/rweb/rjr-edu/exercises>.

⁸ *Personal background.* I developed this material in decades of teaching at Utrecht University and abroad. In the 1960s I learned solar spectrum formation from [C. \(Kees\) de Jager](#) [presently [near 100](#) the other active solar physicist in The Netherlands]. Our bible was Unsöld's book ([note 62](#)) but NLTE theory had started and was loudly advocated to us by A.B. Underhill, then also professor at Utrecht. The guru was R.N. Thomas but his writings were incomprehensible to me ([note 92](#)). De Jager was much clearer, also for R.M. Bonnet who wrote “*As seen through the writings of Thomas, radiative transfer for me would have remained an unintelligible theoretical exercise forever*” and then acknowledges “*the clarity of Kees' views*” on [page 2 \(pdf 2\)](#) of [Bonnet \(1996\)](#). Jefferies' (1968) book was a great improvement [later scanned by A.V. Sukhorukov and put on ADS by me with Jefferies' consent, enabling page openers below]. I had started on solar radio diagnostics ([Fokker & Rutten 1967](#)) but switched to optical spectrum formation thanks to De Jager's lecturing and then concentrated on the chromosphere thanks to J. Houtgast who took me as junior help to both 1966 eclipses to record the flash spectrum. Half a century and three Saros 142 periods later the chromospheric spectrum still fascinates me, as evident in [Sect. 8](#) which is more a [opinionated] progress report than a course. [C. \(Kees\) Zwaan](#) took over the Utrecht radiative transfer courses in the 1970s and modernized their content; I copied much of his [hand-written Dutch] material when I succeeded him for IART in 1985, for RTSA in 1994. I then also started [teaching abroad](#).

⁹ *Textbooks.* I found [Mihalas \(1970\)](#) easier to read than [Mihalas \(1978\)](#). An inventory of relevant textbooks is in the [\[RTSA Bibliography \(pdf 17\)\]](#). Newer books are [Castor \(2007\)](#) and comprehensive [Hubený & Mihalas \(2014\)](#), both more advanced than this course.

Table 1. Acronyms and abbreviations, roughly grouped.

ISSF = introduction to solar spectrum formation
IART = introduction to astrophysical radiative transfer
RTSA = radiative transfer in stellar atmospheres
SSI = introduction to solar spectrum formation
SSF = solar spectrum formation theory
SSX = solar spectrum formation examples
SSA = stellar spectra A (Cannon – Payne – Minnaert)
SSB = stellar spectra B (Avrett – Chandrasekhar – Unsöld)
SSC = stellar spectra C (Mihalas – Judge – Feautrier)
RT = radiative transfer ~ fermion-boson changes of I_ν
TE = thermodynamic equilibrium ~ detailed balance in all
LTE = local thermodynamic equilibrium ~ SB
NLTE = non-local thermodynamic equilibrium ~ SE
non-E = non-equilibrium ~ no SE
RE = radiative equilibrium ~ $\int \alpha_\nu [S_\nu - J_\nu] d\nu = 0$
SB = Saha-Boltzmann equilibrium ($\rightarrow S_\nu$ equals $B_\nu(T)$)
SE = statistical equilibrium ~ all populations stable
CE = coronal equilibrium ~ SE + thin collisional creation
DEM = differential emission measure ~ CE density part j_ν
EM = emission measure $\equiv \int DEM(T) dT$
NLS = non-local in space ~ J_ν important
NLW = non-local in wavelength ~ other J_ν important
NLT = non-local in time ~ non-SE with memory
CS = coherent scattering ~ monofrequent, monochromatic
CRD = complete redistribution ~ sample extinction profile
PRD = partial redistribution ~ mix CS and CRD
HD = hydrodynamics ~ no magnetism
MHD = magnetohydrodynamics ~ single-fluid HD + B
UV = ultraviolet e.g., AIA 1600 & 1700 Å
EUV = extreme ultraviolet e.g., shorter AIA wavelengths
DOT = Dutch Open Telescope @ La Palma, 0.45 m
SST = Swedish 1-m Solar Telescope @ La Palma, 1 m
DKIST = Daniel K. Inouye Solar Telescope @ Maui, 4 m
SDO = Solar Dynamics Observatory @ space
AIA = Atmospheric Imaging Assembly @ SDO
HMI = Helioseismic & Magnetic Imager @ SDO
IRIS = Interface Region Imaging Spectrograph @ space
MC = small kilogauss magnetic concentration (“fluxtube”)
EB = Ellerman bomb (“burst” may be safer)
RBE = rapid blue-shifted excursion in blue wing H α
RRE = rapid red-shifted excursion in red wing H α
CBP = coronal bright point e.g., in AIA 193 Å

The next three files in [Table 1](#) are sets of projection displays that I use in teaching since the passing of the viewgraph era.¹⁰ SSI is bachelor level, SSF and SSX are masters–graduate level. These also contain newer NLT aspects. I used a selection of these displays¹¹ in my lectures during the workshop.

The final three linked files in [Table 1](#) are practicals. They date back to the 1990s and therefore use IDL but are easily coded in Python. I highly recommend SSA and SSB, designed to accom-

pany IART, for fresh RT students to gain hands-on insights. The third is a practical for RTSA developed by former graduate students that still awaits conversion into proper SSC format.

Here I refer and link to these nine web-posted files for formalisms and equations that otherwise would swamp this summary and instead I discuss issues and add footnoted asides – as I would do in oral 3D bodily-on-the-spot teaching¹² while projecting and discussing the displays and publication pages that you should open and scrutinize yourself here. Square-bracketed hyperlinks¹³ to these files should open the particular page in your browser when you click on them.¹⁴ Similarly, many citations have page links to the pdf on ADS that [should open](#) the cited page. The citations themselves [should open](#) the ADS abstract page.¹⁵

2. Introduction

The solar spectrum caused the dawn of astrophysics in the nineteenth century in the hands of Fraunhofer, Herschel, Kirchhoff and Bunsen, and others. Followed by stellar spectrum classification at Harvard by many ladies but foremost Cannon [[SSF \(pdf 2 ff\)](#)] – I invite you to now do practical [SSA 1.1 \(pdf 5\)](#) before reading further.¹⁶ In the twentieth century stellar spectrum interpretation evolved from basic concepts to understanding with Schwarzschild, Russell, Milne, Eddington, Minnaert, Chandrasekhar and others. Major breakthroughs were Payne’s demonstration with the Saha law that Cannon’s classification represents temperature ordering, the Pannekoek–Wildt–Chandrasekhar identification of H $^-$ as major continuous opacity provider, and Grotrian’s establishing the high temperature of the corona (recognizing its pearly eclipse visibility as Thomson scattering by hot fast electrons and identifying the optical emission lines as Edlén high-ionization transitions of ordinary metals, not coronium). Solar spectrum interpretation went from LTE (Unsöld) to NLTE with Menzel, Hummer, Thomas, Athay, Jefferies, Mihalas, Avrett and others. Then started (M)HD simulation modeling by Nordlund, Schüssler, Stein, Carlsson, Steiner and others with spectral synthesis programs by Carlsson, Uitenbroek, Heinzel, Leenaarts, Pereira and others, presently emphasizing the new frontier of non-E interpretation. ADS serves nearly all these works.

This text gives a brief overview dividing radiative transfer (RT) complexities between nonlocal in space (NLS), nonlocal

¹² I much missed face-to-face contact with the students in this zoom school. Also who-what-where sessions and also social interaction in pub sessions. In past schools and courses I was happy to get to know a sizable fraction of later colleagues.

¹³ Colored blue to also suit dichromats. The suggestion is to click on blue items until you get blue in the face – meaning lack of sub-skin scattering by blood drawn off in brain drain [’tis all scattering here].

¹⁴ With all pdf viewers I use, but some may instead shunt you to the first page. I add the pdf page number to these links for then going to the cited page. You may have to right-click for opening in another window. Acrobat may require undoing security settings disabling the opening of web pages.

¹⁵ Making the reference list superfluous except for silly publishers ([note 72](#)) and to count your name. The references also have ADS links following my [recipe for student reports](#).

¹⁶ *Stellar classification*. This [scissors-only exercise \(pdf 5\)](#) is illuminating. My website shows [photos](#) of many colleagues doing it, but young kids tend to do better than astrophysicists because they regard spectra without prejudice – just as Mrs. Cannon whose ordering into “early type – late type” suggests counting lines as wrinkles. [*Spoiler: answer.*]

¹⁰ I still supply 90 viewgraph pages copying all equations of RTSA in its [equation compendium](#). The first few are empty. The passing of the viewgraph era coincided with the passing of Dutch solar physics. I quit teaching at Utrecht at my mandatory retirement in 2007. In 2011 Utrecht University [abruptly quit](#) all its astronomy [even its A&A and ApJ subscriptions]. The DOT is mothballed since. I still [teach abroad](#) when invited but without viewgraphs nor Utrecht affiliation.

¹¹ For me most figures open full-page when I click on them and also there are many blue clickers opening figures and movies elsewhere in my laptop – but not for you [invite me for the [full monty](#)].

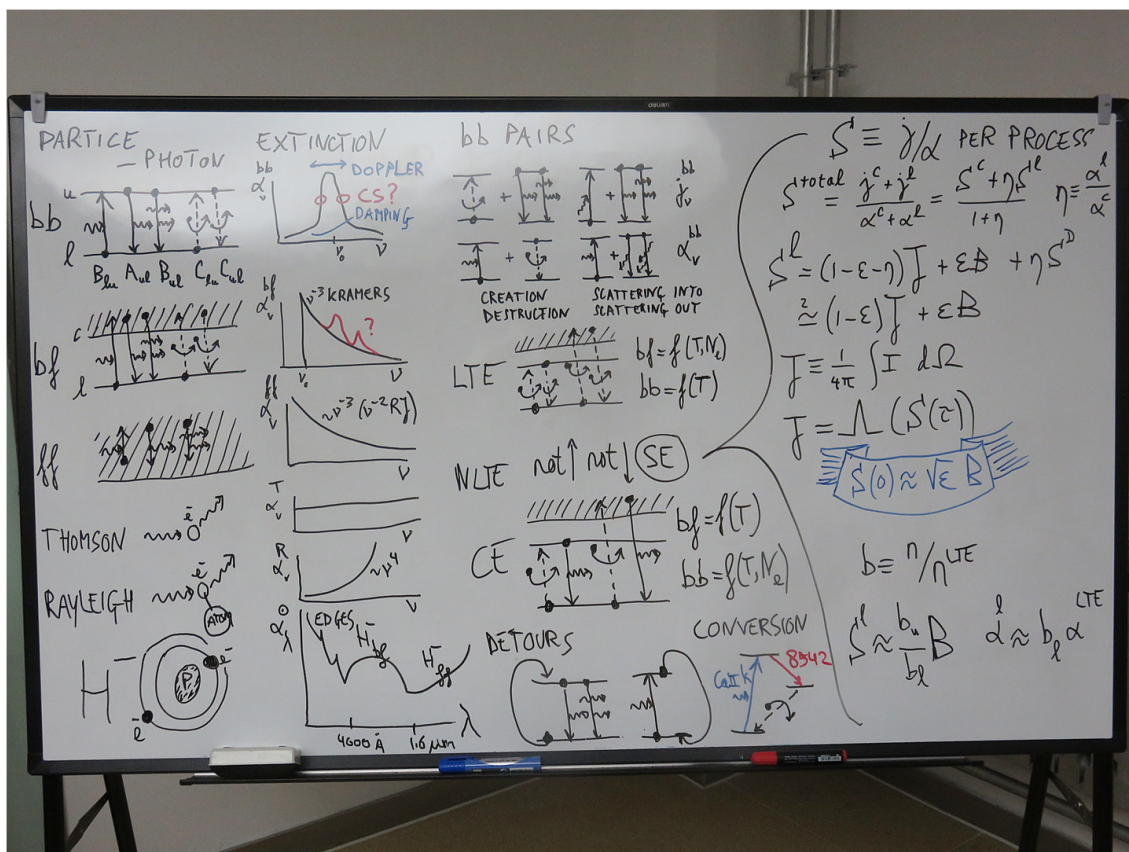


Fig. 1. Snapshot course summary, October 2018, Shandong University, Weihai. First column: particle–photon processes. Second column: corresponding extinction profiles. Third column: process pairs. Last column: key equations. Later I [signed this painting](#).

BASIC QUANTITIES

Monochromatic emissivity

$$dE_\nu \equiv j_\nu dV dt d\nu d\Omega \quad dI_\nu(s) = j_\nu(s) ds$$

units j_ν : $\text{erg cm}^{-3} \text{ s}^{-1} \text{ Hz}^{-1} \text{ ster}^{-1}$ I_ν : $\text{erg cm}^{-2} \text{ s}^{-1} \text{ Hz}^{-1} \text{ ster}^{-1}$

Monochromatic extinction coefficient

$$dI_\nu \equiv -\sigma_\nu n I_\nu ds \quad dI_\nu \equiv -\alpha_\nu I_\nu ds \quad dI_\nu \equiv -\kappa_\nu \rho I_\nu ds$$

units: cm^2 per particle (physics) cm^2 per cm^3 = per cm (RTSA) cm^2 per gram (astronomy)

Monochromatic source function

$$S_\nu \equiv j_\nu / \alpha_\nu = j_\nu / \kappa_\nu \rho \quad S_\nu^{\text{tot}} = \frac{\sum j_\nu}{\sum \alpha_\nu} \quad S_\nu^{\text{tot}} = \frac{j_\nu^c + j_\nu^l}{\alpha_\nu^c + \alpha_\nu^l} = \frac{S_\nu^c + \eta_\nu S_\nu^l}{1 + \eta_\nu} \quad \eta_\nu \equiv \alpha_\nu^l / \alpha_\nu^c$$

thick: (α_ν, S_ν) more independent than (α_ν, j_ν) stimulated emission negatively into α_ν, κ_ν

Transport equation with τ_ν as optical thickness along the beam

$$\frac{dI_\nu}{ds} = j_\nu - \alpha_\nu I_\nu \quad \frac{dI_\nu}{d\tau_\nu} = S_\nu - I_\nu \quad d\tau_\nu \equiv \alpha_\nu ds \quad \tau_\nu(D) = \int_0^D \alpha_\nu ds \quad \mu \frac{dI_\nu}{d\tau_\nu} = S_\nu - I_\nu$$

Plane-parallel transport equation with τ_ν as radial optical depth and μ as viewing angle

$$d\tau_\nu \equiv -\alpha_\nu dz \quad \tau_\nu(z_0) = -\int_\infty^{z_0} \alpha_\nu dz \quad \mu \equiv \cos \theta \quad \mu \frac{dI_\nu}{d\tau_\nu} = I_\nu - S_\nu$$

[start](#) [index](#)

Fig. 2. Screenshot of [SSF (pdf 23)]. SSF offers 119 similarly-styled theory displays with a negative evaluation [SSF (pdf 120)]. SSX offers 185 example displays. SSI offers only 16 introductory displays – you might start with these. The “start” button at the bottom should jump to the clickable contents overview, “index” to a clickable thumbnail index.

in wavelength (NLW), nonlocal in time (NLT). Solar physicists generally appreciate NLS better than NLW, NLT least.

NLS means that radiation received from the location we are studying is influenced by local radiation there that came from elsewhere. It is daily familiar to us since our daytime outdoors is NLS illuminated. Whether sunshine or overcast, all photons we see were made in the Sun and made it into our eyes by scattering, mostly multiple. As NLS as it can get! Very much out of LTE since the radiation temperature is about 6000 K, higher than our local temperature.¹⁷ NLW means that radiation received from the location we are studying is influenced by radiation at other wavelengths at that location. We do not suffer NLW because sunshine scattering around us is monochromatic (monofrequent); every detected photon still has the energy (frequency, color) with which it left the Sun. All solar Fraunhofer lines also reach our retinas unmolested (but disk-averaged and unnoticed¹⁸). We see the sky blue and the setting Sun red not because of underway color change but because Rayleigh scattering off molecules has higher probability at shorter wavelength. The green flash¹⁹ combines that with larger refraction in the blue.

NLT means that radiation received from the location we are studying is influenced by what happened there or thereabouts earlier. We suffer outdoors NLT because our sunshine is eight minutes retarded – but the same for all photons so we don't care.

Solar NLS defines outward decline of line source functions²⁰ that is well exemplified by the Na I D lines and most exemplified by Ly α , but it also brightens ultraviolet continua in and from the solar atmosphere [SSF (pdf 109)]. More below.

Solar NLW is exemplified by most atomic lines having opacity deficiencies up to an order of magnitude from sensing the scattering ultraviolet continua in ionization. It is less commonly appreciated, for example not in profile-fitting “inversion” codes nor in spectral irradiance modeling. More below.

Solar NLT is exemplified by solar H α which is a NLS $\sqrt{\epsilon}$ scattering line but it is also very NLW because Ly α defines its extinction (opacity) and a loop ionizing per scattering Balmer continuum from $n=2$ with cascade recombination back to $n=2$ including H α photon losses contributes to its source function. It is also very NLT because this loop is controlled by the n_2 population which lags badly in gas that was first heated and then cools, as happens continuously in the dynamic structures constituting the solar chromosphere and even in long-lived filaments/prominences appearing as chromosphere-like material high in the corona. Solar NLT can reach many orders of magnitude but is ignored in almost all modeling by invoking statistical equilibrium (SE). More below.

¹⁷ Only our eyesight is adapted to this radiation temperature but not simply to the Planck function for the solar effective temperature. Stating that would need specification whether our retinas measure per wavelength, frequency, wavenumber or count photons – see [SSF (pdf 50)] of which the last panel shows why high-energy astrophysicists plot λB_λ or νB_ν . Our eye bandpass was defined in our aquatic past by the penetration of sunlight in sea water, as for giant squids whose eyes have similar but better design (Feynman I Fig. 36-10) and might suit nighttime astronomers better. As early mammals ashore we became dichromats being nocturnal to hide from predating dinosaurs. After these were blasted into oblivion early hominids restored red-detecting cones (perhaps to spot low-hanging fruit) giving us color-triangle vision (Feynman I Sect. 35) to appreciate Kodachrome Basin.

¹⁸ Even when you look at your beloved although (s)he gets so richly adorned: 27500 colorful lines (not wrinkles) visible on her/his face!

¹⁹ My most beautiful was from the Neemach Mata temple in Udaipur.

²⁰ I call this $\sqrt{\epsilon}$ scattering after the blue-bannered equation in Fig. 1 which results for isothermal constant- ϵ atmospheres from the 2-level simplifications of Eq. 2 and Eq. 3 below. See note 43.

I summarize the theory in Sect. 3, followed by classic developments in order of complexity in Sects. 4–7. Finally in Sect. 8 the hardest nut to crack: the spectrum of the chromosphere.

3. RT basics

Fig. 1 and Fig. 2 show overviews. Table 1 specifies acronyms I bombard you with.²¹

Intensity. The basic RT quantity is specific intensity I_ν , describing energy in a beam of photons at a given location at a given time at a given frequency in a given direction, measured per units of area, time, frequency bandwidth and beam spreading [ISSF Sect. 3.1 (pdf 9)] [IART Sect. 2.1 (pdf 22)] [RTSA Eq. 2.1 (pdf 29)]. The last ensures that intensity does not vary with travel distance [SSF (pdf 25)], an ingenious macroscopic way to express that photons are bosons that do not decay and may travel through the whole universe without change and convey the whole universe to us for inspection.

Common sense suggests that the Sun is brighter than a distant star, but that is irradiance which is flux [SSF (pdf 24)] which is not measured per unit of beam spreading (solid angle [RTSA Fig. 2.1 (pdf 30)]). If the distant star is solar-type it shows the same intensity, also when your time-travel starship parks you just above its surface.²² If your giant groundbased telescope resolves it the stellar intensity in the focus is the same as the solar intensity in the focus of DKIST.²³

Matter–radiation interactions. Photons live forever²⁴ after their creation unless they meet fermions and interact. Also their creation is fermion business. For atoms, ions and molecules the photon-involving processes are bound-bound transitions producing spectral lines and bound-free and free-free transitions producing continua. In addition there are Thomson scattering of existing photons by free electrons and Rayleigh scattering of existing photons by bound electrons. These processes can provide local emissivity or extinction changing the intensity in

²¹ It would be good to hover your cursor over an acronym to pop up its meaning, best Wikipedia-style clickable for more. I have tried latex command pdftooltip in pdfcomment.sty for such popups but they worked too different between pdf viewers or not at all.

²² If the universe were infinite, eternal and homogeneously filled with stars our night sky would be solar bright everywhere, also in neutrinos, and the fraction of astronomers studying this text would be higher.

²³ *Solar telescopes.* These are intensity telescopes and therefore photon-starved, worse when larger (nighttime colleagues may not believe this). Reason: for pixels that resolve the diffraction limit (as they should) the flux of photons per pixel does not vary with aperture size, but smaller pixels sample smaller solar surface area (that's the game) for which the solar change time (say crossing at solar sound speed) is faster. DKIST therefore needs four times faster data-taking cadences than the SST unless used as light bucket. This leaves four times less time for multi-frame collection for the required speckle or MOMFBD restoration. The latter technique (van Noort et al. 2005) needs fewer frames which is an important boon. At the DOT we used two-channel speckle reconstruction (Keller & von der Lühe (1992)) to reduce speckle burst sizes in scanning through H α by adding wide-band imaging as is also done for SST MOMFBD. It is easier to sample brightness = irradiance from a distant star with larger aperture yielding more photons as naively expected. On the other hand, fortunately our resolvable star kindly offers wavefront-encoding granulation everywhere on her surface so that we do not need a laser star for every isoplanatic patch as ELT does.

²⁴ Heeck (2013) concludes that they live at least 3 years – in their rest frame, meaning 10^{18} years for us.

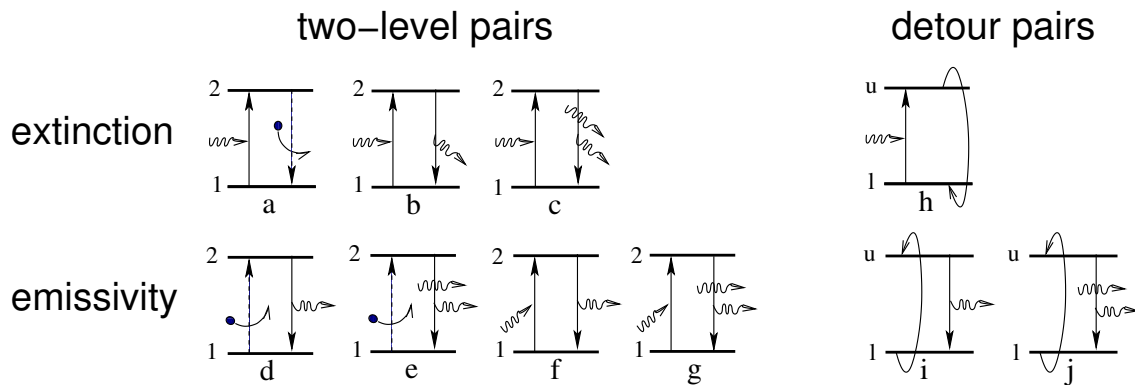


Fig. 3. Atomic transitions governing line formation arranged in photon-involving pairs. The intensity in the beam of interest travels from left to right. All photons drawn here are at the line frequency = jump energy. The pairing categorizes what may happen to an atom after excitation (at left in each pair). It won't stay excited long, for a 2-level atom only between $1/A_{ul} \approx 10^{-8}$ s (resonance) and $1/A_{ul} \approx 10^{-2}$ s (forbidden) until **b**, **d** or **f** occurs spontaneously, yet shorter if the atom while excited meets a deexciting collider **a** or an inviting akin photon to join on its way (**c**, **e**, **g**). Multi-level detour paths (righthand cartoons) combine other-wavelength transitions involving other levels and may include analogous bound-free transitions. There may be radiative or collisional deexcitation to another lower level or radiative or collisional excitation to a higher level including ionization and recombination. Other transitions eventually return the atom to the start-off level *l*. There may be endless up-down scattering in between so the possibilities are infinite. The upper row shows pair combinations contributing to line extinction: collisional photon destruction (**a**), scattering out of the beam (**b** and **c**), photon conversion out of the beam (**h**, into other-wavelength photons and/or kinetic energy). The lower row shows pairs contributing to line emissivity: collisional photon creation (**d** and **e**), scattering into the beam (**f** and **g**), detour photon production into the beam (**i** and **j**). Pairs **c** and **g** have equal probability by requiring one photon in the beam and one with arbitrary direction.

a given beam, in particular the intensity along the “line-of-sight” towards our telescope. Other photon-producing or photon-affecting processes may be ignored for the solar atmosphere unless you are a radio astronomer (cyclotron, synchrotron, plasma radiation) or high-energy astronomer (pair annihilation).

Photons being bosons means that they like to sit in the same place and therefore that any interaction producing or scattering a photon has a stimulated addition in which the new or scattered photon coherently accompanies similar passing radiation that enhances the interaction probability.

Bound-bound, bound-free, free-free interactions. The five bound-bound interactions are photo-excitation, spontaneous photo-deexcitation, induced photo-deexcitation, collisional excitation and collisional deexcitation [SSF (pdf 70)], [ISSF Sect. 5.1 (pdf 23)], [IART Chapt. 5 (pdf 60)], [RTSA Sect. 2.3.1 (pdf 39)]. The same five hold for bound-free ionization and recombination with appropriate nomenclature, and the same five hold for free-free interactions (but collisional three-body up or down transitions have no radiative interest).²⁵

Pair combinations. Combining the above interactions in successive pairs is so important that I do not refer to or link to but copy Fig. 1 of Rutten (2019) here in Fig. 3. It came from [SSF (pdf 105)] and is an extension of [RTSA Fig. 3.3 (pdf 85)] with multi-level detours. Ca II and H α detour examples are shown

in Fig. 2 (pdf 4) of Rutten (2019). With these added this is a complete inventory of how line photons can be locally created and locally modified by fermion interactions. Below I refer to these pairs by their alphabetic labels. Similar pair diagrams can be drawn for bound-free transitions (some in Fig. 1).²⁶

Equilibria. [SSF (pdf 69)] summarizes bound-bound equilibria with the 2-level simplification at left in Fig. 3. It assumes that any excitation is followed by de-excitation in the same transition, ignoring multi-level NLW and so restricting RT to a single wavelength (CS) or the narrow band covering a single transition (CRD).

TE = “*thermodynamic equilibrium*” describes a homogeneous isothermal fully-enclosed gas where nothing ever happens and where every type of excitation occurs just as frequently as its de-exciting counterpart (“detailed balance”): as many collisions down as up, as many radiative transitions down as up, with all rates defined by the temperature. Maybe this boring paradise occurs approximately at the center of a black hole, but not within the Sun since non-enclosed implies net outward energy leak from the hot core to the cold universe and the accompanying outward temperature decline through the entire Sun until the energy surplus escapes.²⁷

SE = “*statistical equilibrium*” foregoes detailed balancing but requires overall balancing, meaning that all level populations do not vary with time however they are made. For each level the

²⁵ *Extinction diagrams.* Diagrams of bound-free and free-free He and He extinction for different stellar atmospheres assuming SB are shown in the four Figs. 8.5 of Gray (2005) [Fig. 8.5a has (in Gray’s words) a small error of 10^{-26}]. Three earlier versions of Gray (1992) are copied into [RTSA Fig. 8.14 (pdf 211)]. The classic “confusograms” in Figs. I–XV (pdf 17) of Vitense (1951) were redrawn in English in Novotny (1973), with the solar one reprinted in [RTSA Fig. 8.5 (pdf 199)] and four stellar ones in [RTSA Figs. 8.15–8.18 (pdf 212)]. Their not-so-trivial interpretation is treated in [RTSA Problem 10 (pdf 252)]. I have emulation programs and comparable resulting diagrams for both references in my IDL *edulib*. An overview of total extinction including lines in the FALC atmosphere is shown in Fig. 6 (pdf 13) of Rutten (2019).

²⁶ In oral teaching I draw these cartoons on the whiteboard as in Fig. 1 and point to them all the time. [In the blackboard era I threw pieces of chalk at inattentive students until hitting Minnaert.]

²⁷ *Solar neutrinos.* Fortunately the fusion-released energy escapes by slow diffusion [RTSA Shu quote (pdf 110)]. In contrast, the neutrinos that are also released in hydrogen fusion are virtually unstoppable and escape directly from the solar core [for them we do not need RT theory]. They posed a **big problem** last century when too few were detected. It was not a fault of the measurement nor of stellar structure theory but the blame was on particle physics: part of the solar neutrinos “oscillate” into another flavor on their way here. Photons, once they escape, fulfill their task of information carrying better.

rate equation [RTSA Eq. 2.100 (pdf 52)] governing changes to a level population is zero. There may be excesses between going up or down some particular way that are compensated by others going down or up. Simplest example: CE = only pair **d**, all ups collisional, all downs spontaneous radiative for lack of impinging particles and photons. The SE assumption underlies all following equilibria except non-E.

LTE = “*local thermodynamic equilibrium*” assumes TE at the local temperature while permitting temperature and density gradients and small leaks, clearly a cheap cheat. Its definition is that Saha-Boltzmann (SB) partitioning applies to all populations, as for element Schadeenium²⁸ in my recommended SSA 2 Cecilia Payne exercise (pdf 9). It is often thought that LTE is defined as equality of the source function S_ν to the Planck function B_ν , but this is a corollary [RTSA Sect. 2.3.2 (pdf 43)] [RTSA Eq. 2.7.3 (pdf 45)]. LTE holds closely within the Sun and to some extent for many lines and continua in the low photosphere. The condition is that collisions both up and down heavily outweigh photons up and down in Fig. 3 and its bound-free counterparts: photon destruction **a** and photon creation **d** + **e** must dominate over spontaneous and stimulated scattering, also for all steps in the photon conversion sequences at right. Thus, the photons must behave as “honorary gas particles” (Castor), likewise boxed in to local circumstances; what we observe must be only a small leak. In SB partitioning the level population ratios sense only the temperature [RTSA Eq. 2.86 (pdf 49)] because the dominating up and down collisions both require one collider so that the density drops out. The ionization stage ratios sense temperature more complicatedly by folding the Boltzmann factor with the Maxwell distribution for the caught electron into the Saha distribution [RTSA Eq. 2.88 (pdf 50)] and scale inversely with the electron density from the need to catch one.

NLTE = “*non-local thermodynamic equilibrium*” is a misnomer. Usually it means assuming SE with accounting for NLS, less often NLW, much less often NLT.

CE = “*coronal equilibrium*” assumes SE but low electron density and absence of local irradiation so that only **d** and its bound-free counterpart remain. Every photon is locally created by a collision obeying the local kinetic temperature. They occur infrequently but in their ground state ions can wait endlessly for suited colliders. After eventual excitation no collider or stimulating photon arrives within the $1/A_{ul}$ decay probability for spontaneous deexcitation. The resulting photon escapes outward to space and may enter our telescope or drowns inward in the Sun or gets bound-free scattered in other gas (more below). In this case the level ratios sense both temperature and collider density since there is only the required bound-bound up collision, not the down collision additionally required for LTE. The stage ratios sense only temperature because each ionization is collisional and each recombination is radiative requiring a single electron catch. CE and SB are thin versus thick partitioning extremes. [SSX (pdf 174)] compares them for photospheric electron density; the SB peaks shift left by about -0.05 in $\log(T)$ per tenfold N_e reduction.

A complication and a boon is that dielectronic excitation must be included beyond the single-electron jump pairings in Fig. 3. The reason is that at coronal temperatures the mean Maxwellian energy is far above the desired standstill value for the free electron to be caught at ionization threshold in one-

electron recombination (peak probability in hydrogenic Kramers $\alpha_v^{bf} \propto \nu^{-3}$ edge decay). The shift of the Maxwell peak to larger energy for higher temperature gives $1/T$ dependence to radiative recombination rates. With dielectronic excitation this too large thermal energy is cut down by using a large part for simultaneous bound-bound excitation of another electron in both dielectronic ionization up and dielectronic recombination down. They are multi-level additions behaving in CE as pair **d**: up only collisions, down only spontaneous photons.²⁹ temperature-only sensitivity of CE stage partitioning is therefore maintained; the rate ratio between direct and dielectronic depends only on temperature (Maxwell peak shift). The complication is that many possible bound-bound transitions to very high levels must be included and evaluated (in CHIANTI³⁰). The boon is that the dielectronic variants produce photons in many lines including the diagnostics in the AIA EUV passbands and help keeping

²⁹ *Dielectronic ionization and recombination.* Unstable levels: both processes excite one electron in a normal bound-bound transition and put a second electron into a level above the nominal ionization limit of the lower-stage ground state. This is possible because the orbitals are boosted by the first excitation; they may also be non-hydrogenic affected. Such a state is unstable because *autoionization* may occur, freeing the electron from there into escape. This usually leaves the fresh ion in its ground state and then the freed electron carries off the energy excess of the unstable state above that, but if the fresh ion is excited it decays, always per line photon in CE. The other path out of the unstable level is decay of one (or both) of the excited electrons, in CE also always per line photon, into a configuration with the second electron in a regular bound level below the nominal ionization limit (*radiative stabilization*). Autoionization often has higher probability than this spontaneous stabilization.

Dielectronic ionization: an energetic collider, usually hitting the lower ion in its ground state, kicks up both electrons with the first one taking a good part of its kinetic energy. With the remainder the second may ionize bound-free but is more likely put into a high level. If this is still below the ground-state limit both electrons decay radiatively, the second likely in a cascade, together a two-electron multi-level version of pair **d** converting kinetic energy into line radiation without ionization. However, if the second electron reaches an unstable level above the nominal limit then it may be freed by autoionization before its radiative decay, a sequence called “excitation-autoionization” by Dere (2007). The other still bound excited electron decays to the ground state of the new ion, also producing one or more line photons. In this double-excitation manner the energetic collider yields higher ionization probability than for one-electron collisional ionization by losing energy that eventually escapes as line photons.

Dielectronic recombination: in the reverse sequence the energetic colliding free electron kicks up the first bound electron to a high level and is itself captured into an unstable state which stabilizes already before re-auto-ionization through spontaneous radiative decay of one of the two excited electrons, often the lower one, to a stable level of the lower stage. If that is still excited it decays radiatively to the ground state; the other electron also, usually per multi-level cascade. Depending on the branching ratios some decays may temporarily end up in a metastable level comparable to Ca II 8542 Å in the Ca II detour example in Fig. 2 (pdf 4) of Rutten (2019) but then not go down from there collisionally as there but CE-wise radiatively in a forbidden transition such as the optical coronal emission lines.

Radiative result: no continuum but line photons galore.

³⁰ *CHIANTI.* [Suggestion: *Coronal Holism In Appreciating Non-Thick Ionization.*] Community effort by these colleagues. It handles coronal spectroscopy with a large transition inventory for evaluating CE ionization equilibria, radiative losses, DEMs and more. The need to include numerous lines contributed by dielectronic processes (note 29) makes it ever-growing. Example (from P.R. Young) for O VII (He-like): currently CHIANTI specifies 577 levels, 127 below the ionization threshold and autoionization rates specified from 128 up. Since CHIANTI v9 the 25 levels of O VIII are added also.

²⁸ Which you can’t pronounce. My Utrecht colleague Aert Schadee invented this didactic element. Utrecht Nobel-winner Tini Veltman called his revolutionary algebra solver “schoonschip” (shipshape) to make certain that no CERN colleague could pronounce it.

the corona cool through substantial radiative losses.³¹ Original Fig. 1 (pdf 4) of Burgess (1964) shows the high-temperature importance for He I ionization. The radiative rate drops as $1/T$ but the dielectronic rate first peaks two-orders-of-magnitude higher before its $1/T$ decay sets in. Classical Fig. 3 (pdf 20) of Jordan (1969)³² shows its importance for coronal iron partitioning (the lower panel shows partitioning without it from House 1964). The “Jordan versus Payne” CE–SB comparisons on [SSX (pdf 174)] include it also. A nice summary following Burgess (1964) is given in Sect. 6.2.5 (pdf 144) of Jefferies (1968).³³

³¹ *Radiative losses versus heating.* Summing all emergent photons from an EUV-bright feature quantifies radiative losses that measure required heating for a stable structure obeying CE including SE. It is a mistake to count summed brightness of short-lived features (e.g., “nanoflares”) as contribution to coronal heating: to the contrary, this energy is radiated away, only the remainder of the feature heating may count.

³² Carole Jordan is the CE counterpart of SB Cecilia Payne, moving to Oxford from Culham rather than to Cambridge USA from Cambridge UK. My SSA exercises should become Annie Cannon – Cecilia Payne – Carole Jordan, likely using CHANTI, and also add a Walter Grottrian [SSX (pdf 6)] exercise.

³³ *Ca II H & K core reversals.* On page 128 (pdf 146) Jefferies cited the suggestion of Goldberg (1964) that the double emission peaks of the Ca II H & K core reversals may be due to dielectronic recombination and also the demonstration by Noyes (1965) that this does not work for CRD in H & K. Noyes used Avrett’s brandnew CRD scattering code producing the canonical $\sqrt{\epsilon}$ graphs of [SSF (pdf 80)] in the belief that CRD is a better approximation than CS which he had initially assumed in Goldberg & Noyes (1964), but actually H & K are PRD lines. Goldberg’s mechanism seems to be collisional dielectronic ionization of Ca I leaving Ca II ions excited in the upper levels of H & K – but I note that Ca I is very much minority species and think it was a red herring. It does illustrate how during decades the Ca II H & K reversals were the most discussed and most enigmatic features in the optical spectrum by being the only Fraunhofer-line departures from regular bell shape. This extended literature was outstandingly reviewed by Linsky & Avrett (1970) (but not mentioning the Goldberg–Noyes dielectronic angle). Athay & Skumanich (1967) had suggested that the H₂ and K₂ dips map a temperature minimum as in NLTE cartoon [SSF (pdf 37)], but then Shine et al. (1975) showed that PRD upsets this notion as in cartoon [SSF (pdf 89)] with their Fig. 9 (pdf 7) copied in [SSF (pdf 92)]. However, such plane-parallel modeling could not explain that the violet-side peaks in H & K are higher than the red-side peaks (the red Ca II H_{2K} peak is barely visible in the atlas profile in Fig. 11 (pdf 10) of Rutten et al. 2011). In addition, high-quality narrow-bandpass imaging as in the “Selected spectroheliograms” of Title (1966) (which I have on my desk but cannot find in ADS) and the remarkable K_{2V} spectroheliogram taken by B. Gillespie at Kitt Peak that adorned the cover of Lites (1985) and was partly shown in Fig. 2 (pdf 4) of Rutten (2007) and elsewhere showed that the asymmetries come from small bright grains that occur intermittently in internetwork cell interiors and are not magnetic (although some authors persistently claimed this). This very wide and most confusing literature was extensively reviewed by Rutten & Uitenbroek (1991) where we concluded that K_{2V} and H_{2V} “cell grains” are an acoustic interference phenomenon along the lines of the ad-hoc scheme of Liu & Skumanich (1974) – which was then brilliantly proven with observation-driven RADYN simulation by Carlsson & Stein (1997) who in their Fig. 18 (pdf 13) reproduced observed spectral grain development as in Fig. 2 (pdf 4) of Lites et al. (1993). Its intricate pattern had been established in Fig. 4 (pdf 9) of Cram & Damé (1983) and was sketched in Fig. 2 (pdf 7) of Rutten & Uitenbroek (1991). More in note 71. However, the Ca II H & K core reversals also govern the famous cool-star relation in Fig. 1 (pdf 9) of Wilson & Vainu Bappu (1957) which to my knowledge remains unexplained. Doing so will make you famous! Since the main contribution to the peaks in solar irradiance is from the calcium network on classic spectroheliograms I suggest an approach along the lines of Ayres (1979) applied to magnetostatic fluxtube atmospheres

Non-E = “non equilibrium” means non-SE = NLT, admitting temporal variations in populations, i.e., having the SE population equations [RTSA Eq. 2.100 (pdf 52)] not equaling zero but a function of time. For hydrogen it is often called “non-equilibrium ionization” but the actual agent is NLT slow collisional settling of Ly α in cooling gas whereas H ionization occurs in an SE Balmer loop (more below).

Bound-bound redistribution. Eddington asked on page 2 (pdf 2) of Eddington (1929) the “crucial question” to what extent a resonance-scattered photon remembers the frequency it had in the preceding photo-excitation (pairs **b, c, f, g**). The one extreme is that it does precisely in “coherent” scattering (CS). In Eddington’s days this was thought to be the rule, but in his landmark thesis Houtgast (1942) showed that most solar lines in the visible obey the other extreme, suffering complete redistribution (CRD) meaning complete loss of memory and representing a new sample of the line extinction profile rather than δ -function frequency conservation. CRD is indeed valid for most lines except the strongest (large extinction) because their photons escape high in the atmosphere where collisions governing collisional redistribution (“damping”) are rare. These must be described by partial redistribution (PRD) which combines Doppler redistribution in the core (CS in the frame of the atom but an redistributing average over the observed individually-Doppler-shifted photon ensemble) with coherency in the inner wings and collisional redistribution in deeply-formed hence collision-rich outer wings [SSF (pdf 89)]. The best-known examples are Ly α , Mg II h & k, Ca II H & K [SSF (pdf 92–93)]. My personal example is Ba II 4554 Å.³⁴ I must concede that this issue remains “not yet” in

with attention to the slow network Dopplershift waves in the third panel of Fig. 3 (pdf 4) of Lites et al. (1993) and interpretation as Kato et al. (2011).

³⁴ *Ba II 4554 Å and Mn I lines.* Ba II 4554 Å showed PRD signature near the limb in my eclipse observation in Fig. 9 (pdf 17) of Rutten (1978). It was confirmed in Figs. 1–3 (pdf 4) of Rutten & Milkey (1979) and Fig. 6 (pdf 5) and Fig. 11 (pdf 7) of Uitenbroek & Bruls (1992). The line is a valuable spectropolarimetry diagnostic (Belluzzi et al. 2007) and also a good Doppler diagnostic of the upper photosphere (Shchukina et al. 2009, Kostik et al. 2009) because it combines large atomic mass, hence small thermal broadening, with considerable core broadening by isotope splitting and hyperfine structure making it suited for filter instruments and so yielding the astounding Dopplergram in Fig. 5 (pdf 4) of Sütterlin et al. (2001). Other lines with large hyperfine broadening are the Mn I ones recommended by G. Elste to W.C. Livingston as candidates for long-term spectral irradiance monitoring because they are insensitive to infamous microturbulence (note 54). Livingston found larger cycle-dependent variation in Mn I 5394.7 Å than for other atomic lines (Fig. 16 (pdf 9) of Livingston et al. 2007). This enhanced sensitivity was attributed by Doyle et al. (2001) to pumping of Mn I 5394.7 Å by Mg II k but erroneously assuming CRD for Mg II k in the spectral synthesis of their demonstration. Vitas et al. (2009) showed that the actual reason is that hyperfine-broadened lines indeed lack the “microturbulent” thermal and granular Doppler smearing through which all narrower photospheric lines lose such sensitivity [MURaM demonstration in their Fig. 6 (pdf 8) and Fig. 7 (pdf 9)]. I reviewed this issue in Rutten (2011, not on ADS but posted here) where Fig. 1 (pdf 2) summarizes Livingston’s results and Fig. 2 (pdf 3) shows that in plage the Mn I blend (at -0.7 Å from Mg II k center) is not pumped at all because the blend is at the wavelength where the PRD source function departs most from the CRD one and sits in the dip outside the Mg II peak even in strong plage. The apparent Mn I over Fe I brightening of plage in Fig. 1 (pdf 2) in scans from Malanushenko et al. (2004) results from mean-field brightness normalization. The surrounding granulation is actually darker in the Mn I line than in the turbulence-sensitive Fe I line while

[RTSA Sect. 3.4.3 (pdf 92)]. The clearest explanation so far is in Chapter 5 (pdf 110) of Jefferies (1968) summarized in [SSF (pdf 91)]. The introduction to Sukhorukov & Leenaarts (2017) is a good literature overview. Recent developments are listed in [SSX (pdf 164)]. Next to frequency redistribution there is also angle redistribution to worry about for moving gas due to its Doppler anisotropy – what gas in the solar atmosphere doesn't move? See Leenaarts et al. (2012b).

Bound-free redistribution. Bound-free transitions are similar to bound-bound transitions and may be described by the same rate equations [RTSA Sect. 3.2.3 (pdf 68)]. Resonance scattering (radiative up and down in the same transition, pairs **b**, **c**, **f**, **g**) is also the same except that the bound-free spectral extent is much wider and that recombination catches an electron as a fresh sample of the kinetic energy distribution without remembering the energy of the electron kicked out in preceding ionization, only memory of ionization to the threshold but not of the excess above it. Hence there is always CRD over the ionization edge.

A particular case is bound-free scattering of EUV line photons imaged in narrow bands as by EIT, TRACE, AIA. They may be extincted in bound-free photo-ionization of H I, He I or He II, most likely followed by spontaneous photo-recombination because the colliding-particle and suited-photon densities are too low for other bound-free equivalents than scattering pair **b**. Through CRD such a bound-free scattered photon not only gets a random redirection but also a new wavelength, most likely near the ionization threshold (probability for H I given by Kramers ν^{-3} decay [RTSA Eq. 2.74 (pdf 45)]), hence far from the line. Bound-free scattering so redirects radiation out of the line of sight and also out of the passband; it may locally darken the narrow-band image (often misnamed “absorption”).³⁵

Free-free redistribution. Every collider is a fresh sample of the kinetic energy distribution giving redistribution over the probability ν^{-3} decay [RTSA Eq. 2.76 (pdf 46)], a continuum without threshold. In addition there is no memory of a preceding transition so that pair combinations as in Fig. 3 make no sense. If the kinetic energy distribution is the Maxwell distribution defined by temperature then that fully defines both emissivity (Brehmstrahlung) and extinction so that their ratio (source function) is the Planck function. Thus, free-free transitions always have $S_\nu = B_\nu$ because they are intrinsically collisional.

A particular case is ALMA for which at longer wavelengths the main agent is hydrogen free-free (electrons meeting protons) [SSX (pdf 32)]. ALMA is therefore often appreciated as a ther-

these lines show the same actual plage brightness because the fluxtube “holes” schematized in Fig. 4 (pdf 5) reach as deep because both Fe I and Mn I ionize away.

³⁵ *Dark EUV features.* When you see the same black features on bright backgrounds (on the disk but outside no-emissivity coronal holes) in multiple EUV wavelengths then out-of-the-passband scattering is the most probable mechanism. Cartoon in [SSX (pdf 10)] [where “volume blocking” is a bad misnomer]; I drew it as Fig. 10 (pdf 12) of Rutten (1999) to answer a TRACE question by C.J. Schrijver. It shows that when black features are also present in He I 584 Å images (not in AIA alas) the agent is photoionization in the H I Lyman continuum. This may occur in filaments seen in EUV lines as in the IBIS active-region blinker of note 99. Other such features are “condensation” (meaning recombination) clouds, e.g., in coronal rain (Antolin & Rouppe van der Voort 2012, Antolin et al. 2015) visible in H α via non-E recombination cascade giving large opacity on the disk and large emissivity off-limb as in the temporal cycling of Froment et al. (2020) (Fig. 7 (pdf 10)).

mometer, but it is as often not appreciated that the extinction is likely NLT controlled and may be orders of magnitude above the local LTE value, just as for H α . ALMA is a thermometer but without easy knowledge where you stick it (more below).

Thomson and Rayleigh scattering. In terms of Fig. 3 these scatterings are described by pairs **b**, **c** and **f**, **g**, none of the others. In the Thomson limit (short of Compton) they still suffer Doppler redistribution. Pairs **c** and **g** cancel in occurrence probability, averaged for Doppler redistribution.

A particular case is Thomson scattering by free electrons making the white-light corona so beautifully visible [SSX (pdf 5)] during eclipses and with LASCO. Since this is monochromatic scattering the absence of photospheric Fraunhofer lines, unlike the spectrum scattered by your nose, was puzzling until Grotrian (1931) noticed that Ca II H & K are shallowly present and proposed here (pdf 22) that their 100 Å smearing corresponds to 7500 km s⁻¹ Doppler redistribution – but his attribution to thermal motion at million K temperature came later (I suspect he didn't dare yet at the time). For smooth-disk illumination the scattered brightness is locally proportional to N_e , but as pointed out by Minnaert (1930) limb darkening (and perhaps spots) must be accounted for in the local scattering source function $S_\nu = J_\nu$, and also the integration along the entire line of sight with problematic confusion between different structures (evident in the marvelous Druckmüller images).

Extinction and emissivity. The extinction coefficient³⁶ and the emissivity³⁷ are the macroscopic ways of quantifying the above processes locally along a given beam with given intensity (Fig. 2 = [SSF (pdf 23)], more explanation in [ISSF Sect. 3.2 (pdf 9)], [IART Chapter 3 (pdf 34)], [RTSA Sect. 2.1.2 (pdf 32)]). Extinction is measured as cross-section so it simply adds up for different processes acting at one wavelength: (multiple overlapping) lines and continua. A photospheric overview is in [SSF (pdf 68)]. The ultraviolet bound-free edges of Si I, Mg I, Fe I and Al I contribute the electrons needed for H⁻ with their joint abundance giving $N_e \approx 10^{-4} N_H$ making the gas near-neutral.³⁸

A particular point is that photons contributed by stimulated emission are not counted positively as contribution to emissivity but negatively as contribution to extinction. I suspect that this was first done by Einstein himself. It facilitates the description because extinction (**a** + **b** + **c** + **h**) and stimulated emission (**e** + **g** + **j**) both need beam photons and therefore similar quantification (Einstein B values [SSF (pdf 70)]). Moreover, with this subtraction the cancelation of pairs **c** and **g** is effectuated. If this isn't done the actual extinction would be overestimated and op-

³⁶ Naming: in many texts this is called “absorption coefficient”. I follow C. Zwaan in using “extinction” because the photon is taken out of the particular beam (direction and frequency) but may still exist in another direction (scattering pairs **b** and **c**) or at another frequency (conversion pair **h**). Absorption is then reserved for pair **a** only, which has sometimes been called “true absorption”.

³⁷ Naming: Zwaan, Jefferies, Mihalas and others called this “emission coefficient”. I followed them in IART and also while writing RTSA in 1995, but at an Oslo school that summer P.G. Judge used “emissivity” and I realized that that is a better name because it is not a coefficient, not a fraction of something but measures new radiation.

³⁸ Gaseous matter is mostly plasma throughout the universe but in cool-star photospheres almost all electrons and in planetary atmospheres all electrons are tied to nuclei. We live in an extraordinary neutral environment energized by an extraordinary near-neutral environment.

tical depth scales would suggest larger opaqueness and higher escape than actually the case.³⁹

Emission measure. Colleagues studying the coronal EUV spectrum usually do not worry about photons after their creation when not ending in their telescope.⁴⁰ Optically thin travel to the telescope, no extinction, only emissivity counts in their production per pair **d**. This must be evaluated for all lines within the passband⁴¹ at every location along the line of sight and integrated with confusion an issue. Locally the emissivity scales with the product $n_l N_e$ of lower-level population density and electron density, the latter representing the required collider for excitation per **d** which is most likely an electron. Regard a resonance line from an ion ground state. Its population enters as $(n_l/N_E) A_E N_H$ with element E abundance $A_E = N_E/N_H$, hence local emissivity $\propto g f A_E G_{ij}(T) N_e N_H$ where G_{ij} is a conglomerate function of temperature describing the element partitioning defining n_l/N_E for this line ij and needing all sophistication of **CHIANTI** for evaluation within the CE assumption. For a review see [Del Zanna & Mason \(2018\)](#). If the line is from an excited state function G_{ij} depends also on electron density. Integration over the volume of an unresolved emitting structure (say a loop) yields emission $\propto g f A_E \int G_{ij}(T) N_e N_H dV$ where N_H is often replaced by N_e taking $N_H = N_p \approx N_e (1 - 2B)$ with B the helium/hydrogen abundance ratio ([Sect. 5 \(pdf 20\) of Pottasch 1964](#)). The density dependencies $N_e N_H$ may be removed using the differential emission measure $DEM(T) \equiv N_e N_H (ds/dT)$ in $\text{cm}^{-5} \text{K}^{-1}$, a combined local gradient measure that defines the emission measure integrated over s along the line of sight as $EM \equiv \int N_e N_H ds = \int DEM(T) dT$ in cm^{-5} ([Sect. 7 \(pdf 113\) of Del Zanna & Mason 2018](#)). With this density removal the emission in the line from a feature becomes $\propto f A_E \int DEM(T) g G_{ij}(T) dT$ where the Gaunt factor g is under the integral because it depends on temperature ([Eq. 2 \(pdf 3\) of Withbroe 1978](#)).

Source function. I wonder who gave this key non-thin quantity its well-suited name in describing weighted local addition of new photons to a given beam by dividing emissivity and extinction ([Fig. 2](#)). It seems like dividing cows and horses since their dimensions are $[\text{erg cm}^{-3} \text{s}^{-1} \text{Hz}^{-1} \text{sr}^{-1}]$ versus just $[\text{cm}^{-1}]$, but the resulting dimension is that of intensity [[SSF \(pdf 23\)](#)] which 'tis all about.

The source function is a key quantity for optically thick colleagues (those studying the photosphere and chromosphere) because it separates local physics and surround physics, or atomic perspective and environmental quality. Take a strong spectral

line, meaning large line extinction coefficient. Its addition of many bound-bound transitions to continuous transitions at its wavelength adds a high narrow spike in extinction versus wavelength. This is local physics: the required particles must be present in sufficient number set by elemental abundance, partitioning over ionization stages and atomic levels within stages that is primarily set by temperature and density (closer to SB than to CE), and transition probability. In the emissivity there is a similar spike given by lookalike particles in the upper level. In the ratio, however, this spike may vanish completely – as for LTE with the featureless Planck function as ratio. Then the ratio is completely set by the temperature, an environmental rather than an atomic physics quantity. When LTE is not valid the local environment also senses nonlocalness, surely in space (NLS), likely also in wavelength (NLW), possibly also in time (NLT). Thus, optically thick colleagues evaluate local atomic properties to define the extinction which defines where their signal comes from, then evaluate the source function to see what environmental effects may make it depart from the local temperature. This split is often described as “accounting for NLTE”.

However, such split interpretation gets mixed when environmental effects also affect the extinction. This happens when that is controlled by other transitions sensitive to source function nonlocalness. The extinction of visible atomic lines defined by scattering bound-free ultraviolet continua is one example, the dominance of Ly α in controlling H α extinction and ALMA H I free-free extinction is another. In such cases, opacity NLTE gets more important than source function NLTE. Colleagues that see NLTE only as a source function issue may miss the crux of their problem.

Also, the source function is a composite because it is a process property. Multiple processes operating at a given wavelength each have their own source function and combine weighted ([Fig. 2](#)) [[SSF \(pdf 23\)](#)]. In the solar photosphere optical lines often combine a scattering line source function with a near-LTE continuous source function because the latter is dominated by H $^-$ bound-free interactions. These are not necessarily LTE as is the case for free-free interactions. Ultraviolet bound-free continua do get far from LTE but in the optical and infrared ambient thermal kinetic energy is similar to or exceeds transition energy and at sufficiently deep formation⁴² collisions reign, making LTE a good approximation. The Na I D lines reach deepest in the optical spectrum ([Fig. 10 \(pdf 18\) of Rutten 2019](#)) because they are exemplary \sqrt{e} scatterers [[SSX \(pdf 85\)](#)]. In hotter stars where hydrogen is ionized the reverse occurs: weak LTE lines appear in emission on the dark Thomson-scattering continuum ([Fig. 1 \(pdf 215\) of Rybicki & Hummer 1992](#)). The solar Ca II H & K wings also contain weak emission lines but these are from NLTE interlocked scattering ([note 60](#)) with Fe II 3969.4 Å close to H ϵ the weirdest: it responds deeper than its quasi-continuum near-LTE background ([Fig. 8 \(pdf 9\) of Cram et al. 1980](#)).

Line source function. Most classic treatments of NLTE scattering in the line source function assume a gas of 2-level atoms to keep the description monochromatic (CS) or limited to a single line (CRD). I did the same in RTSA, with a long derivation inventing “sharp-line atoms” enabling monofrequent use of the Einstein coefficients in [[RTSA Sect. 3.4 \(pdf 84\)](#)], an elegant derivation by Zwaan of the \sqrt{e} law in [[RTSA Sect. 4.3.1](#)

³⁹ More in a [Dick Thomas memorial](#).

⁴⁰ Solar physicists used to be either thin or thick. Thin ones excelled in atomic and later in plasma physics, thick ones in 2-level scattering and later in MHD. They now grow together [but heed my scorn at the end of [note 56](#)]. The Sun doesn't care and magnanimously sends photons to both types adhering to her kind “[Principle of Solar Communicativity](#)” ([pdf 9](#)) formulated at the only solar IAU symposium ever in the USSR ([Rutten 1990](#)).

⁴¹ For spectral-passband imagers as AIA usually a complex multi-temperature combination from registering multiple lines. Spectrometers as Hinode's EIS register spectrally dispersed bands but do not inform precisely where from – slitjaw imaging as by IRIS is highly desirable – or miss the more interesting happening just off the slit. It is a pity that Fabry-Pérot imaging spectroscopy is not feasible at short wavelengths; SST/CHROMIS is the shortest ([Scharmer et al. 2019](#)). My paradise dream is slitless 2D imaging spectrometry resolving wavelength across Ly α (continued in [note 102](#)).

⁴² In the optical and near infrared solar continuous extinction is smallest so that we see deepest there [[SSI \(pdf 5 ff\)](#)] [[RTSA Fig. 8.6 \(pdf 199\)](#)], ([Fig. 6 \(pdf 13\) of Rutten \(2019\)](#)). A true solar physicist ([pdf 9](#)) observing the Earth also sees deepest in the optical.

(pdf 112)], and the classic numerical CRD results for this law in an isothermal atmosphere of Avrett (1965) in [RTSA Fig. 4.12 (pdf 128)].⁴³ Isothermal and 2-level seems farfetched but the $\sqrt{\varepsilon}$ law is often applicable and yet more often instructive.⁴⁴ An equation summary is shown in [SSF (pdf 79)] and as [RTSA concluding RT rap (pdf 275)].

Two-level scattering source function evaluation became a key part of numerical spectrum synthesis with many programs following the key concepts of opposite-direction averaging of Feautrier (1964) [RTSA Sect. 5.2 (pdf 137)] and of operator splitting of Cannon (1973), leading to approximate lambda iteration (ALI) and similar methods [RTSA Sect. 5.3.2 (pdf 145)]. Some of these programs are detailed below in Sects. 4–6.⁴⁵

The extension with multi-level detours is still lacking in my courses, so I add that here. The best descriptions so far are in Sect. 8.1 (pdf 199) of Jefferies (1968) (remove the minus in the equation below Eq. 8.8) and in Sect. II (pdf 1) of Canfield (1971a), both using ratios rather than fractions as probability parameters. Split the line extinction coefficient into the destruction (a for absorption), scattering (s), and detour (d) contributions of Fig. 3:

$$\alpha_v^l \equiv \alpha_v^a + \alpha_v^s + \alpha_v^d \quad \varepsilon_v \equiv \alpha_v^a / \alpha_v^l \quad \eta_v \equiv \alpha_v^d / \alpha_v^l \quad (1)$$

where ε is the collisional destruction probability of an extincted photon and η is its detour conversion probability. With these, the general line source function becomes

$$S_v^l = (1 - \varepsilon_v - \eta_v) J_v + \varepsilon_v B_v(T) + \eta_v S_v^d \quad (2)$$

for CS and

$$S_{v_0}^l = (1 - \varepsilon_{v_0} - \eta_{v_0}) \overline{J_{v_0}} + \varepsilon_{v_0} B_{v_0}(T) + \eta_{v_0} S_{v_0}^d \quad (3)$$

for CRD with $\overline{J_{v_0}} \equiv (1/4\pi) \iint I_v \varphi(v-v_0) dv d\Omega$ the “mean mean” intensity averaged over all directions and the line profile, with v_0

⁴³ $\sqrt{\varepsilon}$ law. This key law says $S_v(0) \approx \sqrt{\varepsilon_v} B_v(T)$ at the top of an isothermal constant- ε 2-level-atom plane-parallel non-irradiated atmosphere [RTSA Eq. 4.81 (pdf 117)], as shown in Avrett’s [RTSA Fig. 4.21 (pdf 128)]. The emergent intensity [RTSA Eq. 4.84 (pdf 117)] is similarly low: scattering lines get very dark. [It seems a straightforward result from simple linear-looking Eq. 2 and Eq. 3 for such a simple atmosphere – but Hubeny (1987b, 1987a) renamed it the Rybicki equation and analyzed why and how it works which I did not understand. I added two pages explanation [RTSA discussion (pdf 117)] which C. Zwaan said he did not understand. I also taught the definition of ε wrongly in IART (now correct in [IART Eq. 7.10 (pdf 101)]) until I finally grasped that the cancellation of c and g even applies to Thomson scattering.]

⁴⁴ Strong-line $B(\tau)$ flattening. Avrett’s ALC7 “chromosphere” (more below) is near-isothermal [SSX (pdf 72)] with near-constant ε in lines as Na I D₁ [SSX (pdf 80)] from increasing hydrogen ionization and hence near-constant (relatively increasing) electron density defining the collision frequency handling destruction pair a. The gas density drops exponentially outward [SSX (pdf 72)] but electrons dominate the collision frequency by moving much faster than atoms. Avrett’s canonical isothermal + constant $\sqrt{\varepsilon}$ demonstrations [SSF (pdf 80)] therefore apply well to ALC7. In addition, strong lines experience an atmosphere as more isothermal than the continuum because their total τ scales are compressed in height with respect to the continuum τ scale due to their steeper buildup [SSF (pdf 38)], flattening their $B(\tau)$ gradient [SSF (pdf 85)]. Where the temperature decays obeying radiative equilibrium as in the upper photosphere (note 65), lines see yet shallower B_v gradients. Hence line core darkening by $\sqrt{\varepsilon}$ scattering applies to most strong lines.

⁴⁵ An online tool for hands-on experimentation with various methods is at <http://rttools.irap.omp.eu> and described by Lambert et al. (2016). It produces plots as [RTSA Fig. 5.2 (pdf 147)] on your screen.

the line-center frequency and also used as line identifier. The first term in Eq. 2 and Eq. 3 represents the reservoir of photons that contribute new photons to the beam by direct scattering (f and g), the second describes collisional beam-photon creation (d and e), the third the contribution of new beam photons via detours (i and j) which themselves may contain collisional, scattering and also such bound-free steps.

Equation 2 and Eq. 3 show that LTE $S = B$ equality holds when $\varepsilon = 1, \eta = 0$ and/or $J = S^d = B$, both very closely correct below the standard $h=0$ surface at $\tau_{5000}^c = 1$. Above it ε becomes small⁴⁶ from lower electron density while η is usually smaller.⁴⁷ Most chromospheric lines and bound-free continua are heavily scattering with $S \approx J$ (but free-free continua always have $S = B$ because each interaction is collisional).

Transfer equation along the beam. See [ISSF Sect. 3.3 (pdf 10)] for a gentle introduction. Here τ_v is optical thickness measured in the beam direction. [ISSF Fig. 5 (pdf 14)] treats a spectral line from a homogeneous isothermal cloud with LTE processes, say a galactic HI cloud showing the 21-cm line to a

⁴⁶ *Epsilon is small* = T-shirt slogan for this course: $\varepsilon \approx 10^{-2} - 10^{-6}$ for Na I [SSX (pdf 80)], Ca II K [SSX (pdf 88)], Mg II k [SSX (pdf 89)], Ly α [SSX (pdf 90)] making the line source function mostly J hence NLS. For estimating emergent intensity with the Eddington-Barbier approximation you need to know the local intensity in all directions defined by source function values elsewhere. If the $\eta_{v_0} S_{v_0}^d$ contribution is significant you also need to know the intensity in all directions in other transitions with other wavelengths. Worse, the same may hold for evaluating the $\tau_v(h)$ scale needed in your Eddington-Barbier evaluation or your line synthesis code or your “inversion” code. RT is easy only when LTE holds everywhere at all participating wavelengths for both S and α (or when there is no RT as in CE). The smallness of ε is also numerically challenging. The source term εB may seem neglectable but it isn’t because without it there are no photons to scatter. In the early days of electronic computing it was tempting to stop Λ iteration [SSF (pdf 101)] when the convergence reached tiny steps – but they were not negligible because still far from the answer [SSF (pdf 103)]. This was remedied by operator splitting in approximate Λ iteration [SSF (pdf 102)] and convergence acceleration [SSF (pdf 103)]. Also, at very small ε the up and down radiative rates may be very large but nearly cancel; then using their “net radiative bracket” normalized difference can be numerically better and useful (Thomas 1960, Eq. 6.75 ff (pdf 151) of Jefferies 1968, Eq. 10 (pdf 6) of Carlsson & Stein 2002).

⁴⁷ *No Thomas photoelectric control*. H α has a sizable ηS^d contribution from bound-free detours as the loop shown in Fig. 2 (pdf 4) of Rutten (2019). It was famously called “photoelectric control” by Thomas (1957) with a schematic source function diagram in Fig. 3 (pdf 5) of Jefferies & Thomas (1959) that was reprinted in Fig. 12-9 of Mihalas (1970) and Fig. 11-11 of Mihalas (1978). It looks similar to the H α source function in [SSX (pdf 76)] with S_v^l leveling out in the photosphere higher than B_v in the temperature minimum, indeed similarly to the Balmer continuum [SSX (pdf 76)] – but the “photoelectric control” designation was wrong because even this complex line is mostly scattering as shown in Fig. 12 (pdf 9) of Rutten & Uitenbroek (2012); the upper-photosphere excess is due to backscattering from the chromosphere. Such excess does not occur in the RE atmosphere at left in Fig. 7 (pdf 6) of Rutten & Uitenbroek (2012) whereas with “photoelectric control” by ηS^d it should since the ultraviolet continua in Fig. 5 (pdf 5) there have similar $S \approx J > B$ excess with or without a chromosphere. It was a red herring. There are some lines as the Mg II triplet around Mg II h & k for which source function enhancement in cooling recombining gas (possibly non-E) producing emission is likely, but the frequent Thomas-citing characterizations of H α as “photoelectric” were misled. H α is instead sensitive to non-E opacity boosting in cooling recombining gas (note 94) that controls the location of its $\sqrt{\varepsilon}$ source function decay (note 76).

radio astronomer. Of my cartoon diagrams this one is most often shown, nowadays as Python animation. Appreciate how the line grows or sinks with increasing cloud opacity until it hits the $I_v = S_v = B_v$ optically thick limit. Thick isothermal LTE clouds show no lines (as black holes have no hair).

Such simple clouds⁴⁸ became the basis for “cloud modeling” started by Beckers (1964) in his thesis (put on ADS by me) for $H\alpha$ mottles on the disk and also much used for filaments. Assuming the cloud homogeneous with Gaussian (“microturbulent”) line broadening yields the classic cloud parameters [SSX (pdf 2)]: line-center optical thickness, line-of-sight velocity, source function, Doppler width, incident intensity profile from below/behind (review Tzotziou 2007).⁴⁹

Transfer equation in optical depth. For very optically thick objects (as the Sun) there is no interest in what impinges the other side since nothing comes through. We then flip τ to measure optical depth instead, either against the line of sight (τ_{ν}) or more often against height radially into the Sun. The standard recipe is then to apply the Eddington-Barbier⁵⁰ approximation as indicator of “height of formation” [ISSF Eq. 35 (pdf 13)], [IART 321 (pdf 45)], [RTSA Eq. 2.44 (pdf 38)], [RTSA Eq. 4.32 (pdf 106)], [SSF (pdf 29)] and [SSF (pdf 51)]. The “four-panel” diagrams in [SSF (pdf 31–38)] are a cartoon course on Eddington-Barbier spectrum formation with increasing complexity. You should blink the absorption–emission pairs by full-page flipping.

Be aware that the Eddington-Barbier approximation may fail miserably: do the exam on [SSF (pdf 40)], first for Na I D₂ (answer $h \approx 500$ km) and then for the blend. If you find $h \approx 150$ km for the blend by reading off where its center intensity equals

⁴⁸ *Coronal clouds.* The simplest clouds are fully transparent as CE assumes for coronal structures, e.g., loops. No RT whatsoever. In optically-thick RT terms: the homogeneous-cloud solution [ISSF Eq. 5 (pdf 13)] has incident intensity $I_v(0) \approx 0$ so $I_v(D) \approx S_v$, $\tau_v(D) = j_v D$ with D the geometrical cloud thickness along the line of sight. This holds for Thomson scattering producing the white-light corona (with $S_v \approx J_v$) and also for locally thermally created EUV radiation. In terms of Eq. 2 for the latter (applicable if we count escaping photons into α_v^d with $\eta_v^d \approx 1$ for CE) both $J_v \approx 0$ and $S_v^d \approx 0$ so that $S_v^l \approx \varepsilon_v B_v(T)$ or $j_v^l \approx \alpha^a B_v(T)$ with exceedingly small α^a and ε_v due to absence of collisional deexcitation. Even though all line photons are thermally created the intensity stays far below saturation to the Planck function for lack of local enclosure. The corona is far hotter than the photosphere and its radiation is thermal and defined by its temperature just as for the optical continuum from the photosphere [SSI (pdf 4)] – but in contrast to the photosphere the corona radiates far below its thermal capacity because it lets photons depart instead of boxing them in.

⁴⁹ *Sophisticated clouds.* Cloud complexity was added by e.g., Molowny-Horas et al. (1999) (model look-up tables for “inversion”), Heinzel et al. (1999) and Mein et al. (1996) (source function variation along the line of sight; this was already done by Beckers (1968) in a famous spicule review by using NLTE population tables for hydrogen from Giovanelli (1967) although warning against assuming SE below Eq. 10 (pdf 32)), Chae (2014) (second cloud model for the incident profile), Heinzel et al. (2015) (multi-thread RT with mutual irradiation). For the incident profile often a field average or a nearby subfield average is used but this is wrong in the case of backscattering as observed for $H\alpha$ filaments as sub-filament brightening towards the limb by Kostik & Orlova (1975), proposed for $H\alpha$ fibrils by Al et al. (2004), and occurring in 1D standard models (note 47). The near-equality of the dashed profiles in the lower panels of their Fig. 8 (pdf 7) made Rutten & Uitenbroek (2012) suggest the recipe (pdf 9) to use the outward intensity profile in a RE model at optical depth equal to the cloud’s thickness as impinging background profile. This recipe improves the finding of Bostanci & Al Erdogan (2010) that a RE emergent-intensity estimate works best.

⁵⁰ Unjustly named (Palletou 2018) – as more often with Eddington.

the source function just as for Na I D₂ you are a million times wrong.⁵¹

Be also aware that solar-atmosphere structures may be optically thick without being effectively thick so that radiation scatters through. Filaments or fibrils may appear intransparent in $H\alpha$ while illumination from behind is still important. This is even the case for $H\alpha$ in the “chromosphere” plateau of 1D standard models, as in [SSX (pdf 91)] which not only shows $S \approx J > B$ across the model temperature minimum from backscattering treated in note 47 but also has photospheric photons scattering through the model chromosphere. This caveat was beautifully demonstrated in Fig. 7 (pdf 7) of Leenaarts et al. (2012a) by comparing 1D $H\alpha$ synthesis for a Bifrost (note 82) simulation with MULTI⁵²

⁵¹ *Na I D, Mg Ib, Ca II 8542 Å heights.* [Spoiler: million difference in line identification [SSF (pdf 41)].] The same Fig. 4 (pdf 5) of Uitenbroek & Bruls (1992) is also the subject of less simple but recommended [RTSA Problem 7 (pdf 250)] on Na I D₂ line formation in the FALC star (Sect. 6). [Spoiler: my answers to most RTSA problems.] The Na I D lines are often called chromospheric. Your Eddington-Barbier estimate $h \approx 500$ km with [SSF (pdf 40)] puts the Na I D₂ formation just above the temperature minimum of the FALC star, but the line source function shows a $\sqrt{\varepsilon}$ scattering decline as if the FALC star has no non-RE heating whatsoever. The photons emerging there were made much deeper, near thermalization depth in the photosphere, and scattered out from there ignoring the temperature rise until their escape. Intensity variations of the core therefore correspond to photospheric temperature variations, not at the $\tau \approx 1$ Eddington-Barbier estimate. However, in measuring Doppler or Zeeman modulation the latter estimate may be more appropriate because these signals are encoded at the last scattering. Similar FALC results in Fig. 13 (pdf 11) of Rutten et al. (2011) compare Na I D₁ formation with Mg Ib₂ and Ca II 8542 Å formation. Mg Ib₂ forms similar to Na I D₁, decoupling slightly higher, but the source function of Ca II 8542 Å decouples above the FALC temperature minimum higher and does convey chromospheric signature. The same is seen for the ALC7 star in comparing [SSX (pdf 85)] [SSX (pdf 84)] [SSX (pdf 87)] with S , B , J graphs that also show optical depth locations, destruction probabilities, thermalization lengths and decoupling heights ([SSX (pdf 80)], note 66). Rutten et al. (2011) used high-quality SST observations to compare the three lines in intensity in Fig. 4 (pdf 5) in comparison with simulation results in Fig. 5 (pdf 6) and those smeared to observation-resolution in Fig. 6 (pdf 7), and then observed and simulated line-core Dopplergrams in Fig. 7 (pdf 8). These figures confirm non-chromospheric sampling by Na I D₁ and Mg Ib₂ whereas Ca II 8542 Å does show chromospheric signatures (note 94). The main difference between the first two is that the Na I D lines have higher Doppler sensitivity than the Mg Ib lines by having narrower cores with steeper flanks. This explains the observed difference between their wings in sampling upper-photosphere reversed granulation in Fig. 1 (pdf 2) and also makes Na I D Dopplergrams a sharp proxy for localizing upper-photosphere shocks in MCs, as summarized in [SSX (pdf 54)] repeating the corollary on page 15 (pdf 15) of Rutten et al. (2011) that Fourier analysis of full-disk Doppler sampling with the proposed GOLF-NG space instrument (Turck-Chièze et al. 2012) will not achieve chromospheric helioseismology as advertised, whereas hoped-for g -mode detection will be hampered by upper-photosphere reversed granulation, fluxtube shocks and “shutter” modulation by overlying features as in Figs 5 and 6 (pdf 6) of De Wijn et al. (2007).

⁵² *MULTI program.* NLTE spectral synthesis code of Carlsson (1986) obviously named for going beyond the 2-level approximation. It initially used linearization following Scharmer & Carlsson (1985) with the brilliant Scharmer operator [RTSA Eq. 5.52 (pdf 148)] [yes, the same as the brilliant SST builder] to obtain I_v rather than J_v from S_v with a local Eddington-Barbier approximation. It was later extended with the faster combination of the diagonal [RTSA OAB operator (pdf 150)] of Olson et al. (1986) and [RTSA convergence acceleration (pdf 150)] of Ng (1974).

and 3D $H\alpha$ synthesis with MULTI3D⁵³. In the columnar 1D line synthesis the deep-photosphere granulation is better visible than lower-contrast chromospheric fibrils but in 3D synthesis the granular contrast is smoothed away by sideways scattering.

The most important equation of classical 1D 2-level scattering is the Schwarzschild equation defining the Λ operator [RTSA Eq. 4.14 (pdf 98)]; a synopsis is given in (pdf 9–10) of Rutten (2019). Its cutoff at the surface produces outward $J_\nu < S_\nu$ divergence for small inward increase of $S_\nu(\tau_\nu)$ but outward $J_\nu > S_\nu$ divergence for steep increase [RTSA Fig. 4.2 (pdf 100)], [RTSA Fig. 4.4 (pdf 103)], [RTSA Fig. 4.9 (pdf 121)]. Be aware that steep horizontal gradients are similarly important in 3D radiative transfer. Steep horizontal gradients occur for example already in the photosphere in and above granulation and in and around MCs constituting network and plage. Obviously they occur in and around the multitude of small dynamic structures constituting the higher atmosphere.

[SSF (pdf 108)] gives a summary of the key line formation equations.

4. LTE: Holweger models

The classic Holweger models⁵⁴ (Holweger 1967 and HOLMUL of Holweger & Müller 1974) were a pinnacle of solar LTE interpretation. They replaced curve of growth⁵⁵ abundance determination by numerical abundance determination. They ignore the existence of the solar chromosphere to avoid self-reversals in strong optical lines⁵⁶, but nevertheless HOLMUL became

⁵³ MULTI3D program. Extension of MULTI to 3D parallel computation by Leenaarts & Carlsson (2009). It uses short characteristics with further-away contributions corrected by iteration.

⁵⁴ Holweger modeling, classical abundance determination. Holweger used the ALGOL “Kieler program” of Baschek et al. (1966) for LTE spectral synthesis in a classical approach: impose a $T(h)$ “model” relation, evaluate density stratifications for the given element mix by assuming hydrostatic equilibrium [RTSA Sect. 7.2.3 (pdf 166)], compute continuum extinction from H^- and extinction of a given line per SB ($b_u = b_l = 1$ in [RTSA Eq. 9.6 (pdf 224)]), integrate the transport equation to obtain the emergent profile. He used the area (“equivalent width” [RTSA Sect. 9.1.2 (pdf 224)]) as quality gauge, repeated this for many optical lines, and derived a best-fit temperature stratification by trial-and-error manual $T(h)$ adjustment. Most analyses using his models (a large “abundance determination” industry during decades) employed critical ad-hoc adjustment parameters: fake line broadening for duplicating observed line broadening with “microturbulence” (adding height-dependence as in Fig. 11 (pdf 19) of Vernazza et al. 1981) and “macroturbulence” (with “radial-tangential” anisotropy added by Gray 1977), and fake wing extension with a collisional damping “enhancement factor”.

⁵⁵ Treated in practical SSA 3 (pdf 28). Fig. 4 (pdf 6) of Rutten & Zwaan (1983) may have been the last solar Fe I one.

⁵⁶ Mg I 12-micron emission lines. Assuming LTE implies self-reversing chromospheric cores in e.g., the Na I D lines treated in practical SSB 3 (pdf 22) but also in the strong Fe I lines that Holweger employed. Their absence was attributed correctly to NLTE scattering by others but Holweger insisted tenaciously that NLTE computer programs fatally overestimate NLTE departures by not including sufficient hydrogen-atom collisions and that the actual chromosphere starts higher. When he refereed Carlsson et al. (1992) explaining the enigmatic Mg I emission lines at 12 micron this was also his main complaint, but the Rydberg recombination modeled there was already collision-dominated. The formation of these striking features is interesting. Naturally they were first attributed to chromospheric formation (Brault & Noyes 1983) but they are photospheric, combining NLW photon pumping (photo-ionization), NLW photon suction (recombination driven by strong-line photon loss) and a diffusive radiative-collisional Rydberg

highly popular⁵⁷ with abundance determiners because it worked so well, giving them smaller spread for multiple lines than other standard models. No wonder because the model was made as best fit to photospheric lines, in particular of Fe I, so that fitting similar lines with the model was a self-fulfilling prophecy, in particular for the then much debated Fe abundance itself (e.g., Kostik et al. 1996). Earlier Rutten & Kostik (1982) showed that such model production is also self-correcting through “NLTE masking”.⁵⁸

So-called “inversion” codes (I find “best-fit” better suited) are automated versions of Holweger’s trial-and-error model derivation procedure.⁵⁹ Copying Holweger’s fads also copies the fallacies including NLTE masking, an important failure because NLTE scattering in the ultraviolet bound-free edges controls the opacity of minority-species atomic lines throughout the spectrum. In the optical these often have source functions close to LTE through interlocking⁶⁰ but their interlocked opacities have

population departure flow. In the Rydberg top this is dominated by collisional decays, the opposite of the coronal dielectronic radiation-down case of note 29. See the cartoon explanations in Rutten & Carlsson (1994) including Mats’ “Rydberg flows for kayakers” in Fig. 4 (pdf 7) [better quality]. Actually, Lemke & Holweger (1987) had come close to model these emission lines properly except that their Mg I model atom did not reach high enough. Their paper was wildly and wrongly attacked by Zirin & Popp (1989), in turn severely rebutted by me in Carlsson et al. (1992). This impressed Zirin so much that he saw me as potential successor. I saw him as thin because in the abstract he stated that these Mg I lines are thin. They are not in his sense, but that itself is a no-no because lines cannot be thin (define a halfwidth threshold in Å or km s⁻¹). A solar-atmosphere structure can be thin or thick or effectively thick in a line (maybe the Sun is thin in neutrino lines) but no line is thin or thick. Never say “this line is thin” or earn my scorn!

⁵⁷ ADS shows 900+ citations but declining rate since 2009.

⁵⁸ NLTE masking. For a steep outward temperature decline the outward increasing ultraviolet $J > B$ excess from scattering and Λ results in NLW-type NLTE overionization of minority-species metals [SSF (pdf 111)]. Instead adopting Saha ionization then puts the height assigned to $\tau = 1$ too high so that the fitted temperature gradient gets too shallow and the same as for locations with less steep temperature decline. Different surface structures with different gradients (as granules and lanes) can so be fitted by a single shallow gradient. Additionally, the neglect of source function NLTE for higher-up scattering in stronger lines results in undoing an actual chromospheric temperature rise, masking that also. Fig. 8 (pdf 8) of Rutten & Kostik (1982) shows how a HOLMUL-like model so results from the steeper-gradient HSRA model of Gingerich et al. (1971); a cartoon is shown in Fig. 4 (pdf 14) of Rutten (1988).

⁵⁹ Milne-Eddington approximation. Inverters often apply the further simplification of assuming Milne-Eddington line formation, i.e., constancy of the line-to-continuum extinction ratio with height. This assumption was tested with a MURaM simulation and LTE line synthesis for comparable weak Fe I lines at different excitation energy in Fig. 8 (pdf 10) of Vitas et al. (2009). It is bad at low excitation, better at higher excitation.

⁶⁰ Interlocking: $S = B$ Fe I lines, weak Ce II and Fe II emission lines.

Grotrian diagrams of e.g., Fe I and Fe II are very rich in bound-bound transitions. Optical multiplets are mostly high up but connected by ultraviolet transitions to levels lower down (ground state or low-lying metastable levels). These transitions tend to be strong maintaining $S' \approx B$ further out as in cartoon [SSF (pdf 111)], forcing $b_u \approx b_l$ on their upper levels at the deeper heights where their weaker optical siblings reach $\tau \approx 1$. When the latter lines so share strong-line b_l in their upper and lower levels they have LTE source functions. Other interlocking examples are lines from lanthanide rare earths. They have multiplets with many members that overlap closely in energy. Ce II has most lines, peaking at 10 lines/Å around Ca II H & K. These lines are weak lines but scatter strongly with much crosstalk. They show up in emission in-

NLTE deficits up to an order of magnitude from ultraviolet over-ionization set by steep temperature gradients in deeper layers.⁶¹ This fallacy has been long ignored but was at last addressed by [Smitha et al. \(2020\)](#). Worse: in the actual 3D solar photosphere matter and radiation gradients also occur and act horizontally, requiring 3D line synthesis (cf. [Smitha et al. 2021](#)). Proper quantification of such ultraviolet extinction control is severely hampered by the dense ultraviolet line haze with its own NLTE properties ([Fig. 10 \(pdf 18\)](#) of [Rutten 2019](#)). Stronger lines need NLTE modeling not only for their extinction but also for their source function set by their own scattering or by non-2-level de-tour transitions. When “inversion” codes are proudly advertised as NLTE usually only the modeled-line resonance scattering is meant, not the extinction-affecting scattering in the bound-free continua nor resonance scattering in the line haze affecting those.

Holweger’s assumptions of 1D modeling, LTE and no chromosphere were also revived in SATIRE irradiance modeling for network and plage ([Unruh et al. 1999](#)) which therefore suffers similarly from mistreating the opacity-affecting NLTE ultraviolet continua and their NLTE line haze. More explanation in [Sect. 4 \(pdf 11\)](#) of [Rutten \(2019\)](#).

The Asplund revolution ([Asplund et al. 2009](#), 5000+ citations) ended the HOLMUL popularity, not so much as an LTE dismissal but by including granulation ([Nordlund et al. 2009](#)). Its main effect is that its temperature inhomogeneity upsets the notion that spatially-averaged intensity may be modeled as spatially-averaged temperature because at optical and shorter wavelengths this notion is undone by the Wien nonlinearity of the Planck function ([Uitenbroek & Criscuoli 2011](#)). In addition simulated granulation undid the “microturbulent” and “macro-turbulent” faking, and better atomic physics ([Barklem et al. 2000](#)) undid the “damping enhancement” faking.

5. NLS: Auer & Mihalas modeling

NLS is the realm of 2-level modeling treated extensively in [\[RTSA Chapt. 4 \(pdf 95\)\]](#), numerical developments around the Λ operator summarized in [\[RTSA Chapt. 5 \(pdf 133\)\]](#), and numerical PRD formalisms (not yet in RTSA). [\[SSF \(pdf 111\)\]](#) shows a cartoon summary also shown as [Fig. 4 \(pdf 10\)](#) of [Rutten \(2019\)](#) and discussed in [Sect. 4 \(pdf 11\)](#) there. Non-local scattering makes J depart from B in setting S according to [Eq. 2](#) and [Eq. 3](#), for bound-free continua and for lines of increasing strength (or different parts of strong PRD lines). The ultraviolet continua gain $S \approx J$ excess over the photospheric B decline per Λ [\[SSF \(pdf 86\)\]](#). Strong lines obtain low S per Λ from $\sqrt{\epsilon}$ scattering by seeing actual temperature gradients as near-isothermal from τ scale compression ([note 44](#)).

side the limb both outside and within the extended wings of Ca II H & K which was explained in the classic analysis of [Canfield \(1971b\)](#) following on [Canfield \(1971a\)](#) and his earlier thesis studies. They appear bland from wide multi-wavelength scattering producing their J , whereas similar Fe II blends in the wings of H & K show much spatial variation due to pumping by particular ultraviolet transitions ([Cram et al. 1980](#), [Rutten & Stencel 1980](#)).

⁶¹ *Fe I 6302 Å doublet, Mg I 4571 Å*. A good example is the Fe I 6302 Å polarimetry doublet [\[SSX \(pdf 83\)\]](#). Their “inversion” should use RH ([note 68](#)) with a large Fe model atom, sizable electron-donor atoms and a suited line-haze recipe or it will mistreat their opacities. Another good example is Mg I 4571 Å which is a forbidden transition and therefore has $S = B$ up to large height but suffers considerable extinction NLTE even in 1D modeling [\[SSX \(pdf 82\)\]](#). “Inversion” fitting needs a large Mg model atom plus the other electron donors and a line-haze recipe.

I advertise the classic warm-star HI analyses of Auer & Mihalas (1969a, 1969b) here. They were an early pinnacle of 2-level modeling.⁶² Not purely 2-level since adding the HI continuum level and so including the Lyman and Balmer continua to Ly α in the first paper and to H α in the second. The key results were copied in [Mihalas \(1970\)](#) and in [\[RTSA Fig. 7.10 \(pdf 187\)\]](#). The great didactic value of their results is that the effects of these transitions are well separated in height. “Big whopper” [\[RTSA exercise 12 \(pdf 254\)\]](#) poses five pages of hard questions on their graphs that I challenge you to answer⁶³. The hardest is to understand: “Amazingly, the photon losses in the subordinate Balmer- α line, located in the low-energy red part of the spectrum, cause heating of the whole outer atmosphere of this hot star.” [\[RTSA \(pdf 189\)\]](#). Because their graphs did not include J we did a multi-level re-do including Avrett-style *S, B, J* graphs ([pdf 5](#)) and radiative heating/cooling graphs ([pdf 6](#)) in [Wiersma et al. \(2003\)](#), giving as answer: “The photon losses in Ba α suck population from the proton reservoir through a collisionally-dominated Rydberg recombination flow and so boost the outward temperature rise.” ([pdf 7](#)). All yours to understand.

6. NLS+NLW: Avrett stars

The various Avrett models⁶⁴ (VALIIM of [Vernazza et al. 1976](#), VALIIC of [Vernazza et al. 1981](#), MACKKL of [Maltby et al.](#)

⁶² I wonder what Unsöld, who at Kiel had told Holweger to produce a thesis proving that LTE suits the solar spectrum, made of these. In 1967 he wrote to Minnaert that Holweger had indeed definitely proven the LTE veracity of the solar spectrum, in a recommendation for the “International Study week” at the Bilderberg Hotel [famous from more famous Bilderberg Conferences] that [De Jager](#) organized in order to jointly derive the Bilderberg Continuum Atmosphere of [Gingerich & de Jager \(1968\)](#) that later got improved to the HSRA by [Gingerich et al. \(1971\)](#). As student I operated the slide projector and later described this truly expert meeting in [Rutten \(2002\)](#) with a nice [group photo \(pdf 5\)](#) also sporting Holweger [more photographs at the bottom of [my astronomershots](#)]. E.A. Müller commented that she wouldn’t use the new model but stick to Holweger’s model and LTE, then did so with HOLMUL ([Holweger & Müller 1974](#)). However, the Auer–Mihalas results did upset Unsöld’s bible “*Physik der Sternatmosphären*” ([Unsöld 1955](#), 900+ citations) which was translated by H. Panovsky and A.K. Pierce but never printed because Unsöld insisted that any astrophysicist could and should learn German to read his book.

⁶³ [Spoiler: [my answers](#) to most RTSA problems including this one.]

⁶⁴ *Pandora program*. NLTE spectral synthesis code of [Avrett & Loeser \(1992\)](#); more [here](#) and [here](#) and [here](#). It is similar to Holweger’s program in applying hydrostatic here and equilibrium to a trial manually-fitted $T(h)$ temperature stratification but uses SE NLTE for radiation evaluation in a giant “equivalent two-level” iteration loop treating each bound-bound or bound-free transition that is explicitly taken into account (not added as background opacity) with two-level rate equations, letting iteration take care of multi-level crosstalk. The equation system is large enough to earn the [ominous name](#). Whereas Holweger concentrated on fitting observed optical lines, most from Fe I, Avrett concentrated on fitting observed disk-center continua, especially in the ultraviolet. These are affected by line crowding (the “veiling line haze” of [Labs & Neckel 1972](#) and [Greve & Zwaan 1980](#)) so that Avrett added increasing numbers of lines from the ever-growing list of [Kurucz \(2009\)](#) and treated them with an imposed ad-hoc gradual source function transition from $S = B$ in the model photosphere to $S = J$ in the model chromosphere to avoid non-observed core reversals that occur in LTE sampling above the temperature minimum ([page 243 ff. \(pdf 15\)](#) of [Avrett & Loeser 2008](#)). The line haze was most comprehensively handled brute force in [Fontenla et al. \(2015\)](#) by solving NLTE population equations for many transitions, doable only in single-shot 1D modeling. Fontenla diverged from Avrett after [Fontenla et al. \(1993\)](#), writing a Pandora alternative

(1986), FALC of Fontenla et al. 1993 and ALC7 of Avrett & Loeser (2008) with an update in Avrett et al. 2015) are all classic pinnacles of plane-parallel (1D) NLTE modeling (2100⁺ citations and steepening for VALIIC). Their strength is comprehensive inclusion of ultraviolet transitions. Their weakness is ignoring Wien nonlinearity in assigning observed intensities to averaged temperatures of inhomogeneities, the same mistake as in HOLMUL abundance determination rectified in the hydrodynamic Asplund revolution. Practical SSB 1 (pdf 5) dissects the FALC stratifications with comparison to our own atmosphere which is transparent to sunlight by missing H^- (did you miss it?) treated in the continuum part of SSI and in practical SSB 2 (pdf 13). SSB 3 (pdf 22) makes you synthesize the Na I D lines from FALC assuming LTE and hence misrepresenting their cores.

NLW was still lacking in VALIIM which only accounted for scattering in the Si I continuum so that its Fig. 23 (pdf 38) multi-page analogon to multi-page VALIIC Fig. 36 (pdf 33) shows erroneous $S_\nu \approx B_\nu$ above the Si I threshold at 1682 Å where other electron-donor bound-free contributions dominate. This was remedied in VALIIC but overestimating their effect because not enough line-haze blending lines were included, resulting in a too steep upper-photosphere temperature decline. Including more and more lines from the Kurucz tabulations then brought the upper-photosphere back up in MACKKL and since then it has remained the same. It is remarkably similar to HOLMUL and even to Kurucz or Uppsala LTE-RE models [RTSA Fig. 7.3 (pdf 169)].⁶⁵

I love the Avrett models, in particular VALIIC because of the many diagrams in Vernazza et al. (1981) and especially its many-page Fig. 36 (pdf 33) continuum formation diagrams (some copied in [RTSA (pdf 204)] – [RTSA (pdf 206)]). Since VALIIC obeys all the standard RT equations, meaning all those in RTSA, these graphs describing spectral continua arising from the VALIIC density and temperature stratifications provide valuable insights on spectrum formation and its intricacies. They are of enormous didactic value because *everything* in Avrett's

and adding tricks to enhance output similarity to the non-1D non-static non-SE spectra of the actual Sun. First he invoked the Farley–Buneman instability to warrant adding ad-hoc artificial pressure (the Avrett stars use *observed microturbulence* (pdf 19) for turbulent pressure); later he mucked gravity ad-hoc to extend the model chromosphere to reproduce CO lines that probably have 3D(t) NLT formation (Uitenbroek 2000). I prefer the ALC7 star of Avrett & Loeser (2008) for my spectrum-formation demonstrations [SSX (pdf 72–140)]. It isn't the Sun but it is self-consistent within its RTSA physics and well-suited to showcase this physics. Pandora is *web-available* but documented only in many pages of coding requests and specifications to R. Loeser that reside in Avrett's CfA office [P. Heinzel holds copies in Ondrejov].

⁶⁵ *RE upper photosphere.* The reason is that the upper photosphere is the most homogeneous domain of all. The granular convection has stopped whereas acoustic waves do not yet shock. Magnetic fields are still mostly confined to slender fluxtubes at small density in the modeled “quiet” areas. Gravity waves do not yet couple into them (note 72). In addition, the bulk of the escaping solar radiation is in the optical and forces radiative equilibrium. In “grey” RE [RTSA Sect. 7.3.2 (pdf 173)] the continuum gets gradient $S(\tau) \sim (1 + 1.5 \tau)$ [RTSA Eq. 7.43 (pdf 176)] because for that gradient $\Lambda(S) \approx S$ [SSF (pdf 45)]. The continuum in the optical is dominated by H^- which has near-LTE $S_\nu \approx B_\nu$ in the bound-free range and strict LTE $S_\nu = B_\nu$ in the free-free range. Most lines in the optical also have $S_\nu \approx B_\nu$ because they share levels with stronger ultraviolet lines still having $\tau_\nu > 1$, still locked in and forcing balancing for the whole multiplet. Hence the temperature gradient is set LTE-wise by the RE condition [RTSA Eq. 7.33 (pdf 174)]. Indeed, more modern Bifrost simulations obtain about the same average temperature decay with relatively small spread at these heights [SSX (pdf 59)].

output graphs is fully understandable from the input physics \approx RTSA physics. The same holds for the newer Avrett models and his latest ALC7. Therefore I made many ALC7 demonstration figures: [SSX (pdf 73)] showing ALC7 stratifications, [SSX (pdf 76)] ultraviolet continua, [SSX (pdf 77)] hydrogen line formation, [SSX (pdf 77)] overview of strong-line formation, then [SSX (pdf 78–81)] explaining line-formation plots⁶⁶ followed by such plots for thirteen ALC7 lines in [SSX (pdf 82–94)]. They were all made with IDL⁶⁷ with the 1D version of the github-public RH program.⁶⁸ They represent a detailed view of how all these lines form in the ALC7 atmosphere. Any student of thick solar spectrum formation should be able to understand and appreciate all these curves in all their gory detail. I invite you to study and explain:

- N_e stratification;
- Eddington-Barbier validity in all lines;
- ε decline in scattering lines;
- PRD-split source functions of Ba II 4554, Ca II K, Mg II k, Ly α ;
- thermalization depth for all lines, in particular H α ;
- NLTE extinction dip of Mg I 4571, Fe I 6301.5, Mg I b₂ but not for Na I D₁, He I 10830;

⁶⁶ *ALC7 line formation plots, departure coefficients.* These triples show populations, source functions, emergent profiles in fixed formats used for all plots. The explanations are for Na I D₁. The first plot [SSX (pdf 79)] shows lower and upper level population departure coefficients $b \equiv n/n_{\text{LTE}}$ which have $a^l \approx b_l a_{\text{LTE}}^l$ and $S_{\nu_0}^l \approx (b_u/b_l) B_{\nu_0}(T)$ [SSF (pdf 73)]. The other curves are NLTE and LTE fractional populations. Their divergence follows the $\log(b_l)$ departure from zero. The second plot [SSX (pdf 80)] shows B , J and S^l [they must always be shown all three]. They are on equivalent temperature scales [SSF (pdf 72)] to enable comparisons between different lines across the spectrum by undoing nonlinear Wien temperature sensitivity. On logarithmic intensity scales the S^l separations from B would equal the logarithmic separations of b_u from b_l in the first plot. The thick solid curve usually lies between the other two, identifying it as S^l obeying $S^l \approx (1 - \varepsilon) J + \varepsilon B$. For PRD lines it is split between monofrequent samplings. The $\log(\tau)$ marks are defined by the lower-level fractional population, abundance and density drop. The other two curves measure scattering governing the separation between S^l and J . The third plot [SSX (pdf 81)] is the computed emergent profile on the same equivalent-temperature scale as the second plot to enable checking the Eddington-Barbier approximation. I did not add observed disk-center atlas profiles in view of the Ha–Ha formation in note 76: you might be tempted to interpret a good fit as solar-proven model truth.

⁶⁷ *My IDL programs.* These are webposted under my *Recipes for IDL* with this *inventory*. RH plot programs in *rhlib*, LTE line formation programs in *ltelib*, SDO alignment pipeline in *sdolib*, SST data-handling programs in *stlib*, image sequence browser *showex* in *imagelib*, etc. Installation is described in *this manual*. I even offer a *beginner IDL manual*.

⁶⁸ *RH program.* The RH spectrum synthesis code of Uitenbroek (2001) is named after Rybicki & Hummer (1992) and follows their scheme of multi-level approximate lambda iteration [RTSA Sect. 5.3.2 (pdf 145)] not iterating Λ for J_ν but the Ψ operator for J_ν . It permits overlapping lines, includes PRD and full-Stokes options, exists in 1D, 2D, 3D, spherical, and Cartesian versions, and more recently also in parallel multi-column “1.5D” (Pereira & Uitenbroek 2015). It has various options to treat the worrisome ultraviolet line haze, including the Zwaan-inspired Fig. 2 fudge (pdf 3) of Bruls et al. (1992). I used RH 1D version-2 with H, He, Si, Al, Mg, Fe, Ca, Na, and Ba active, C, N, O, S, and Ni passive, and with 20 mÅ sampling of 343 000 lines between 1000 and 8000 Å in the atomic and molecular line list of Kurucz (2009). Fig. 6 (pdf 13) of Rutten (2019) gives an overview of their extinction in the FALC star. The line haze is prominent between $\log \lambda = 3$ and 4. Results with two line haze treatments [both wrong] are in Fig. 10 (pdf 18) of Rutten (2019).

- LTE extinction of Mg II k, H α , H β , He I 584;
- slight rise in NLTE over-extinction for Ly α .⁶⁹

However – the stern caveat is that I love the Avrett models only for representing educational solar-analog “Avrett stars” [SSX (pdf 58)]. These computationally existing stars are infinitely plane-parallel extending (1D) without any inhomogeneities or any magnetism or any sort of waves or any type of reconnection – no granules, spicules, floccules, let be flares, CMEs, and whatever else that makes our kind Sun non-plane-parallel interesting. The Avrett stars are a marvelous boon to an RT teacher like me but they also had and have detrimental effects on far too many colleagues misled into accepting their stratifications as a valid average over small fluctuations around realistic means. VALIIC Fig. 1 (pdf 3) is a double champion of solar physics: the most-shown figure but also the most misinterpreted one. It misled many solar physicists into thinking it describes the Sun instead of an unrealistic plane-parallel-layer star. *The solar atmosphere is not layered but dynamically structured.*

Take H α as example. In VALIIC Fig. 1 (pdf 3) E.H. Avrett, admirably careful, drew its core coming from the VALIIC chromosphere, its wing from the low VALIIC photosphere with an extended gap in between that is not present in his formation spans of Ca II K and Mg II k. He did so because at low temperature the Boltzmann excitation and therefore the extinction of H α are negligible.⁷⁰ But the actual H α core in actual quiet Sun mostly samples fibril canopies that reach higher than the entire VALIIC star.

Worse, the VALIIC chromosphere and similar Avrett-star chromospheres do not represent average fibril temperatures but ultraviolet radiation temperatures reached in acoustic shocks in internetwork regions underneath H α fibril canopies. These radiation temperatures are Wien-weighted to the shock maxima and not linear temperature averages. This was shown in Fig. 4 (pdf 8) of Carlsson & Stein (1994) with the demonstration in Fig. 5 (pdf 11) that the nonlinear Wien weighting skews the apparent average to an Avrett-type apparent chromosphere, along

⁶⁹ *Menzel departure coefficients.* Various authors [not to be named] reversed the meaning of VALIIC Fig. 30 (pdf 29) into its b_1 curve implying chromospheric hydrogen ground-state population ten times the local gas density. Be aware that Avrett and Fontenla used the Menzel definition of departure coefficients described in VALIIC Eqs. 13–18 (pdf 29); they use the next-ion population as normalization. I use the more intuitive Zwaan definition [RTSA Eq. 2.104 (pdf 53)] using the total element population as normalization and used to write β_l and β_u following Wijbenga & Zwaan (1972). The values reverse for majority species as H I, which led Fontenla et al. (2009) to misinterpret their own results (Rutten & Uitenbroek 2012).

⁷⁰ *Quiet-Sun H α scenes.* Note the deep chasm in the dashed curve in the first panel of [SSX (pdf 91)], first described by Schoolman (1972). Observationally the gap is evident when you shift the SST/CRISP H α passband from line center to a wing for a quiet-Sun target. Up to about $\Delta\lambda = \pm 0.5$ Å the scene usually shows fibrils extending from network and then you suddenly drop into deep-photosphere granulation, skipping the middle and upper photosphere. Only in rare utterly quiet areas you may see somewhat higher-up reversed granulation near $\Delta\lambda = \pm 0.5$ Å. I offer two SST examples. The first is a very quiet target corner in the data of Ruppe van der Voort et al. (2007) in this Ca II H + H α blue-wing movie where reversed H α at $\Delta\lambda = -0.45$ Å shows reversed granulation as grey background pancakes. The second is a similarly very quiet target (in a disk-center coronal hole) that you may inspect yourself by doing my alignment practical teaching my SDO pipeline (note 87). Its showex commands for these SST data enable wing blinking against reversed granulation in Ca II 8542 Å to identify it in H α .

with their marvelous RADYN reproduction of actual internetwork shocks observed by Lites et al. (1993) in Fig. 14 (pdf 23).⁷¹

In AIA 1700 and 1600 Å movies acoustic waves in quiet internetwork regions causing such shocks higher up stand out as fast-moving fast-evolving wisps of emissivity amid stable network evident as bright grains representing kilogauss “flux-tube” MCs. The internetwork wisps represent upward propagating waves excited by the 3-min components of the photospheric p -mode interference pattern. The 1600 Å images sample them slightly higher because the summed photo-ionization extinction of electron donors Mg I, Fe I, Si I, and Al I increases for shorter wavelength (VALIIC Fig. 36 (pdf 33 ff)). This increase produces the Fourier phase differences in the upper panel of Fig. 18 (pdf 18) of Krijger et al. (2001) reproduced per RADYN simulation by Fossum & Carlsson (2005b).⁷²

The MCs outlining network appear with brighter contrast at 1600 Å then at 1700 Å. Plane-parallel colleagues attribute this enhancement also to increased donor-ionization opacity and standard “network” and “plage” models therefore have less steep upper-photosphere temperature decay than their “quiet” companions for internetwork. However, the actual fluxtube brightness is photospheric hole-in-the-surface radiation, with deeper holes at shorter wavelength. This is also known for decades; I re-

⁷¹ *Carlsson-Stein internetwork shocks, four-panel diagrams, H $_{2V}$ grains.* Their well-known results were formally published in Carlsson & Stein (1995) and Carlsson & Stein (1997). Figs 8–12 (pdf 16) of Carlsson & Stein (1994) also introduced the informative Carlsson four-panel spectral-feature breakdown diagrams. For Ca II H one is shown in [SSX (pdf 156)], four in Figs. 4 (pdf 5)–7 (pdf 8) of Carlsson & Stein (1997), three for Na I D $_1$ and one for Ca II 8542 Å in Fig. 9 (pdf 8) of Leenaarts et al. (2010). [I recommend studying these – by understanding them you join a select club! In my courses they became examination material. An astute student noted that the second panel of [SSX (pdf 156)] exhibits the wrong assumption of CRD. Carlsson and Stein argued that their neglect of Ca II H PRD was compensated by not including Mg II h & k.] These breakdown diagrams clearly demonstrate the importance of NLT effects even though the spectral synthesis assumed SE. The observed bright Ca II H $_{2V}$ grains (note 33) which the simulation reproduced so admirably exist only because previous shocks define the opacity distribution along the line of sight. The bright H $_{2V}$ grain represents an upward traveling acoustic wave at too low height to show shock heating at its wavelength if the higher atmosphere were stationary; it gains its bright visibility from large higher-up downdraft after the earlier passage of a wave that shocked higher up. The downdraft pulls the line core redward and uncovers the grain.

⁷² *Acoustic and gravity wave heating.* Fossum & Carlsson (2005a) also laid the long-debated attribution of coronal heating to acoustic waves (e.g., Ulmschneider & Kalkofen 2003) to rest [unfortunately with what I call a “silly” publisher not furnishing a direct pdf opener on ADS. Page linking such publications (e.g., *Solar Physics* since Springer bought Kluwer) presents a multi-click hassle. If your remote library offers [Lean Library](#) its browser app may reduce this by silently using your remote-institute licenses, but I avoid page-linking silly publications altogether. If you publish in *Solar Physics* you should always add an arXiv upload [[ignore Springer’s stipulations against that – see my [Springer nasturtiums](#)]] so that ADS page-opens that instead]. Fortunately, they also wrote directly-opening Fossum & Carlsson (2006) on this topic. A previous directly-opening wave alternative for coronal heating is Whitaker (1963) who (with Parker’s blessing long before nanoflares) proposed gravity waves as main heater and introduced the “diagnostic” $k-\omega$ diagram (pdf 22) in solar physics following geophysics Hines (1960) (note 74). The $k-\omega$ diagrams in Fig. 3 (pdf 3) of Rutten & Krijger (2003) exhibit gravity-wave power and phase difference signatures. I doubt that gravity waves heat the corona (but see Straus et al. 2008); however, since gravity waves couple relatively easy into Alfvénic waves (Lighthill 1967) they may play a role in spicule-II heating of the quiet chromosphere (note 85).

cently put a review as caption in Fig. 73 (pdf 90) of Rutten (2020) and refer to that.⁷³ Actual MCs are close to RE throughout the photosphere without evidence of kinetic heating as expected for structures that inhibit convection (Fig. 7 (pdf 7) of Sheminova et al. 2005).

Thus, the standard-model “chromospheres” non-linearly represent under-the-chromosphere internetwork shocks (a domain I called “clapotisphere”⁷⁴ in Fig. 12 (pdf 7) of Rutten 1995), plus misinterpreted network surface holes. Nothing to do with the on-disk chromosphere in H α that carries the name originally given

⁷³ *Bright points shifts 1600–1700 Å.* Away from disk-center magnetic bright points in AIA 1600 Å images shift limbward from their 1700 Å counterparts. These shifts result from larger hole deepening and are shown, quantified, undone and explained in Figs. 70–73 (pdf 87) of Rutten (2020). My SDO alignment pipeline (note 87) has an option to unshift and subtract them to bring out flaring active-region fibrils (Vissers et al. 2015, Rutten 2016) that are brightened independently in 1600 Å images by emission in CIV lines.

⁷⁴ *Solar-p-mode history.* “Clapotis” on sea charts marks locations with “wild” waves from pattern interference. In regular wind-driven ocean waves material motion is mostly vertical; the same holds for the acoustic p -mode undulations of the solar surface. In HMI Dopplergram movies they appear everywhere as patches of apparently coherent 5-minute oscillation a bit larger than granules [a DKIST show-off granulation movie will need (k, ω) filtering]. The patches are the surface interference pattern of many solar p -modes and contribute “radial macroturbulence” to the wash-out of narrower lines than Mn I ones (note 34). In AIA 1700 Å movies the 3-min components pistoning Carlsson-Stein shocks appear as fast-moving erratically-distributed coming and going brightness wisps in internetwork regions. Both patterns appear random and chaotic. White & Cha (1973) studied apparent phase patterns of the 5-minute oscillation and concluded that they are random: “any description of the observed motion in terms of simple deterministic functions will be inadequate”. Chaos indeed [so much for future helioseismology]. I was the referee, found it convincing, and gave a Utrecht colloquium reviewing 5-minute oscillations but only the discovery part (showing 35-mm slides of the ingenious pre-IDL 10K×10K image processing plates of Leighton et al. 1962) and the confusion part (speculating about gravity waves turning into Alfvénic waves after Lighthill 1967) in this later display (pdf 1), yet without enlightenment because I was not aware of the Nobel-worthy modeling of Ulrich (1970). At the time the same held for F.-L. Deubner who was then contesting Frazier’s finding of substructure in the (k, ω) diagram (Deubner 1972; the underlinings are by R.W. Noyes whose annotated *Solar Physics* volumes got scanned by ADS). However, Deubner was asked to referee Wolff (1973) and so became aware of Wolff (1972) stating that the Sun is spherical and that Ulrich’s modes must be spherical harmonics. Deubner then recognized the paraboloid mode-location curves in Ulrich’s brilliant Fig. 2 (pdf 6) as the fish to catch and knew from Fig. 6 (pdf 17) of the authoritative [but French] (k, ω) description of Mein (1966) that long duration and large extent were the way to (k, ω) resolution and fast cadence and fine sampling to (k, ω) extent. He found the ridges, best in his hand-drawn note-in-progress diagram (pdf 4) in Deubner (1975) adding the detailed spherical-harmonic predictions of Ando & Osaki (1975). He showed it first at a conference in Nice, apologizing to Frazier (Deubner & McIntyre 1976) [McIntyre was not involved but wrote an ADS-misleading comment about earthquake modes]. It became the proceedings cover (Cayrel & Steinberg 1976) and made Deubner famous [scooping Ulrich and Rhodes who also had detected the ridges]. [Deubner and Mein both completed conservatory schooling; I made them play the Debussy cello sonata at the Zwaan retirement workshop (Rutten & Schrijver 1994).] More of the p -mode solar success story in my 5-minute lecture (pdf 1). Upshot: the photospheric p -mode pattern looks random but is a most beautiful harmonic chord (pdf 50) [I take my flute to public lectures “The Singing Sun” to demonstrate overtone harmonics] but the resulting chromospheric 3-min shock patterns are wildly clapotispheric, also vertically NLT interfering (note 71).

by Lockyer (1868)⁷⁵ for the colorful off-limb appearance of the Balmer lines and He I D₃.

Yet worse, actual H α canopies in quiet areas are mostly made by spicules-II (note 85) that reach heights around 7000 km (Pereira et al. 2014) far beyond any Avrett atmosphere. On the disk they are observed as outer H α -wing RBEs and RREs (note 85) – so much for ascribing outer-wing intensities to deep-photosphere sampling and so much for assigning brightness to heating since they heat to EUV visibility (Henriques et al. 2016) but are dark. Their subsequent cooling recombining return flows produce most of the dark H α line-core “mottles” around network (Rutten et al. 2019). Both types of ubiquitous dynamic H α structure are transparent in the ultraviolet continua used for constructing standard models which instead sample clapotisphere underneath, misnamed “chromosphere”.⁷⁶

⁷⁵ *Lockyer chromosphere, He I D₃, flash color.* I typed Lockyer (1868) into ADS, remain its main citer so far, and look forward to write “less refrangible” in publications [SSX (pdf 12–14)]. Lockyer’s total of about 50 ADS citations (but steepening reads) shows how citation ranking utterly fails for the first professor in astrophysics and the founding editor (during 50 years!) of *Nature*. I recommend his delightful “The Spectroscope and Its Applications”. In this report he discovered He I D₃ [as did “Indian observer” Janssen shortly before him]. It contributed its splendid yellow color [familiar to us from sodium street lamps] to the chromatic beauty of the emission lines he knew as prominence lines but saw everywhere just outside the limb with his new [but “incomplete” and delayed beyond Janssen] spectroscope [SSX (pdf 12)], concluding that “prominences are merely local aggregations of a gaseous medium which entirely envelopes the sun”. This was well before he saw himself the beautiful purple-pink of the flash chromosphere at eclipses, but he knew the visually-integrated color from prominences and chose the name to distinguish it from “the white light-giving photosphere” and the “cool absorbing atmosphere” – a reversing-layer Fraunhofer-line interpretation prior to Schuster-Schwarzschild modeling treated in the SSA 3.3 (pdf 31) practical, the opposite to Milne-Eddington modeling. The chromospheric flash color at eclipses during a few seconds after second and before third contact [longer near the edge of the totality strip as Houtgast did on purpose] sums his lines dominated by H α , plus white electron scattering (Sect. 7 on pdf page 8 of Jejić & Heinzel (2009) [another non-page-linkable at silly Springer without arXiv post]. The beautiful color represents H I, He I and freed H and He electrons: enjoy it yet more by appreciating it as the stuff the universe is made of.

⁷⁶ *Ha–Ha scattering.* Avrett stars yield H α disk-center profiles that correspond reasonably well to the observed disk-center atlas profile. Naïvely this may be seen as vindication of the model “chromosphere”. However, about the same profile is also produced in a NLTE RH computation of H α from an 1D RE atmosphere having no chromosphere whatsoever, only an RE photospheric temperature decline (Figs 7–8 (pdf 6–7) of Rutten & Uitenbroek 2012). The reason is that H α makes its own $\sqrt{\epsilon}$ scattering decline, more or less the same in H α optical depth scale irrespective of geometrical height scale and presence or absence of an upper-photosphere opacity gap. I call this “Ha–Ha” line formation. It similarly implies that actual H α from higher-located optically and effectively thick fibrils samples similar scattering declines. Furthermore, in the ALC7 atmosphere Ca II 8542 Å has nearly the same $\sqrt{\epsilon}$ decline with closely the same τ sampling (compare [SSX (pdf 91)] and [SSX (pdf 87)]). The solar-atlas profiles of H α and Ca II 8542 Å in Fig. 10 (pdf 10) of Rutten et al. (2011) differ substantially, but mostly from the difference in atomic mass affecting thermal broadening and H α ’s abnormal opacity gap, both known to ALC7 so that it reproduces both profiles reasonably well – but so does a Kurucz RE atmosphere without chromosphere and so do higher-up chromospheric fibrils (ha–ha). In quiet-Sun resolving observations the actual nonthermal motions yield different scenes in the cores of the lines (Fig. 3 (pdf 4) of Cauzzi et al. 2009) except for their time-averaged core widths which both sample temperature as does the time-averaged Ca II 8542 Å profile minimum (Fig. 4 (pdf 5) and Fig. 6 (pdf 7) of Cauzzi et al. 2009). In the wings

Yet worse, there even exist publications (not to be named) that used VALIIC Fig. 1 (pdf 3) to define “height differences” as the 400 km there between Ca II K₃ and the core of H α to identify and measure wave propagation and explain coronal heating. Maybe there exist plane-parallel stars in a parallel plain universe where this is a viable tactic (but do those have coronae?).

7. NLS+NLW+NLT: Oslo simulations

NLT is the current frontier in solar spectrum interpretation, not just in underlying MHD phenomena as the Carlsson-Stein shocks but also by not assuming SE in spectrum synthesis. Anything you see may not be so much how it appears now but rather what it was before. Outdoors example: airliner contrails on our sky signify that aircraft engines passed before. If you don’t know that aircraft exist you may have a problem to explain white clouds appearing in long lines.

The key publications I summarize here are the 1D(t) HD RADYN analysis of acoustic shocks by Carlsson & Stein (2002) and the 2D(t) MHD Stagger simulation of network and internetwork shocks by Leenaarts et al. (2007). The first showcases the physics, the second demonstrates the effects. Neither includes spectrum synthesis but the hydrogen rate analyses of the first and the hydrogen population results of the second suffice to designate these publications classics of solar spectrum formation.

1D HD RADYN simulation. Carlsson & Stein (2002) studied hydrogen partitioning in acoustic shocks as those of Carlsson & Stein (1997) in an exemplary analysis. Key results are summarized in [SSX (pdf 165)]. The main agent is Ly α . They found that detailed radiative balance is generally a close approximation for Ly α , in agreement with the discussion on VALIIC p. 662 (pdf 29): about as many photons go up as down, many more than collisions up or down. Most photons are created per pair **d** but then resonance scatter many times without coming far because their mean free path is small (1 cm in the center panel of [SSX (pdf 32)]) with scattering thermalization length about 10 km [SSX (pdf 90)] due to the immense $n_1 \approx N_H$ density while the probabilities of destruction **a** and Balmer detour **h** are small [SSX (pdf 90)]. This approximation was imposed as input by Leenaarts et al. (2007) to avoid quantifying large numbers that effectively cancel.

Fig. 3 (pdf 4) of Carlsson & Stein (2002), reproduced in the [SSX (pdf 165)] summary, illustrates this Ly α photon balancing as negligible net 1-2 rate. The fat transitions there (large net photon rate) are photo-ionization in the Balmer continuum and recombination with $\Delta n = 1$ steps⁷⁷ ending with fat H α . For given n_2 population (highly non-E in post-shock cooling) this loop obeys SE but it is far out of LTE because the impinging Balmer continuum originates in the deep photosphere, with radiation temperature about 5300 K [SSX (pdf 76)]. Where this value exceeds

both lines show spicules-II but H α more and longer (Fig. 2 (pdf 4) of Rouppe van der Voort et al. 2009, Fig. 1 (pdf 3) of Sekse et al. 2012). You can see all this very well with the last showex SST-data inspection of my alignment practical (note 87).

⁷⁷ *Rydberg HI lines.* The HI Rydberg ladder produces emission lines in the infrared by radiative-collisional recombination departure diffusion (Carlsson & Rutten 1992) similar to the Mg I 12-micron lines in note 56. At that wavelength the HI and Mg I lines are still apart but they creep together for higher levels and longer wavelengths. The Rydberg levels producing lines near 12 micron have larger population for Mg I than for HI (Fig. 1 (pdf 2)) of Rutten & Carlsson 1994 but this likely reverses at ALMA wavelengths through NLT HI-top population boosting (note 105).

the local temperature “photon pumping” enhances ionization. There are also contributing photon losses in heavily scattering H α [SSX (pdf 91)] which operates within the low-energy 3.6 eV hydrogen top as a “photon suction” alkali resonance line (Bruls et al. 1992; explanation with Fig. 2 (pdf 4) in Rutten & Carlsson 1994.)

The key hydrogen balance for NLT is the Ly α collision balance. The collisional up and down rates differ much in temperature sensitivity due to the Boltzmann ratio in their Einstein relation [SSX (pdf 166)] [RTSA p. 23 (pdf 43)] [RTSA Sect. 3.2.5 (pdf 70)]. The exponential C_{lu} sensitivity determines the settling time scale at which Ly α reaches Boltzmann equilibrium. A few cases are plotted in Fig. 6 (pdf 7) of Carlsson & Stein (2002), reproduced in [SSX (pdf 166)]. In hot shocks the frequent Ly α up- and down collisions make the balance reach Boltzmann equilibrium in seconds, but in subsequent post-shock cooling gas the settling time scale increases to multiple or many minutes. During this time the large n_2 overpopulation also governs large non-E overionization since the whole top of the hydrogen atom including the proton population is defined by this lower boundary condition. The Balmer-top SE loop just adds yet more overionization with respect to SB if the temperature drops below 5300 K.

2D MHD Stagger simulation. The next step in non-E simulation was Leenaarts et al. (2007), going from 1D to 2D and from HD to MHD. [SSX (pdf 167)] is a summary. The three panels at its top are cutouts showing three of the nine quantities in Fig. 1 (pdf 4) at a sample time step. They demonstrate that the simulation (evolved after starting from an LTE initializing simulation) portrays a quiet solar scene with two opposite-polarity MCs 8 Mm apart that resemble network fluxtubes, with internetwork in between showing a canopy-like dome with cool to very cool gas underneath and less steep upward density decay. For me the small 9-panel thumbnail underneath in [SSX (pdf 167)] is a clicker that opens [this movie version](#) running the whole simulation. Please download and play it. It vividly shows how shocks (thin blue filaments in temperature) travel up along the MCs and more erratic between them, the latter kicking up the apparent canopy. The first represent field-guided dynamic fibrils⁷⁸ as evident from their characteristic time-slice parabolas in the lefthand column of Fig. 3 (pdf 6). The internetwork shocks are acoustic Carlsson-Stein shocks.

The last panel of the three in [SSX (pdf 167)] and the nine in Fig. 1 (pdf 4) and its movie version show the NLTE departure coefficient b_2 of HI level $n = 2$, upper level of Ly α and lower level of H α . Its variations are enormous, reaching values up to 10^{12} in cooling post-shock blobs⁷⁹. This is not NLTE at the 0.1-1 dex level traditionally important in solar and stellar abundance

⁷⁸ *Dynamic fibrils* Field-guided shocked waves in active-region MCs (Hansteen et al. 2006, De Pontieu et al. 2007, earlier Suematsu et al. 1995). Their signature is repetitive parabolic extension and [non-ballistic] retraction along their length in timeslices. Many are visible as dark up-and-down dancing stalks in phased rows in this magnificent 5-s cadence SST/SOUP H α movie (courtesy L.H.M. Rouppe van der Voort). The rows map MC arrangements in network and plage; the phasing along rows is set by the interference-pattern undulations of the combined p -modes (note 74). Their tops may heat to high temperature and show up as bright grains in the Si IV lines in IRIS 1400 Å slitjaw images (Skogsrud et al. 2016). Short ones are observed in sunspots (Rouppe van der Voort & de la Cruz Rodríguez 2013).

⁷⁹ This panel also shows high-up green arches. I think that these are artifacts stemming from the input tractability assumption that Ly α obeys detailed radiative balance everywhere [it does lower down].

studies – this is 12 dex! The next to last panel of Fig. 1 (pdf 4) and its movie version shows the departure for the H I continuum level ($n = 6$ in the atom model) and illustrates that Balmer continuum pumping adds up to another 3 dex for the coolest clouds.

Fig. 2 (pdf 5) of Leenaarts et al. (2007) is also best studied in its movie version. Its panels show behavior of the y -axis quantity along the dotted vertical lines in the fourth panel of Fig. 1 (pdf 4), at left sampling the lefthand MC and at right internetwork. In the lower three rows the thick curves are the simulation results, the thin curves the values obtained by assuming LTE instead so that the curve separations correspond to the departure coefficients in Fig. 1 and its movie version. Playing this movie shows shocks running up with time in the temperature curves in the lefthand top panel. The actual shocks in the Fig. 1 movie tend to go slanted in the internetwork, so that the righthand column samplings are not along-the-shock path histories⁸⁰ but represent different shocks at different times. The movie strikingly demonstrates that the ionization fraction, proton density and n_2 population density in the lower rows reach LTE values in shocks but thereafter do not drop steeply along with the temperature. Instead they hang roughly at the value they got in the shock. There should be eventual settling to the LTE value, but long before that the next shock arrives: shocks repeat faster than the settling time scale. In the lefthand column sampling dynamic fibril shocks better along their near-vertical paths, the persistently-high n_2 population results in the dark appearance of dynamic fibrils in the downstroke phase of their timeslice parabolas⁸¹. If SE LTE held they would fade fast with the lowering temperature.

The second row shows that hydrogen generally does not ionize fully in the shocks but only a few percent. However, this already means two orders of magnitude increase of the electron density which in neutral-hydrogen gas sits at the 10^{-4} abundance fraction of the electron donor metals (VALIII 47 (pdf 67) [SSX (pdf 72)]). This increase in collision frequency appears sufficient to obtain LTE Boltzmann equilibrium in Ly α within the shocks, giving LTE Balmer extinction. Another condition for this equilibrating is that a feature should be thick enough to contain Ly α , optically thicker than the thermalization length from its surface [SSX (pdf 90)]. At percent-level ionization hydrogen retains sufficient n_1 opacity to keep these shocks effectively thick in Ly α .

⁸⁰ *Internetwork shocks in Ca II H and H α .* When M. Carlsson hunted in the data of Lites et al. (1993) he found only few pixels with nice multi-cycle spectrum-versus-time behavior as in RADYN output and selected the best for Fig. 18 (pdf 13) of Carlsson & Stein (1997). Others as the two less matching samplings in their Fig. 17 (pdf 20) may have been too slanted to produce vertical-column NLT signature or had too much sideways wave interference. Their four samplings are marked in the observed time slices in Fig. 2 (pdf 4) of Rutten et al. (2008) where the rightmost panel shows slanted propagation tracks crossing the latter two (149 and 30). The very quiet-target SST movie linked in note 70 and here again shows fast-varying threads constituting H α “mushroom” shells following on and around Ca II H $_{2V}$ grains, indeed not radial along the line of sight: internetwork shocks are 3D(t) rather than 1D or 2D phenomena even if the p -mode wave pistoning is primarily radial. Per-pixel Fourier analysis to establish vertical phase relations is invalid for the resulting shocks and their mushroom aftermaths. The cadence of the movie is 7 seconds but faster is clearly desirable [I hope that DKIST reaches 1 s cadence in H α sampling]. The showex SST displays in my alignment practical show H α mushroom threads very well in the upper-left quiet corner of the SST field but at slower cadence.

⁸¹ Seen well in the SST/SOUP H α movie of note 78.

3D MHD Bifrost simulations. Since these classic simulations the Oslo simulators went to 3D(t) MHD Bifrost⁸² of Gudiksen et al. (2011) [SSX (pdf 159)]. The Bifrost stars are far more solar-like than the Avrett stars by being 3D(t) with dynamism and magnetism. Unlike the Avrett stars they contain realistic granulation, acoustic waves and shocks, MCs arranged in network patterns, dynamic fibrils, bipolar-network-connecting chromospheric fibrils, and Ellerman bombs (EB). However, they still lack in spicules-II and attendant fibrils around network as major quiet-chromosphere ingredients, and their cube sizes are yet too small for supergranulation, active regions, and larger-scale coronal fine structure. Bifrost spectral synthesis has mostly concentrated on the IRIS diagnostics. Obviously it beats Avrett-star spectral synthesis in NLS, although most analyses rely for tractability on columnar modeling with the RH 1.5D program of Pereira & Uitenbroek (2015). The Avrett stars handle NLW better with respect to ultraviolet ionization and the problematic ultraviolet line haze (Fig. 10 (pdf 18) of Rutten 2019). Various Bifrost runs included NLT for hydrogen (as in the classics above), but not in subsequent spectral synthesis⁸³.

8. NLS – NLW – NLT chromosphere spectrum

SE is usually a sound assumption for thick spectral modeling of photospheric structures (SE NLTE) and for thin spectral modeling of coronal structures (SE CE). Chromospheric structures in between are the hardest to model because NLT reigns next to NLS and NLW in making them cycle through thick and thin.⁸⁴ For a review see Carlsson et al. (2019).

⁸² *Bifrost program.* This MHD simulation code of Gudiksen et al. (2011) is named after old-Norse Bifröst in the Icelandic Edda: *burning rainbow bridge between Earth and the realm of gods* [slightly more inviting than Pandora]. Reference lists (until 2018 at the time of writing) are given in [SSX (pdf 160–163)]. Many studies employ the public snapshot of Carlsson et al. (2016). ADS abstract search “Bifrost” and “solar” gives publication count and Hirsch $N = 77$, $h = 17$, solid enough for a solid permanent position. “MURaM” and “solar” $N = 74$, $h = 19$ idem for the MHD simulation program of Vögler et al. (2005). Maybe you should simulate – so it goes.

⁸³ But see Golding et al. (2017) for an NLT analysis of EUV helium lines.

⁸⁴ *Transition region versus heated chromosphere.* I skip the so-called “transition region” because I don’t think such exists as a separable domain in the solar atmosphere. The shocks in the Fig 1 movie of Leenaarts et al. (2007) lift the corona (let’s define that as fully ionized hydrogen) above them tremendously up and down, doing so effortlessly with a steep space-time-varying temperature jump as instantaneous highly-warped envelope, not as the global shell of standard models. The simulated corona there reaches lower in the MCs, as it does in moss in denser plage regions (note 98). Furthermore, in closed-field regions the quiet-Sun chromosphere observed in the “transition” He II 304 Å line with AIA resembles the fibrillar H α chromosphere so well that one may co-align reversed-intensity quiet-Sun H α and 304 Å images by pattern correlation, as shown and discussed in Appendix B (pdf 11) of Rutten (2020). This pattern similarity extends even to AIA 131 Å images. The 304 and 131 Å emitting gas around quiet network is not a thin transitional envelope around H α fibrils but represents hot ionization phases, i.e., hot tips of spicules-II and their still hot aftermaths whereas H α fibrils show cooling recombining return gas NLT-darkest near the spicule-II ejecting network. Both outline canopies with similar surface patterns because each samples the quiet chromosphere around network in successive manifestations. *The chromosphere ain’t stacked in layers but is NLT unstuck in time* [Billy Pilgrim syndrome].

Quiet chromosphere. In the optical the quiet chromosphere is seen only in Balmer lines, Ca II lines and He I lines. The Lockyer definition implies it is made up by the fibrils seen around network in the H α core and with lesser extent in Ca II 8542 Å. The scene in Ca II H & K is more complex due to larger Doppler sensitivity enhanced by PRD, and the Ca II lines also do not skip the clapotisphere in their inner wings. H α fibrils spreading from network are largely made by spicules-II.⁸⁵

In AIA UV images the quiet chromosphere is transparent. They sample clapotisphere underneath and yet deeper in MC holes in the photospheric surface (Fig. 75 (pdf 90) of Rutten 2020). Active phenomena brighten 1600 Å images with chromospheric C IV contributions (EBs and flaring active-region fibrils (FAF), [Visser et al. 2015](#), [Rutten 2016](#)).

In AIA 304 Å images quiet areas show two major chromosphere constituents: ubiquitous extended heating patches and sparser brighter feet of coronal bright points (CBP). For a quick overview inspect the 10 “triple” image sets in [Figs. 17 \(pdf 34\) – 46 \(pdf 63\)](#) of [Rutten \(2020\)](#). The first of each triple is a large-field 193 Å image showing coronal activity, coronal holes, and CBPs. The second is a clipped “fire detector” multiplication of 304 Å and 131 Å images in which grey patches show heated quiet chromosphere and cyan-colored pixels mark CBP feet. The third is the corresponding HMI magnetogram showing what underlies and probably causes CBPs. The 10 triples sample low and high activity and low and high latitude and permit inspecting multiple coronal holes.⁸⁶

⁸⁵ *Spicules-II*. In my [not too humble] opinion these are the main agents causing the fibrillar H α and heated He II 304 Å quiet-Sun chromospheres (while not heating the corona), and are the main agents in quiet-chromosphere spectrum formation. I use the name generically for off-limb and on-disk manifestations. I noted them as “straws” near the limb in [DOT Ca II H movies \(Fig. 1 \(pdf 2\)\)](#) of [Rutten 2006](#) but they were described earlier as outer-wing H α “jets” by [Suematsu et al. \(1995\)](#) and in later Big Bear reports. They were detected and measured using Hinode off-limb Ca II H sequences and attributed to Alfvénic waves and named “spicules type-II” by [de Pontieu et al. \(2007\)](#) and [De Pontieu et al. \(2007\)](#) [no bibtex a, b because the first spells Dutch]. Spicules-I reach less high above the limb, crowd into the “spicule forest” in H α limb images, and were attributed to active-region dynamic fibrils ([note 78](#)) by [Pereira et al. \(2012\)](#). Spicules-II are ubiquitously ejected from quiet-Sun network including monopolar network and also in coronal holes. On the disk these ejections became known as “rapid blue-wing excursion” (RBE) ([Roupe van der Voort et al. 2009](#)) and “rapid red-wing excursion” (RRE) ([Sekse et al. 2013](#)), first in the wings of Ca II 8542 Å and then in the outer wings of H α , with heating up to EUV visibility ([Henriques et al. 2016](#)). Their aftermaths of cooling recombining return flows cause dark H α -core fibrils around network known as “mottles” in older days, minutes later with their H α opacities probably much enhanced by NLT cool-down retardance as in the post-shock clouds of [Leenaarts et al. \(2007\)](#). Evidence are the darkest-darkest time-delay correlations in [Rutten et al. \(2019\)](#) [my [alignment practical \(note 87\)](#) enables you to inspect such time-delay correlations yourself for coronal-hole SST spicules-II]. The spicule-II driver mechanism is not known ([Pereira et al. 2012](#)) but because spicules-II exhibit torsion modes near and at the limb ([De Pontieu et al. 2012](#), [Rutten 2013](#)) vorticity in granular convection affecting embedded network fluxtubes seems a candidate, perhaps with fly-by reconnection as in [Meyer et al. \(2012\)](#) kicking up Alfvénic waves and perhaps with coupling to gravity waves ([note 72](#)).

⁸⁶ *SDO quiet-chromosphere images (pdf 34 ff)*. I recommend page-blinking the three members of each set. I find it uncanny how well the detector images separate localized chromospheric heating (ubiquitous grey patches around any network outside coronal holes) from sparser localized coronal heating (cyan CBP feet in denser bipolar network also in coronal holes). This separation implies that atmospheric heating is

The heated chromosphere patches in the detector images appear everywhere around network but fewer in coronal holes. Their surface patterns are cospatial with the fibrillar H α canopies around network ([Appendix B \(pdf 11\)](#) of [Rutten 2020](#)) and serve in my SDO alignment pipeline⁸⁷ to cross-align AIA 304 Å images directly to HMI magnetograms. I attribute this component to the heating phase of spicules-II ejected from network. These also occur in coronal holes; I suspect that the lack of corresponding 304 Å heating patches there is from lack of EUV irradiation from above that elsewhere enhances He I ionization. AIA 193 Å images do not show these quiet-chromosphere heating patches but outside coronal holes they do show wide-spread diffuse brightness providing such irradiation as a diffuse blanket.

CBPs are sparser but not rare in quiet areas. They are best seen in 193 Å images as small ensembles of EUV-bright loops located at and connecting bipolar network (review by [Madjarska 2019](#)). They appear as “mini” active regions, are likely due to ongoing flux emergence and flux assembly into network, and are probably heated by reconnection near their loop tops with subsequent heating of their chromospheric feet⁸⁸ ([Madjarska et al. 2021](#)), likely by particle beams ([Frogner et al. 2020](#), cf. [Rutten 2020](#)). These features can live fairly long, the smallest⁸⁹ Rut-

not traditionally “via the chromosphere to the corona” (with a much larger energy need for the denser chromosphere) but that it is done by unrelated mechanisms for quiet chromosphere (spicules-II) and quiet corona (CBPs).

⁸⁷ *SDO alignment programs* A large collection of IDL programs to request and download SDO sequences for any field, location, time, duration, typically for co-alignment with image sequences from another smaller-field higher-resolution telescope such as the SST. The AIA sequences get cross-aligned with sub-pixel precision to HMI by cross-correlation of large parallel cutouts around solar center and are then co-aligned with 0.1 arcsec precision to the other telescope (or vice versa). See [program manual](#) and [alignment practical](#). Alignment results are shown in [Fig. 75 \(pdf 92\)](#) of [Rutten \(2020\)](#). For small fields this pipeline is fast by not handling full-disk images but only JSOC `im_patch` cutouts. All programs use IDL `assoc` to avoid memory loads. There is a versatile sequence browser `showex.pro` which can play, blink, manipulate, cross-correlate many movies in parallel with zoom-in magnification. The [alignment practical](#) contains examples browsing the SDO-aligned quiet-Sun SST data of [note 70](#). The disk-center coronal hole sampled there also sports a few “SolO campfires” ([note 89](#)).

⁸⁸ *CBP foot visibility*. CBP feet are bright in AIA 304 Å and its “fire detector” ([pdf 86](#)) product with 131 Å but sharper in IRIS 1400 Å slit-jaw images because Si IV has similar temperature-defined presence as He II but 10³ lower abundance (compare the complex CBP in the 1400 Å and 304 Å columns of [Fig. 2 \(pdf 3\)](#) of [Rutten & Roupe van der Voort 2017](#)). The SDO cutouts for a dozen CBPs in [Fig. 48 ff \(pdf 65 ff\)](#) of [Rutten \(2020\)](#) suggest there is additional 304 Å brightness around bright CBP feet due to EUV irradiance from above.

⁸⁹ *“SolO campfires”*. Press-release hullabalooed as new coronal heating agent and so triggering [Rutten \(2020\)](#), but already reported as smallest CBPs by [Falconer et al. \(1998\)](#) and [non-hullabalooed] present throughout the AIA database. They are the smallest cyan features in the detector images in the ten triple blinkers in [Figs. 17 ff \(pdf 34\)](#). The many CBPs in these snapshots suggest that at any time the smaller CBPs are somewhat more numerous per size class than larger CBPs, but the latter live much longer (fifteen evolutionary cutouts in [Figs. 48 ff \(pdf 65\)](#)). The cyan detector CBP feet are at chromospheric heights, come from above as in [Fig. 12 \(pdf 13\)](#) of [Frogner et al. \(2020\)](#), and mark [not cause] higher-up CBP loop reconnection caused by bipolar network as evident in blinking with the triple magnetograms. It is a mistake to sum observed CBP brightnesses as contribution to coronal heating since this energy is radiated away ([note 31](#)). The actual coronal heating patterns in the AIA 193 Å triple images suggest negligible heating from the smallest [campfire] CBPs and most from the largest.

ten (2020). the shortest, but AIA 193 Å movies show frequent change suggesting continuous renewal. The representative AIA 193 Å images shown as triple members in Figs. 17 (pdf 34)–46 (pdf 63) of Rutten (2020) suggest that CBPs are the main agent in quiet-Sun coronal heating and cause the diffuse AIA 193 Å brightness spread widely around them, together and with contributions from prior CBPs. Such diffuse brightness is absent in coronal holes where heating does not spread to surrounding surface areas along closed loops but instead follows open-field up and out, likely as coronal plumes (Wang et al. 1997).

The appearance of the chromosphere in optical He I lines⁹⁰ remains an outstanding problem. Lockyer proposed element “helios” for He I D₃ which became helium and remains the only extra-terrestrially discovered element.⁹¹ I am not aware of a sound explanation why his He I D₃ is so extraordinary strong off-limb, equal to H α in his engraved Fig 42 (pdf 94) and ranking between H γ and H β in brightness and off-limb extent in pages 94–95 of Table 3A (pdf 94) of Dunn et al. (1968), much brighter and higher than its Na I D neighbors whereas it is nearly invisible on the disk and hence not even mentioned on page 258 (pdf 292) of the line table of Moore et al. (1966) from the Utrecht Atlas of Minnaert et al. (1940) in which the Na I D lines are the darkest in the optical and the Balmer lines are prominent wide dips (Fig. 10 (pdf 18) of Rutten 2019). How can the Balmer lines in the top of the hydrogen atom and the He I lines in the top of the helium atom differ so enormously between transverse and top-down viewing?⁹² Apparently the He I top shares in the spicule-II emissivity phase but much less in the subsequent recombination opacity phase. Maybe He I outside coronal holes remains considerably photoionized by blanket-like EUV irradiation from wide-around above. Spicule-II RBEs and RREs occur ubiquitously also in coronal holes but produce less 304 Å and 131 Å heated chromosphere there⁹³. H α does not map coronal holes but the He I and He II 304 Å lines do.

To reproduce such dynamic nature numerically, even for just “quiet” chromosphere, poses enormous challenges because the MHD simulations must produce spicules-II as copiously as actual solar network does and must then be combined with 3D(t) NLS–NLW–NLT (“non-E”) spectral synthesis including PRD at least for Ly α to recover the observed H α chromosphere, and in addition must produce small-scale bipolar activity causing and governing CBPs as observed.

ALMA has the potentiality to sample and measure the chromosphere sharper and faster than DKIST. Plane-parallel modeling and various simulations have suggested that ALMA samples the claptosphere dominated by acoustic waves on their way to

become shocks but these efforts erred in assuming SE. Because Ly α -controlled NLT opacity enhancement of the HI n_2 population also gives enhanced hydrogen ionization I have instead predicted that NLT-opaque H α canopies are similarly NLT-opaque in the HI free-free continua sampled by ALMA (Rutten 2017b with a tutorial in Rutten 2017a).⁹⁴ This means that, while ALMA is a thermometer thanks to free-free source function LTE, due to NLT extinction NLTE it more likely samples H α canopy fibrils than internetwork shocks underneath – a blessing because we understand internetwork shocks for decades but do not understand the chromosphere. The good correlation between ALMA intensity and H α width (both gauges of temperature, see Cauzzi et al. 2009) in Fig. 4 (pdf 6) of Molnar et al. (2019) confirms this view.⁹⁵

⁹⁴ *Background: RBE–RRE–fibril ionization-recombination.* RBEs and RREs reach higher degrees of hydrogen ionization than the shocks in the Fig 2 movie of Leenaarts et al. (2007). They extend further in H α than in Ca II 8542 Å (lower-left panel of Fig. 1 (pdf 3) of Sekse et al. 2012) because Ca II ionizes before HI and is much less abundant. Where their tips reach AIA EUV visibility (Henriques et al. 2016) hydrogen is nearly or fully ionized. The resulting recombining fibrils are more numerous and also much longer in H α than in Ca II 8542 Å (Fig. 3 (pdf 4) of Cauzzi et al. 2009). The time-averaged core-widths correlation in the bottom row of Fig. 6 (pdf 7) of Cauzzi et al. (2009) suggests that both lines sample recombining-fibril temperatures but with much larger fibril opacity in H α , as in the return contrast in Fig. 5 (pdf 6) of Rutten & Rouppe van der Voort (2017). You can check these findings yourself with high-quality SST quiet-Sun data with my alignment practical (note 70). Its last showex command browses SST H α and Ca II 8542 Å image sequences sampling many wavelengths and also adding the three core measures of Cauzzi et al. (2009) for both lines. It shows scatter diagrams between the selected samplings and has a button for sequence time-averaging. For example, the well-correlated width-width blink shows how much further the H α spicules-II reach, and time-delay blinking H α -0.6 Å against H α +0.2 Å confirms Rutten et al. (2019) with yet better data showing striking darkest-darkest correlation between RBEs and subsequent redshifted core fibrils around 5-min delay, and also that these reach close to the spicule-II firing network [because in the cooling return H α gains largest NLT overopacity there keeping it \sqrt{e} dark]. The minima and shift blinks show that in Ca II 8542 Å these return fibrils get visible only very close to network where also Ca II recombines from Ca III. Thus, large spicule-II H ionization is followed by cooling return recombination producing core fibrils that are much more prominent in the H α core. The few-percent ionization in the shocks in the Fig 2 movie of Leenaarts et al. (2007) with its two-orders of magnitude electron density increase already suffices to reach near-SB proton densities (3rd movie row). Hence large electron densities and SB partitioning must also occur in spicules-II, warranting straightforward SB extinction comparisons as in Fig. 7 (pdf 7) of Rutten & Rouppe van der Voort (2017) for the hot spicule-II phases while recognizing that these high extinction values persist NLT-wise afterwards in the recombining return fibrils constituting opaque canopies while instantaneous SB values drop Boltzmann-steep with their temperature. Similar SB curves imply the same for the mm wavelengths of ALMA in Fig. 1 (pdf 4) of Rutten (2017b) where the HI free-free extinction curves rise as steeply as for H α in the Boltzmann increase and then saturate at increasingly much higher values for longer wavelengths due to the Rayleigh-Jeans λ^2 in free-free extinction $\alpha_{\lambda}^{\text{ff}} \sim N_e N_p T^{-3/2} \lambda^2$ [RTSA Eq. 2.79 (pdf 47)]. Summary: in heating gas the hydrogen-top populations and extinction slide fast up along the SB curves to high values at large hydrogen ionization, but in subsequent cooling they hang multiple minutes near these high values before finally dropping back to the SB value for the actual temperature [’tis all NLT for fibrils].

⁹⁵ *ALMA–GONG–SDO alignment.* Another confirmation that ALMA sees quiet-Sun chromospheric canopies is that quiet-Sun ALMA images can be co-aligned with H α images through cross-correlation. These are near-always available from GONG but with large quality variations with time and between stations, fortunately with ALMA’s longitude sam-

⁹⁰ *Optical He I lines.* These are He I 10830 Å, weaker He I D₃ at 5876 Å, He I 6678 Å “occasionally making its appearance” (Lockyer 1868). He I 10830 Å reaches largest extinction because its lower level is metastable and collects population. Its observed depth is the best coronal hole mapper in the optical. I wonder whether low-density high-temperature dielectronic recombination as in Fig. 1 (pdf 4) of Burgess (1964) contributes.

⁹¹ *Coronium, nebulum, Zanstra.* Coronium [SSX (pdf 8)] and nebulum [SSX (pdf 142–147)] went away. The ingenious Zanstra mechanism for detour photon conversion in planetary nebulae [SSX (pdf 144)] [IART Sect. 8.3.3.1 (pdf 137)] may be at work for hot and dense solar features illuminating cooler surroundings (EBs, flares).

⁹² The 400+-page book by Athay & Thomas (1961) [wrong order at ADS] addressed this question without clear answer. It was grandly titled “Physics of the solar chromosphere” earning a scathing review from De Jager [SSX (pdf 15–17)] for not mentioning magnetism nor dynamism.

⁹³ High-resolution example: blink the AIA fire detector and SST H α core-width images in my alignment practical (note 87).

There have been and there are efforts (e.g., Eklund et al. 2021) to synthesize ALMA signatures of under-canopy inter-network shocks from the public Bifrost simulation of Carlsson et al. (2016) but since this simulation does not show spicules-II nor attendant $H\alpha$ canopy fibrils emanating outward from its network such efforts apply probably only to very quiet areas as the ones offered in note 70 and described in note 80. AIA 304 Å images can assist in locating such canopy-free locations. They are rare. Elsewhere my hope is that ALMA will help solve the long-standing problem of chromospheric heating in quiet areas. Hopefully soon so that we can turn to activity in its current up-swing to maximum.

Active chromosphere. For chromospheric activity phenomena I refer to Jongchul Chae's contribution in this school because I have not worked on these (except EBs⁹⁶). Hence no discussion of spot chromospheres, flares, filaments, etc. here. I restrict this section to two active region scenes in different diagnostics.

The first scene is the DST/IBIS–SDO multi-wavelength image mosaic of Cauzzi & Reardon (2012) and Reardon & Cauzzi (2012a, 2012b) showing AR 1092 near disk center on 2010-08-03 in the early days of SDO. I received these concurrent co-aligned images from K.P. Reardon and combined them into this

plung the usually better ones (Big Bear and Cerro Tololo). Since they are full-disk images good ones likely contain a suited large quiet closed-field area somewhere for precise co-alignment (reversedly as in Fig. 11 (pdf 28) of Rutten 2020 and discussed in Appendix B (pdf 11) there) to simultaneous AIA 304 Å images and then may serve (also reversedly) as ALMA-to-SDO intermediary for wherever ALMA pointed. I succeeded in this for quiet-Sun ALMA data with a good GONG sequence and indeed found pattern correlation between the ALMA and AIA chromospheres.

⁹⁶ *Ellerman bombs.* I participated in Watanabe et al. (2011), Rutten et al. (2013), Vissers et al. (2013), Rutten et al. (2015), Vissers et al. (2015), Rutten (2016), Young et al. (2018), Vissers et al. (2019) [I think that I helped boost interest in Ellerman (1917): after half a century of ignorance it shot up in ADS citations reaching 100 in its centennial year. Moral: if your nice discovery remains unnoticed just relax waiting for ADS to revive it. However, this revival got my laptop confiscated by border police spotting the B word]. EBs are photospheric but of interest here because the spectral signature of these strong-field reconnection events is complex and instructive. They appear very bright only in the $H\alpha$ wings because their $H\alpha$ line cores remain shielded by overlying dark active-region fibrils (Fig. 3 (pdf 4) of Rutten et al. 2013). They are therefore similarly shielded and invisible for ALMA (prediction 9 (pdf 9) of Rutten 2017b confirmed by da Silva Santos et al. 2020). They are not visible in the Na I D and Mg I b lines (Ellerman 1917, Rutten et al. 2015) because they are hot enough to fully ionize neutral metals and they appear bright in UV continua (AIA 1700 Å and 1600 Å) from Balmer continuum brightening with neutral-atom bound-free opacity ionized away. The cartoon in Fig. 2 (pdf 5) of Rutten (2016) added one to the last panel of Fig. 1 of the simulation of Leenaarts et al. (2007). Because they are hotter and denser than the shocks in which $Ly\alpha$ already reaches collisional equilibrium their $H\alpha$ extinction obeys SB partitioning, permitting the straightforward SB opacity comparisons in Fig. 5 (pdf 9) of Rutten (2016). The actual EB $H\alpha$ profile under the canopy is probably similar to Mg II k ($H\alpha$ reaches similar extinction and emissivity at high temperature) with a very high peak and a small central dip as in Fig. 4 (pdf 7) of Vissers et al. (2015). It is a mistake to sum observed EB brightnesses as contribution to coronal heating since this energy is radiated away (note 31). Presently the interest has moved to non-active quiet-Sun QSEBs (“quiet-Sun Ellerman-like brightening”) marking ubiquitous but hard-to-detect small-scale photospheric reconnection (Roupe van der Voort et al. 2016, Danilovic 2017, Joshi et al. 2020).

pdf blinker.⁹⁷ The IBIS selection samples Ca II 8542 Å, $H\alpha$ (also $H\alpha$ core width and core-minimum Dopplershift as defined in Cauzzi et al. 2009), and the equivalent width of He I D₃. The SDO selection adds comparable HMI and AIA diagnostics. This IBIS blinker represents an active-region counterpart to the final showex inspection of the quiet-Sun SST and SDO sequences in my alignment practical. These two data displays are utterly different. The SST set is a time sequence of a small very quiet coronal-hole field with only some network. The IBIS set is only a single snapshot, not permitting time-delay cause-and-effect sequence inspection, but shows a larger field containing dense unipolar plage, mossy plage⁹⁸, a large regular spot, and even a small flare originating in the spot which behaves as a CBP with loop brightening and feet heating. Blinking these images represents a vivid course in active-region phenomenology and also displays aspects discussed above.⁹⁹

⁹⁷ In a sequence suited to pairwise blinking. Most pdf viewers furnish blinking by flipping pages in-place with the cursor arrow or page up-down keys. Full-page or fit-to-page viewing may help. Multiple-page flipping may be possible with a back key. Myself I use my showex blinker (from the command line as in my SDO IDL manual) because it auto-blinks between selectable pairs at selectable speed and offers zoom-in magnification with scatter-diagram correlation and more.

⁹⁸ *Moss.* “Spongy” active-region plage showing many short loops and bright footpoints interspersed with darker patches at small scales in 171 Å and other EUV lines (e.g., Berger et al. 1999b, Berger et al. 1999a, de Pontieu et al. 1999, Martens et al. 2000, De Pontieu et al. 2003). Polito et al. (2020) differentiate moss and outflow regions in active-region plage where the latter likely contribute to the slow wind and the FIP effect (note 101).

⁹⁹ *IBIS–SDO active-region blinker.* Most of these images have enhanced grey scales by using the square root or the square of the measured intensity plus clipping. All have a small area near center magnified four times in the upper-right corner for more detailed blinking. Inventory (please blink yourself):

HMI Stokes I–V (p1–p2): Stokes I shows only granules, pores and the spot, no network or plage in Stokes V [higher resolution would show abnormal granulation in plage]. Plage brightens in such continuum sampling only near the limb, from MC transparency in slanted viewing (righthand cartoon in Fig. 73 (pdf 90) of Rutten 2020). There is opposite polarity field in the sunspot moat where the flare occurs (blink p2–p5).

HMI Stokes V–AIA 1700 Å (p2–p3): in 1700 Å conspicuous MC brightening not from higher-up heating but from magnetic hole brightening (lefthand cartoon and caption of Fig. 73 (pdf 90) of Rutten 2020). Having the same “height of formation” gives co-spatiality in blinking this disk-center images but towards the limb 1700 Å bright points shift relatively limbward, 1600 Å more (note 73). A few bright 1700 Å points in internetwork mark isolated MCs that are barely detected by HMI. They may be products of ephemeral regions on their way to network as the “persistent flasher” of Brandt et al. (1994). Elsewhere the grey fine structure in 1700 Å internetwork areas represents clapotispheric shocks (note 71).

AIA 1700 Å–Ca II 8542 Å wing I (p3–p4): in the Ca II 8542 Å wing MC brightening in plage and network is hole brightening from less collisional damping and additional downdrafts, but the inset suggests much shielding within plage. Enhanced bright points in the sunspot moat are likely not EBs since they lack corresponding excess 1700 Å brightness (Vissers et al. 2019) and may mark MC downdrafts common in moats (Beck et al. 2007). Internetwork areas show predominant reversed granulation (inset) and also sporadic shock brightening in grains (Rutten et al. 2011). Slender dark fibrils extending from plage and network represent the plage counterpart of network RBEs combining blueshift and line broadening in this blue-wing sampling as in Roupe van der Voort et al. (2009).

Ca II 8542 Å wing I–core I (p4–p5): dramatic difference. The core shows the chromosphere with bright-grained network and plage hearts

One striking difference between quiet and active scenes is that quiet closed-field areas permit $H\alpha$ and He II 304 Å co-alignment by reversing $H\alpha$ intensity (note 84, note 95, Appendix B (pdf 11) of Rutten 2020) whereas active areas permit co-alignment using normal $H\alpha$ intensity (blinker p6–p10). I attribute this difference to different ratios between roundabout (“around”) chromosphere heating that dominates in quiet closed-field areas and upward chromosphere heating that dominates in the hearts of active network and plage from more numerous and

signifying onset of heating. Magnified blinking shows that many of these dense bright grains are roughly cospatial with wing MCs, suggesting upward heating, mostly in unipolar plage (p2). Blinking to 171 Å (p11) shows a few areas appearing as EUV moss (note 98) over bipolar plage (one patch is above the cutout square but HMI does not show all opposite-polarity field). Dark fibrils extend far over internetwork but do not cover all of that, some internetwork still shows up in the quietest areas with shock brightening in grains of which some are also visible in the wing image.

Ca II 8542 Å core I – $H\alpha$ core I (p5–p6): similar scenes but all fibrils are much fatter and longer in $H\alpha$ which I attribute to large non-E opacity (note 94). All internetwork is covered by fibrils in $H\alpha$. The bright plage grains often correspond well between the two (inset). Some may be heated tips of dynamic fibrils observed down-the-throat. There are long slender dark active-region filaments above polarity inversion lines (blink either against p2). The spot flare shows its concurrent loop and feet brightening similarly in both line cores.

$H\alpha$ core I – minimum shift (p6–p7): the second is the shift of the $H\alpha$ profile minimum per pixel following Cauzzi et al. (2009), with blueshift dark. The hearts of the plage areas have small-scale grainy appearance with sizable patches of large blueshift. The fibrils extending away show lower-amplitude fibril-to-fibril modulation, a signature of their intermittent repetitiveness in extending out and shrinking back [called “breathing” by a colleague]. Blinking the inset shows short dark blueshifted heating onsets; the longer grey fibrils are return flows. The latter show similar but finer structure in Ca II 8542 Å I (blink p5–p7); showex zoom-in shows two-branch scatter diagrams there because Doppler-shifting the narrow Ca II 8542 Å core brightens its intensity for both blue- and red-shift. In $H\alpha$ the umbra shows flashes on their way to running penumbral waves. Only the brightest are visible in Ca II 8542 Å but they are well-known from Ca II H & K as in Figs. 2–4 (pdf 4) of Rouppe van der Voort et al. (2003). The spot flare shows a very bright core-shift feature in the loop and also a very dark shift companion feature further out, at image edge. Diametrically opposite on the other side of the spot there is a conspicuous bright-dark feature pair that also seems connected.

$H\alpha$ core width (p8): width of the $H\alpha$ core per pixel following Cauzzi et al. (2009). The bottom panels of their Fig. 6 (pdf 7) with quantification in their Fig. 9 (pdf 9) showed that this is a proxy for temperature thanks to the small H atom mass. It is perhaps the most telltale scene in this blinker. The plage hearts are again grainy and mostly hot. The bushes extending away from there are shorter than the fibrils in core intensity (p6) because these are RBE-type heating onsets. Network RBEs reach much further out while heating and accelerating, but their profile signature moves out from the core to the far wing (Fig. 5 (pdf 6) of Rouppe van der Voort et al. 2009). The same likely happens for these active-plage fibrils, as for the active-network fibrils in the data of Rutten & Rouppe van der Voort (2017) analyzed in Rutten et al. (2019). Blinking the inset against minimum shift (p7) confirms that the short dark blueshifted features there are part of these. The Dopplershift features of the spot flare show heating here, also on the other side of the spot.

He I D₃ – He II 304 Å (p9–p10): the He I D₃ equivalent-width image is naturally very noisy but nevertheless intriguing. The two scenes show fair bright-bright correspondence, better further away from the spot and not 1:1. The proposed mechanism that He I D₃ obtains opacity by He I photoionization from irradiation by hotter overlying gas, often invoked to explain coronal-hole visibility in optical He I lines (in particular more opaque He I 10830 Å), is therefore not the whole story. Furthermore,

denser MC clustering.¹⁰⁰ I also wonder whether or how upward

this blink shows significant feature shifts, also in the inset, for the bright beginnings of dark fibrils; they occur further out from network in 304 Å whereas the He I D₃-bright parts remain co-located with corresponding $H\alpha$ features. These offsets suggest outwardly increasing heating as occurs for network RBEs in the bottom panels of fig. 6 (pdf 8) of Sekse et al. (2012), here for fatter fibrils originating from plage. This blink also indicates that the 304 Å dark filaments are also present in He I D₃, barely outlined by showing slightly less noise.

304 Å (p10): blinking against $H\alpha$ core I (p6), $H\alpha$ core width (p8) and He I D₃ equivalent width (p9) are all interesting. The p6–p10 blink shows coarse similarity between $H\alpha$ and 304 Å: active chromosphere roughly corresponds between these diagnostics, opposite in sign to the reversed- $H\alpha$ –304 Å correlation for quiet closed-field chromosphere (note 84). The correlation improves with spatial and temporal averaging (options in showex). I have used this likeness for direct co-alignment of $H\alpha$ to AIA 304 Å for SST targets with much activity and many active-region filaments and it became an option in my alignment pipeline (note 87), but almost always alignment of quiet-area AIA 304 Å to HMI magnetograms plus SST alignment to HMI per granulation works better.

171 Å (p11): obviously mostly corona, no chromosphere. Blinking to HMI Stokes I (p1) shows that all long loops connect spot areas. The mossy patches near image center correspond to bright areas in both He diagnostics (p9 and p10); in $H\alpha$ (p6) these may harbor dynamic fibrils but their identification needs a time sequence. Otherwise, the grainy areas of chromospheric plage heating in $H\alpha$ width (p8) show no coronal counterpart. The separation between chromospheric and coronal heating in quiet closed-field areas is already striking (note 86); here it extends to an active region. Some thick 304 Å filament parts are also dark in 171 Å, suggesting bound-free scattering as in note 35.

¹⁰⁰ *Around and upward heating in network and plage.* In quiet areas dark fibrillar $H\alpha$ canopies and similar-pattern but bright He II 304 Å canopies are made by spicules-II extending from network (note 85). Active areas show similar but denser, fatter, longer $H\alpha$ fibril canopies (pdf 6) that are relatively dark in 304 Å (pdf 10). It seems likely that such active canopies stem from similar mechanisms as quiet canopies; I call these “around heating”. However, in active regions there is much grainy heating in the hearts of plage and network, especially where mostly unipolar, that I call “upward heating” (meaning at chromospheric heights, not high-reaching as coronal plumes in coronal holes as in Wang et al. 1997). *$H\alpha$ core-width* (pdf 8) shows remarkable difference: grainy bright upward heating in the plage hearts versus around heating as extended bushes pointing away from network and plage that seem comparable to spicule-II onsets (note 99). I attribute this difference to MC clustering and upward field forcing. Active network and plage contain discrete MCs in larger number and at larger density than quiet network. In classic magnetostatic fluxtube cartoons [SSX (pdf 44)] the field flares out with height; in classic “Zürich wineglass” models (Fig. 4 (pdf 6) of Bünte et al. 1993) neighboring fluxtubes inhibit flaring wide. Denser near-unipolar collections so have more upward field, as in the simulation-assisted inversion map in Fig. 7 (pdf 9) of Jafarzadeh et al. (2017). I suggest that the resulting dominance of upward heating over around heating causes larger brightness in 304 Å, outshining the surrounding fibril canopies that then appear dark in byte-scaled comparison. Instead, where plage and network are more bipolar they have small-scale short-loop connectivity leading to moss appearance (note 98). For both around and upward heating the driving mechanisms are not known,

chromosphere heating in the hearts of active network and plage contributes to the slow wind FIP composition bias.¹⁰¹

The second display I link to is an appetizer for things hopefully to come: comparable active regions in $H\alpha$ and $Ly\alpha$.¹⁰²

as is the case for spicules-II producing canopies around quiet network in closed-field areas (fewer in coronal holes, Fig. 42 (pdf 59) of Rutten 2020). However, also for quiet canopies there is also already inclination dichotomy between more horizontal and more vertical. On-disk RBEs and RREs are easiest detected in the $H\alpha$ wings when they reach far out from their launching network, preferentially showing wide-spread around heating, but at the limb spicules-II are easiest noted and isolated amid their projective confusion when they are more upward, as shown in the inclination histograms in Fig. 4 (pdf 5) of Pereira et al. (2012) and seen near the limb e.g., in this DOT straw movie and in Fig. 5 (pdf 5) of De Pontieu et al. (2012). Hence distinction between around versus upward morphology and heating is gradual, suggesting similar driving but difference in appearance and detectability set by variation in dominating field topography defined by MC clustering density and polarity. For He I D₃ the sparse and very minor on-disk presence in the blinker (pdf 9) versus its bright Balmer-like prominence in the flash spectrum, also away from active regions, suggests sensitive response to upward network and plage heating.

¹⁰¹ *FIP effect.* Significant offset between fast-and slow-wind composition for the photospheric electron-donor elements Fe, Si and Mg with first ionization “potential” below 10 eV which are predominantly ionized where H and hence the gas are near-neutral (Fig. 7 (pdf 11) of von Steiger & Geiss 1989). It is generally attributed to ion-neutral fractionation involving the degree of line-tying and hence attributed to low-atmosphere origins (e.g., von Steiger & Geiss 1989; cf. Laming et al. 2019). The IRIS study of Polito et al. (2020) points to non-mossy upward active-region heating in slow-wind generation (note 100).

¹⁰² *Ly α dream.* Let me dream further re imaging spectroscopy in $Ly\alpha$ (note 41; paradise: 5×5 arcmin field, 0.1 arcsec resolution, 20 wavelengths all at 1 s cadence) and compare that with what we see (awake) with SST/CRISP in $H\alpha$, recapitulating results above. The lines are both H I α and even share the $n=2$ level but differ tremendously. Any feature visible in $H\alpha$ has much higher opacity in $Ly\alpha$ that will only show its outer surface. Within hot and dense features as internetwork shocks, dynamic fibrils, spicules-II, EBs and EB-like lower-atmosphere reconnection sites $Ly\alpha$ has fast collision-up rates [SSX (pdf 166)] while remaining boxed-in even though being champion resonance scatterer [many random steps but of small length [SSX (pdf 90)]]. The very high radiative 1–2 up and down rates then nearly cancel to net radiative rate zero [SSX (pdf 165)], the $n=2$ level gains near-Boltzmann population, $Ly\alpha$ has $S^l_{\nu} \approx B_{\nu}(T)$ and $H\alpha$ has SB line extinction. $H\alpha$ does not show such features in its core when they are underneath the opaque $H\alpha$ fibril canopies spreading from network and then samples them only in its outer wings, bright for EBs but Doppler-shifted thermally-broadened dark for spicule-II RBEs and RREs. $H\alpha$ also skips internetwork shocks by its opacity chasm in the upper photosphere (note 70, [SSX (pdf 91)]). $Ly\alpha$ does not have such gap so that shifting my narrow dream passband from core to wing means sampling the whole non-coronal atmosphere down to the low [dark] photosphere (first plot of [SSX (pdf 90)]). In addition, it is the worst PRD line in the spectrum (second plot of [SSX (pdf 90)]) but this is actually a boon because it gives each part of the line its own source function and response, much as in the [SSF (pdf 111)] cartoon, and hence specific surface-sampling signature in the dream-resolved emergent profile. At each wavelength the emergent intensity does not sample the LTE source function within hot and dense features but the outer monofrequent $\sqrt{\epsilon_{\nu}}$ scattering decline at the $\tau_{\nu} \approx 1$ feature surface. [Ca II H&K are richer in sampling chromospheric canopies than $H\alpha$, as in Fig. 2 (pdf 5) of Jafarzadeh et al. (2017) and in Fig. 3

in Fig. 2 (pdf 6) of Rutten (2017b).¹⁰³ It is amazing how these scenes, both sampling hydrogen atoms, differ in appearance, I think with bright $Ly\alpha$ grains showing dynamic heating and dark $H\alpha$ fibrils showing NLT cooling.¹⁰⁴ ALMA samples hydrogen ions and may be able to measure both types of feature at fast enough cadence to establish and correlate cause–effect delays.¹⁰⁵

Finally, there are dark filaments in these active-region scenes suggesting “chromospheric” neutral hydrogen gas in the corona. Filaments generally appear long-lived but may nevertheless be made dynamically.¹⁰⁶ At high resolution and fast cadence ALMA may also diagnose their formation including frequent refurbishment.

(pdf 4) of Bose et al. (2019) partly thanks to such PRD source function splitting but also because thermal broadening is less wide for heavier atoms.] Hot and dense features may cause $Ly\alpha$ wing brightness that even contributes profile-summed brightness.

¹⁰³ *Ly α images.* The $Ly\alpha$ image is from the VAULT-II flight (Korndyke et al. 2001, Vourlidas et al. 2010, Patsourakos et al. 2007) and is one of 17 images near disk center. A second sequence of four limb images was analyzed by Koza et al. (2009) and assembled into a limb movie and a centerward movie.

¹⁰⁴ *Ly α features.* The VAULT-II limb movie and centerward movie show dense bright grains in plage and active region of which a few change already during the 51-s movies. Koza et al. (2009) suggested that these are $Ly\alpha$ counterparts to $H\alpha$ dynamic fibrils (note 78). The dense more stable grains seem tips of longer-lived upward heating jets that may also produce the numerous bright grains in non-mossy hearts of network and plage in the IBIS $H\alpha$ core-width scene (pdf 8) and contribute the upward chromosphere heating of note 100. Away from the bright-grain plage areas in the $Ly\alpha$ panel of Fig. 2 (pdf 6) the emission blobs are fuzzier and appear remarkably as the short bright bushes extending towards internetwork in the core-width display (pdf 8), suggesting that they sample similar spicule-II-like roundabout heating onsets. The dense non-E $H\alpha$ fibril canopies in the lefthand panel of Fig. 2 (pdf 6) of Rutten (2017b) and in the IBIS $H\alpha$ image (pdf 6) appear dark not from sampling temperature but from $H\alpha$ ’s self-made $\sqrt{\epsilon}$ scattering decline ([SSX (pdf 91)], note 76), darker at larger non-E overopacity of cooling recombining hydrogen. These canopies must be yet more opaque in $Ly\alpha$ with $S^l \approx b_2 B(T)$ superthermal internal source function boosting but similarly sampling the monochromatic $\sqrt{\epsilon}$ $Ly\alpha$ declines towards the canopy surface, as suggested by dark quieter areas in Fig. 2 (pdf 6) of Rutten (2017b) where they are not outradiated by brighter features in profile-summed brightness. The same applies to filaments. [Wake-up caveat: numerical simulations may reproduce non-E canopies and filaments in $Ly\alpha$ only if they also do so properly for $H\alpha$, including spicules-II, filament disruptions, cooling non-E aftermaths.]

¹⁰⁵ *Rydberg H I candidate for ALMA.* There may even exist chromospheric features with sufficient Rydberg-ladder (note 77) NLT recombination emissivity for visibility in the H I 30- α line at 231.901 GHz. The predictions of Carlsson & Rutten (1992) together with α -line observations in Fig. 6 (pdf 5) of Clark et al. (2000) suggested no visibility even at the limb for H I- α lines above $n \approx 25$ but our predictions were for the MACKKL star assuming SE. The expected NLT overextinction of the H I top may make 30- α both higher-formed and visible, and then enable exciting measurement of chromospheric Zeeman splitting which scales with wavelength (Sect. 6 (pdf 13) of Rutten 2017a).

¹⁰⁶ *Filament blobs.* The SST/SOUP $H\alpha$ movie of note 78 shows an active-region filament where small bright bullet-like blobs run intermittently along its length (Lin et al. (2012)). Since then I have noted many such fast disturbances running through filaments in AIA 304 Å movies, suggesting frequent ionization-recombination cycling with NLT opacity enhancement. I speculate that they are not disturbances but actually make filaments and also cause the extraordinary He I D₃-like off-limb visibility of prominences in $H\alpha$ and He II 304 Å.

9. Conclusion

Understanding the solar spectrum has come a long way but isn't there yet. The basic physics was well understood by the 1970s – no dark matter nor dark energy in the solar atmosphere.¹⁰⁷ Numerical modeling started about then with the advent of electronic computing which was welcome because analytic theory had reached its limit in Kourganoff (1952). Numerical study provided great insights even though initially mostly within the misleading straitjacket of plane-parallel atmospheres. Nowadays the major challenge is to obtain realistic spectrum synthesis from realistic solar-atmosphere simulations to provide guidance to interpret high-quality observations conveying solar truth – with the proviso that “simulations are great tools but still toys” (Martínez-Sykora). Full 3D(t) synthesis of all spectral features for every voxel at all times of a RADYN-style 3D(t) MHD-etc simulation is a bridge too far, so that the simulation synthesis frontier lies in clever shortcuts (reviews by Pereira 2019 and Leenaarts 2020).

Shortcuts as adopting 1.5D columnar synthesis ignoring non-radial matter and radiation gradients, Holweger-style “inversion” with NLTE masking, neglect of NLTE ultraviolet scattering and neglect of NLT memory by assuming SE may be as misleading as believing plane-parallel models – but just as those they may be educational steps along the way.

The tantalizing trophy is spectral understanding of the chromosphere which I now define as the hectic domain separating dense near-LTE near-neutral photospheric gas and tenuous near-CE ionized coronal gas, where hydrogen intermittently ionizes and recombines cycling between neutral and plasma state with full NLS – NLW – NLT and HD ↔ MHD ↔ plasma complexity. I repeat: *the chromosphere ain't stacked in layers but is dynamically structured and unstuck in time*. The lowest-hanging fruit is spicule-II heating of quiet chromosphere, then moss, the FIP effect a ripening plum, the Wilson-Bappu effect overdue. However, 150⁺ years since Lockyer (1868) coined “chromosphere” we Khayyam-wise have no explanation for his bright yellow “helios” line.

Every aspect treated here must be considered: the Sun is a most beautiful complex being. We are fortunate that our kind star offers such great inspiring complexity to keep us on our toes.

Acknowledgements. I thank Ram Ajor Maurya and M.K. Ravi Varma for inviting me to teach this subject which I learned initially from C. (Kees) de Jager who became my lifelong example; the second arXiv post celebrates his 100th birthday. I enjoyed my teaching sessions but suspect that the students came out by the same door as in they went [SSF (pdf 120)]. Earlier invitations to teach, in Bandung, Mitaka, Palo Alto, Seoul, La Laguna, Freiburg, Newcastle and Weihai (usually a full week for this material) led to displays SSF and SSX; I hope more will come in a post-covid future. I also thank the organizers for requesting this writeup and endorsing hyperlinks. F. Paletou, J. Leenaarts, T.M.D. Pereira and P.R. Young contributed improvements. As always I relied much on ADS. ADS also taught me pdf page opening and kept my older links active in its 2019 revamp. M.J. Rutten started hosting robrutten.nl for link speed and persistence.

Version history

March 3, 2021 – initial pre-school arXiv post.

April 29, 2021 – second arXiv post: more content, more links, faster serving.

References

Al, N., Bendlin, C., Hirzberger, J., Kneer, F., & Trujillo Bueno, J. 2004, A&A, 418, 1131 ADS
Ando, H. & Osaki, Y. 1975, PASJ, 27, 581 ADS

Antolin, P. & Rouppe van der Voort, L. 2012, ApJ, 745, 152 ADS
Antolin, P., Vissers, G., Pereira, T. M. D., Rouppe van der Voort, L., & Scullion, E. 2015, ApJ, 806, 81 ADS
Asplund, M., Grevesse, N., Sauval, A. J., & Scott, P. 2009, ARA&A, 47, 481 ADS
Athay, R. G. & Skumanich, A. 1967, AJ, 72, 784 ADS
Athay, R. G. & Thomas, R. N. 1961, Physics of the solar chromosphere ADS
Auer, L. H. & Mihalas, D. 1969a, ApJ, 156, 157 ADS
Auer, L. H. & Mihalas, D. 1969b, ApJ, 156, 681 ADS
Avrett, E., Tian, H., Landi, E., Curdt, W., & Wülser, J. P. 2015, ApJ, 811, 87 ADS
Avrett, E. H. 1965, SAO Special Report, 174, 101 ADS
Avrett, E. H. & Loeser, R. 1992, in Astron. Soc. Pacific Conf. Ser., Vol. 26, Cool Stars, Stellar Systems, and the Sun, ed. M. S. Giampapa & J. A. Bookbinder, 489 ADS
Avrett, E. H. & Loeser, R. 2008, ApJS, 175, 229 ADS
Ayres, T. R. 1979, ApJ, 228, 509 ADS
Barklem, P. S., Piskunov, N., & O'Mara, B. J. 2000, VizieR Online Data Catalog, J/A+AS/142/467 ADS
Baschek, B., Holweger, H., & Traving, G. 1966, Astronomische Abhandlungen der Hamburger Sternwarte, 8, 26 ADS
Beck, C., Bellot Rubio, L. R., Schlichenmaier, R., & Sütterlin, P. 2007, A&A, 472, 607 ADS
Beckers, J. M. 1964, PhD thesis, Sacramento Peak Observatory, Air Force Cambridge Research Laboratories, Mass., USA ADS
Beckers, J. M. 1968, SoPh, 3, 367 ADS
Belluzzi, L., Trujillo Bueno, J., & Landi Degl'Innocenti, E. 2007, ApJ, 666, 588 ADS
Berger, T. E., de Pontieu, B., Fletcher, L., et al. 1999a, SoPh, 190, 409 ADS
Berger, T. E., De Pontieu, B., Schrijver, C. J., & Title, A. M. 1999b, ApJL, 519, L97 ADS
Bonnet, R. M. 1996, SoPh, 169, 233 ADS
Bose, S., Henriques, V. M. J., Joshi, J., & Rouppe van der Voort, L. 2019, A&A, 631, L5 ADS
Bostanci, Z. F. & Al Erdogan, N. 2010, MmSAI, 81, 769 ADS
Brandt, P. N., Rutten, R. J., Shine, R. A., & Trujillo Bueno, J. 1994, in NATO Advanced Science Institutes (ASI) Series C, Vol. 433, Solar and stellar magnetism, ed. R. J. Rutten & C. J. Schrijver, 251 ADS
Brault, J. & Noyes, R. 1983, ApJL, 269, L61 ADS
Bruls, J. H. M. J., Rutten, R. J., & Shchukina, N. G. 1992, A&A, 265, 237 ADS
Büntje, M., Solanki, S. K., & Steiner, O. 1993, A&A, 268, 736 ADS
Burgess, A. 1964, ApJ, 139, 776 ADS
Canfield, R. C. 1971a, A&A, 10, 54 ADS
Canfield, R. C. 1971b, A&A, 10, 64 ADS
Cannon, C. J. 1973, ApJ, 185, 621 ADS
Carlsson, M. 1986, Uppsala Astronomical Observatory Reports, 33 ADS
Carlsson, M., De Pontieu, B., & Hansteen, V. H. 2019, ARA&A, 57, 189 ADS
Carlsson, M., Hansteen, V. H., Gudiksen, B. V., Leenaarts, J., & De Pontieu, B. 2016, A&A, 585, A4 ADS
Carlsson, M. & Rutten, R. J. 1992, A&A, 259, L53 ADS
Carlsson, M., Rutten, R. J., & Shchukina, N. G. 1992, A&A, 253, 567 ADS
Carlsson, M. & Stein, R. F. 1994, in Chromospheric Dynamics, ed. M. Carlsson, 47 ADS
Carlsson, M. & Stein, R. F. 1995, ApJL, 440, L29 ADS
Carlsson, M. & Stein, R. F. 1997, ApJ, 481, 500 ADS
Carlsson, M. & Stein, R. F. 2002, ApJ, 572, 626 ADS
Castor, J. I. 2007, Radiation Hydrodynamics ADS
Cauzzi, G. & Reardon, K. 2012, IAU Special Session, 6, E5.11 ADS
Cauzzi, G., Reardon, K., Rutten, R. J., Tritschler, A., & Uitenbroek, H. 2009, A&A, 503, 577 ADS
Cayrel, R. & Steinberg, M., eds. 1976, Physique des Mouvements dans les Atmosphères Stellaires ADS
Chae, J. 2014, ApJ, 780, 109 ADS
Clark, T. A., Naylor, D. A., & Davis, G. R. 2000, A&A, 357, 757 ADS
Cram, L. E. & Damé, L. 1983, ApJ, 272, 355 ADS
Cram, L. E., Rutten, R. J., & Lites, B. W. 1980, ApJ, 241, 374 ADS
da Silva Santos, J. M., de la Cruz Rodríguez, J., White, S. M., et al. 2020, A&A, 643, A41 ADS
Danilovic, S. 2017, A&A, 601, A122 ADS
de Pontieu, B., Berger, T. E., Schrijver, C. J., & Title, A. M. 1999, SoPh, 190, 419 ADS
De Pontieu, B., Carlsson, M., Rouppe van der Voort, L. H. M., et al. 2012, ApJL, 752, L12 ADS
De Pontieu, B., Hansteen, V. H., Rouppe van der Voort, L., van Noort, M., & Carlsson, M. 2007, ApJ, 655, 624 ADS
de Pontieu, B., McIntosh, S., Hansteen, V. H., et al. 2007, PASJ, 59, S655 ADS
De Pontieu, B., McIntosh, S. W., Carlsson, M., et al. 2007, Science, 318, 1574 ADS
De Pontieu, B., Tarbell, T., & Erdélyi, R. 2003, ApJ, 590, 502 ADS
De Wijn, A. G., De Pontieu, B., & Rutten, R. J. 2007, ApJ, 654, 1128 ADS

¹⁰⁷ For a conflicting speculation search ADS with *abs: "axion quark" and "solar orbiter"* – amusing but not honorable by labeling, naming, citation.

- del Toro Iniesta, J. C. 2007, Introduction to Spectropolarimetry [ADS](#)
- Del Zanna, G. & Mason, H. E. 2018, *Liv. Rev. Solar Phys.*, 15, 5 [ADS](#)
- Dere, K. P. 2007, *A&A*, 466, 771 [ADS](#)
- Deubner, F.-L. 1972, *SoPh*, 22, 263 [ADS](#)
- Deubner, F. L. 1975, *A&A*, 44, 371 [ADS](#)
- Deubner, F. L. & McIntyre, 1976, in *Physique des Mouvements dans les Atmospheres*, ed. R. Cayrel & M. Steinberg, 259 [ADS](#)
- Doyle, J. G., Jevremović, D., Short, C. I., et al. 2001, *A&A*, 369, L13 [ADS](#)
- Dunn, R. B., Evans, J. W., Jefferies, J. T., et al. 1968, *ApJS*, 15, 275 [ADS](#)
- Eddington, A. S. 1929, *MNRAS*, 89, 620 [ADS](#)
- Eklund, H., Wedemeyer, S., Snow, B., et al. 2021, *Phil. Trans. Royal Soc. London A*, 379, 20200185 [ADS](#)
- Ellerman, F. 1917, *ApJ*, 46, 298 [ADS](#)
- Falconer, D. A., Moore, R. L., Porter, J. G., & Hathaway, D. H. 1998, *ApJ*, 501, 386 [ADS](#)
- Feautrier, P. 1964, *Comptes Rendus Academie des Sciences (serie non specifiée)*, 258, 3189 [ADS](#)
- Fokker, A. D. & Rutten, R. J. 1967, *Bull. Astr. Inst. Neth.*, 19, 254 [ADS](#)
- Fontenla, J. M., Avrett, E. H., & Loeser, R. 1993, *ApJ*, 406, 319 [ADS](#)
- Fontenla, J. M., Curdt, W., Haberleiter, M., Harder, J., & Tian, H. 2009, *ApJ*, 707, 482 [ADS](#)
- Fontenla, J. M., Stancil, P. C., & Landi, E. 2015, *ApJ*, 809, 157 [ADS](#)
- Fossum, A. & Carlsson, M. 2005a, *Nat*, 435, 919 [ADS](#)
- Fossum, A. & Carlsson, M. 2005b, *ApJ*, 625, 556 [ADS](#)
- Fossum, A. & Carlsson, M. 2006, *ApJ*, 646, 579 [ADS](#)
- Frogner, L., Gudiksen, B. V., & Bakke, H. 2020, *A&A*, 643, A27 [ADS](#)
- Froment, C., Antolin, P., Henriques, V. M. J., Kohutova, P., & Rouppe van der Voort, L. H. M. 2020, *A&A*, 633, A11 [ADS](#)
- Gingerich, O. & de Jager, C. 1968, *SoPh*, 3, 5 [ADS](#)
- Gingerich, O., Noyes, R. W., Kalkofen, W., & Cuny, Y. 1971, *SoPh*, 18, 347 [ADS](#)
- Giovannelli, R. G. 1967, *Australian Journal of Physics*, 20, 81 [ADS](#)
- Goldberg, L. 1964, *ApJ*, 140, 384 [ADS](#)
- Goldberg, L. & Noyes, R. W. 1964, *AJ*, 69, 542 [ADS](#)
- Golding, T. P., Leenaarts, J., & Carlsson, M. 2017, *A&A*, 597, A102 [ADS](#)
- Gray, D. F. 1977, *ApJ*, 218, 530 [ADS](#)
- Gray, D. F. 1992, *The Observation and Analysis of Stellar Photospheres*. (2nd edition, Cambridge University Press) [ADS](#)
- Gray, D. F. 2005, *The Observation and Analysis of Stellar Photospheres* (3rd edition, Cambridge University Press) [ADS](#)
- Greve, A. & Zwaan, C. 1980, *A&A*, 90, 239 [ADS](#)
- Grottrian, W. 1931, *Z. Astrophys.*, 3, 199 [ADS](#)
- Gudiksen, B. V., Carlsson, M., Hansteen, V. H., et al. 2011, *A&A*, 531, A154 [ADS](#)
- Hansteen, V. H., De Pontieu, B., Rouppe van der Voort, L., van Noort, M., & Carlsson, M. 2006, *ApJL*, 647, L73 [ADS](#)
- Heeck, J. 2013, *Phys. Rev. Lett.*, 111, 021801 [ADS](#)
- Heinzel, P., Gunár, S., & Anzer, U. 2015, *A&A*, 579, A16 [ADS](#)
- Heinzel, P., Mein, N., & Mein, P. 1999, *A&A*, 346, 322 [ADS](#)
- Henriques, V. M. J., Kuridze, D., Mathioudakis, M., & Keenan, F. P. 2016, *ApJ*, 820, 124 [ADS](#)
- Hines, C. O. 1960, *Canadian Journal of Physics*, 38, 1441 [ADS](#)
- Holweger, H. 1967, *Z. Astrophys.*, 65, 365 [ADS](#)
- Holweger, H. & Müller, E. A. 1974, *SoPh*, 39, 19 [ADS](#)
- House, L. L. 1964, *ApJS*, 8, 307 [ADS](#)
- Houtgast, J. 1942, PhD thesis, - [ADS](#)
- Hubený, I. 1987a, *A&A*, 185, 336 [ADS](#)
- Hubený, I. 1987b, *A&A*, 185, 332 [ADS](#)
- Hubený, I. & Mihalas, D. 2014, *Theory of Stellar Atmospheres* (Princeton: Princeton University Press) [ADS](#)
- Jafarzadeh, S., Rutten, R. J., Solanki, S. K., et al. 2017, *ApJS*, 229, 11 [ADS](#)
- Jefferies, J. T. 1968, *Spectral line formation* (Waltham: Blaisdell) [ADS](#)
- Jefferies, J. T. & Thomas, R. N. 1959, *ApJ*, 129, 401 [ADS](#)
- Jejčić, S. & Heinzel, P. 2009, *SoPh*, 254, 89 [ADS](#)
- Jordan, C. 1969, *MNRAS*, 142, 501 [ADS](#)
- Joshi, J., Rouppe van der Voort, L. H. M., & de la Cruz Rodríguez, J. 2020, *A&A*, 641, L5 [ADS](#)
- Kato, Y., Steiner, O., Steffen, M., & Suematsu, Y. 2011, *ApJL*, 730, L24 [ADS](#)
- Keller, C. U. & von der Lühe, O. 1992, *A&A*, 261, 321 [ADS](#)
- Korendyke, C. M., Vourlidas, A., Cook, J. W., et al. 2001, *SoPh*, 200, 63 [ADS](#)
- Kostik, R., Khomenko, E., & Shchukina, N. 2009, *A&A*, 506, 1405 [ADS](#)
- Kostik, R. I. & Orlova, T. V. 1975, *SoPh*, 45, 119 [ADS](#)
- Kostik, R. I., Shchukina, N. G., & Rutten, R. J. 1996, *A&A*, 305, 325 [ADS](#)
- Kourganoff, V. 1952, *Basic methods in transfer problems; radiative equilibrium and neutron diffusion* (Oxford: Clarendon Press) [ADS](#)
- Koza, J., Rutten, R. J., & Vourlidas, A. 2009, *A&A*, 499, 917 [ADS](#)
- Krijger, J. M., Rutten, R. J., Lites, B. W., et al. 2001, *A&A*, 379, 1052 [ADS](#)
- Kurucz, R. L. 2009, in *Am. Inst. Phys. Conf. Series*, ed. I. Hubený, J. M. Stone, K. MacGregor, & K. Werner, Vol. 1171, 43–51 [ADS](#)
- Labs, D. & Neckel, H. 1972, *SoPh*, 22, 64 [ADS](#)
- Lambert, J., Paletou, F., Josselin, E., & Glorian, J.-M. 2016, *European Journal of Physics*, 37, 015603 [ADS](#)
- Laming, J. M., Vourlidas, A., Korendyke, C., et al. 2019, *ApJ*, 879, 124 [ADS](#)
- Landi Degl'Innocenti, E. & Landolfi, M. 2004, *Polarization in Spectral Lines*, Vol. 307 [ADS](#)
- Leenaarts, J. 2020, *Liv. Rev. Solar Phys.*, 17, 3 [ADS](#)
- Leenaarts, J. & Carlsson, M. 2009, in *Astron. Soc. Pacific Conf. Ser.*, Vol. 415, *The Second Hinode Science Meeting: Beyond Discovery-Toward Understanding*, ed. B. Lites, M. Cheung, T. Magara, J. Mariska, & K. Reeves, 87 [ADS](#)
- Leenaarts, J., Carlsson, M., Hansteen, V., & Rutten, R. J. 2007, *A&A*, 473, 625 [ADS](#)
- Leenaarts, J., Carlsson, M., & Rouppe van der Voort, L. 2012a, *ApJ*, 749, 136 [ADS](#)
- Leenaarts, J., Pereira, T., & Uitenbroek, H. 2012b, *A&A*, 543, A109 [ADS](#)
- Leenaarts, J., Rutten, R. J., Reardon, K., Carlsson, M., & Hansteen, V. 2010, *ApJ*, 709, 1362 [ADS](#)
- Leighton, R. B., Noyes, R. W., & Simon, G. W. 1962, *ApJ*, 135, 474 [ADS](#)
- Lemke, M. & Holweger, H. 1987, *A&A*, 173, 375 [ADS](#)
- Lighthill, M. J. 1967, in *Aerodynamic Phenomena in Stellar Atmospheres*, ed. R. N. Thomas, Vol. 28, 429 [ADS](#)
- Lin, Y., Engvold, O., & Rouppe van der Voort, L. H. M. 2012, *ApJ*, 747, 129 [ADS](#)
- Linsky, J. L. & Avrett, E. H. 1970, *PASP*, 82, 169 [ADS](#)
- Lites, B., ed. 1985, *Chromospheric Diagnostics and Modelling*, Sacramento Peak Workshop, Sunspot, August 1984 [ADS](#)
- Lites, B. W., Rutten, R. J., & Kalkofen, W. 1993, *ApJ*, 414, 345 [ADS](#)
- Liu, S. Y. & Skumanich, A. 1974, *SoPh*, 38, 109 [ADS](#)
- Livingston, W., Wallace, L., White, O. R., & Giampapa, M. S. 2007, *ApJ*, 657, 1137 [ADS](#)
- Lockyer, J. N. 1868, *Proceedings of the Royal Society of London Series I*, 17, 131 [ADS](#)
- Madjarska, M. S. 2019, *Liv. Rev. Solar Phys.*, 16, 2 [ADS](#)
- Madjarska, M. S., Chae, J., Moreno-Insertis, F., et al. 2021, *A&A*, 646, A107 [ADS](#)
- Malanushenko, O., Jones, H. P., & Livingston, W. 2004, in *Multi-Wavelength Investigations of Solar Activity*, ed. A. V. Stepanov, E. E. Benevolenskaya, & A. G. Kosovichev, Vol. 223, 645–646 [ADS](#)
- Maltby, P., Avrett, E. H., Carlsson, M., et al. 1986, *ApJ*, 306, 284 [ADS](#)
- Martens, P. C. H., Kankelborg, C. C., & Berger, T. E. 2000, *ApJ*, 537, 471 [ADS](#)
- Mein, N., Mein, P., Heinzel, P., et al. 1996, *A&A*, 309, 275 [ADS](#)
- Mein, P. 1966, *Annales d'Astrophysique*, 29, 153 [ADS](#)
- Meyer, K. A., Mackay, D. H., & van Ballegooijen, A. A. 2012, *SoPh*, 278, 149 [ADS](#)
- Mihalas, D. 1970, *Stellar atmospheres* (San Francisco: W. H. Freeman and Co) [ADS](#)
- Mihalas, D. 1978, *Stellar atmospheres*, 2nd edition (San Francisco: W. H. Freeman and Co) [ADS](#)
- Minnaert, M. 1930, *Z. Astrophys.*, 1, 209 [ADS](#)
- Minnaert, M., Houtgast, J., & Mulders, G. F. W. 1940, *Photometric atlas of the solar spectrum* (Sterrewacht "Sonnenborgh", Utrecht) [ADS](#)
- Molnar, M. E., Reardon, K. P., Chai, Y., et al. 2019, *ApJ*, 881, 99 [ADS](#)
- Molowny-Horas, R., Heinzel, P., Mein, P., & Mein, N. 1999, *A&A*, 345, 618 [ADS](#)
- Moore, C. E., Minnaert, M. G. J., & Houtgast, J. 1966, *The solar spectrum 2935 Å to 8770 Å* (NBS) [ADS](#)
- Ng, K. C. 1974, *J. Chem. Phys.*, 61, 2680 [ADS](#)
- Nordlund, Å., Stein, R. F., & Asplund, M. 2009, *Liv. Rev. Solar Phys.*, 6, 2 [ADS](#)
- Novotny, E. 1973, *Introduction to stellar atmospheres and interiors* (Oxford University Press) [ADS](#)
- Noyes, R. W. 1965, *SAO Special Report*, 174, 405 [ADS](#)
- Olson, G. L., Auer, L. H., & Buchler, J. R. 1986, *J. Quant. Spec. Radiat. Transf.*, 35, 431 [ADS](#)
- Paletou, F. 2018, *Open Astronomy*, 27, 76 [ADS](#)
- Patsourakos, S., Gouttebroze, P., & Vourlidas, A. 2007, *ApJ*, 664, 1214 [ADS](#)
- Pereira, T. M. D. 2019, *Advances in Space Research*, 63, 1434 [ADS](#)
- Pereira, T. M. D., De Pontieu, B., & Carlsson, M. 2012, *ApJ*, 759, 18 [ADS](#)
- Pereira, T. M. D., De Pontieu, B., Carlsson, M., et al. 2014, *ApJL*, 792, L15 [ADS](#)
- Pereira, T. M. D. & Uitenbroek, H. 2015, *A&A*, 574, A3 [ADS](#)
- Polito, V., De Pontieu, B., Testa, P., Brooks, D. H., & Hansteen, V. 2020, *ApJ*, 903, 68 [ADS](#)
- Pottasch, S. R. 1964, *Space Sci. Rev.*, 3, 816 [ADS](#)
- Reardon, K. & Cauzzi, G. 2012a, in *SDO-4: Dynamics and Energetics of the Coupled Solar Atmosphere. The Synergy Between State-of-the-Art Observations and Numerical Simulations*, 20 [ADS](#)
- Reardon, K. P. & Cauzzi, G. 2012b, in *Am. Astr. Soc. Meeting Abstracts*, Vol. 220, 201.11 [ADS](#)
- Rouppe van der Voort, L. & de la Cruz Rodríguez, J. 2013, *ApJ*, 776, 56 [ADS](#)
- Rouppe van der Voort, L., Leenaarts, J., de Pontieu, B., Carlsson, M., & Vissers, G. 2009, *ApJ*, 705, 272 [ADS](#)

- Roupe van der Voort, L. H. M., De Pontieu, B., Hansteen, V. H., Carlsson, M., & van Noort, M. 2007, *ApJL*, 660, L169 [ADS](#)
- Roupe van der Voort, L. H. M., Rutten, R. J., Sütterlin, P., Sloover, P. J., & Krijger, J. M. 2003, *A&A*, 403, 277 [ADS](#)
- Roupe van der Voort, L. H. M., Rutten, R. J., & Vissers, G. J. M. 2016, *A&A*, 592, A100 [ADS](#)
- Rutten, R. J. 1978, *SoPh*, 56, 237 [ADS](#)
- Rutten, R. J. 1988, in *Astrophys. Space Sci. Library*, Vol. 138, IAU Colloq. 94: Physics of Formation of Fe II Lines Outside LTE, ed. R. Viotti, A. Vittone, & M. Friedjung, 185–210 [ADS](#)
- Rutten, R. J. 1990, in *IAU Symposium*, Vol. 138, Solar Photosphere: Structure, Convection, and Magnetic Fields, ed. J. O. Stenflo, 501–516 [ADS](#)
- Rutten, R. J. 1995, in *ESA Special Pub.*, Vol. 376, Helioseismology, ed. J. T. Hoeksema, V. Domingo, B. Fleck, & B. Battick, 151–163 [ADS](#)
- Rutten, R. J. 1999, in *Astron. Soc. Pacific Conf. Series*, Vol. 184, Magnetic Fields and Oscillations, ed. B. Schmieder, A. Hofmann, & J. Staudte, Third Adv. in Solar Physics Euroconf., 181–200 [ADS](#)
- Rutten, R. J. 2002, *J. Astron. Data*, 8, 1 [ADS](#)
- Rutten, R. J. 2006, in *Astron. Soc. Pacific Conf. Series*, Vol. 354, Solar MHD Theory and Observations: A High Spatial Resolution Perspective, ed. J. Leibacher, R. F. Stein, & H. Uitenbroek, 276–283 [ADS](#)
- Rutten, R. J. 2007, in *Astron. Soc. Pacific Conf. Series*, Vol. 368, The Physics of Chromospheric Plasmas, ed. P. Heinzel, I. Dorotovič, & R. J. Rutten, 27–49 [ADS](#)
- Rutten, R. J. 2011, in *Indonesia Astronomy & Astrophysics*, ed. P. W. Premadi & et al. (Institut Teknologi Bandung: Indonesian Astron. Soc.), 3–8
- Rutten, R. J. 2013, in *Astron. Soc. Pacific Conf. Series*, Vol. 470, 370 Years of Astronomy in Utrecht, ed. G. Pugliese, A. de Koter, & M. Wijburg, 49–58 [ADS](#)
- Rutten, R. J. 2016, *A&A*, 590, A124 [ADS](#)
- Rutten, R. J. 2017a, in *IAU Symposium*, Vol. 327, Fine structure and dynamics of the solar atmosphere, ed. S. Vargas Domínguez, A. G. Kosovichev, P. Antolin, & L. Harra, 1–15 [ADS](#)
- Rutten, R. J. 2017b, *A&A*, 598, A89 [ADS](#)
- Rutten, R. J. 2019, *SoPh*, 294, 165 [ADS](#)
- Rutten, R. J. 2020, *arXiv e-prints*, arXiv:2009.00376 [ADS](#)
- Rutten, R. J. & Carlsson, M. 1994, in *IAU Symposium*, Vol. 154, Infrared Solar Physics, ed. D. M. Rabin, J. T. Jefferies, & C. Lindsey, 309–322 [ADS](#)
- Rutten, R. J. & Kostik, R. I. 1982, *A&A*, 115, 104 [ADS](#)
- Rutten, R. J. & Krijger, J. M. 2003, *A&A*, 407, 735 [ADS](#)
- Rutten, R. J., Leenaarts, J., Roupe van der Voort, L. H. M., et al. 2011, *A&A*, 531, A17 [ADS](#)
- Rutten, R. J. & Milkey, R. W. 1979, *ApJ*, 231, 277 [ADS](#)
- Rutten, R. J. & Roupe van der Voort, L. H. M. 2017, *A&A*, 597, A138 [ADS](#)
- Rutten, R. J., Roupe van der Voort, L. H. M., & De Pontieu, B. 2019, *A&A*, 632, A96 [ADS](#)
- Rutten, R. J., Roupe van der Voort, L. H. M., & Vissers, G. J. M. 2015, *ApJ*, 808, 133 [ADS](#)
- Rutten, R. J. & Schrijver, C. J., eds. 1994, *Solar Surface Magnetism*, Procs. Soesterberg workshop, linked contents of NATO ASI Series C 433 [ADS](#)
- Rutten, R. J. & Stencel, R. E. 1980, *A&A Suppl.*, 39, 415 [ADS](#)
- Rutten, R. J. & Uitenbroek, H. 1991, *SoPh*, 134, 15 [ADS](#)
- Rutten, R. J. & Uitenbroek, H. 2012, *A&A*, 540, A86 [ADS](#)
- Rutten, R. J., van Veelen, B., & Sütterlin, P. 2008, *SoPh*, 251, 533 [ADS](#)
- Rutten, R. J., Vissers, G. J. M., Roupe van der Voort, L. H. M., Sütterlin, P., & Vitas, N. 2013, in *J. Physics Conf. Series*, Vol. 440, Eclipse on the Coral Sea: Cycle 24 Ascending, ed. P. S. Cally, R. Erdélyi, & A. A. Norton, 1–13 [ADS](#)
- Rutten, R. J. & Zwaan, C. 1983, *A&A*, 117, 21 [ADS](#)
- Rybicki, G. B. & Hummer, D. G. 1992, *A&A*, 262, 209 [ADS](#)
- Rybicki, G. B. & Lightman, A. P. 1986, *Radiative Processes in Astrophysics* (New York: Wiley), 400 [ADS](#)
- Scharmer, G. B. & Carlsson, M. 1985, *Journal of Computational Physics*, 59, 56 [ADS](#)
- Scharmer, G. B., Löfdahl, M. G., Sliepen, G., & de la Cruz Rodríguez, J. 2019, *A&A*, 626, A55 [ADS](#)
- Schoolman, S. A. 1972, *SoPh*, 22, 344 [ADS](#)
- Sekse, D. H., Roupe van der Voort, L., & De Pontieu, B. 2012, *ApJ*, 752, 108 [ADS](#)
- Sekse, D. H., Roupe van der Voort, L., De Pontieu, B., & Scullion, E. 2013, *ApJ*, 769, 44 [ADS](#)
- Shchukina, N. G., Olshevsky, V. L., & Khomenko, E. V. 2009, *A&A*, 506, 1393 [ADS](#)
- Sheminova, V. A., Rutten, R. J., & Roupe van der Voort, L. H. M. 2005, *A&A*, 437, 1069 [ADS](#)
- Shine, R. A., Milkey, R. W., & Mihalas, D. 1975, *ApJ*, 199, 724 [ADS](#)
- Skogsrud, H., Roupe van der Voort, L., & De Pontieu, B. 2016, *ApJ*, 817, 124 [ADS](#)
- Smitha, H. N., Holzreuter, R., van Noort, M., & Solanki, S. K. 2020, *A&A*, 633, A157 [ADS](#)
- Smitha, H. N., Holzreuter, R., van Noort, M., & Solanki, S. K. 2021, *A&A*, 647, A46 [ADS](#)
- Straus, T., Fleck, B., Jefferies, S. M., et al. 2008, *ApJL*, 681, L125 [ADS](#)
- Suematsu, Y., Wang, H., & Zirin, H. 1995, *ApJ*, 450, 411 [ADS](#)
- Sukhorukov, A. V. & Leenaarts, J. 2017, *A&A*, 597, A46 [ADS](#)
- Sütterlin, P., Rutten, R. J., & Skomorovsky, V. I. 2001, *A&A*, 378, 251 [ADS](#)
- Thomas, R. N. 1957, *ApJ*, 125, 260 [ADS](#)
- Thomas, R. N. 1960, *ApJ*, 131, 429 [ADS](#)
- Title, A. M. 1966, *Selected Spectroheliograms* (Pasadena: Mount Wilson and Palomar Observatories)
- Turck-Chièze, S., Carton, P. H., Barrière, J. C., et al. 2012, in *Astron. Soc. Pacific Conf. Ser.*, Vol. 462, Progress in Solar/Stellar Physics with Helio- and Asteroseismology, ed. H. Shibahashi, M. Takata, & A. E. Lynas-Gray, 240 [ADS](#)
- Tziotziou, K. 2007, in *Astron. Soc. Pacific Conf. Ser.*, Vol. 368, The Physics of Chromospheric Plasmas, ed. P. Heinzel, I. Dorotovič, & R. J. Rutten, 217 [ADS](#)
- Uitenbroek, H. 2000, *ApJ*, 531, 571 [ADS](#)
- Uitenbroek, H. 2001, *ApJ*, 557, 389 [ADS](#)
- Uitenbroek, H. & Bruls, J. H. M. J. 1992, *A&A*, 265, 268 [ADS](#)
- Uitenbroek, H. & Criscuolo, S. 2011, *ApJ*, 736, 69 [ADS](#)
- Ulmschneider, P. & Kalkofen, W. 2003, Heating of the solar chromosphere, ed. B. N. Dwivedi & F. b. E. N. Parker, 181–195 [ADS](#)
- Ulrich, R. K. 1970, *ApJ*, 162, 993 [ADS](#)
- Unruh, Y. C., Solanki, S. K., & Fligge, M. 1999, *A&A*, 345, 635 [ADS](#)
- Unsöld, A. 1955, *Physik der Sternatmosphären* (2. Auflage, Springer) [ADS](#)
- van Noort, M., Roupe van der Voort, L., & Löfdahl, M. G. 2005, *SoPh*, 228, 191 [ADS](#)
- Vernazza, J. E., Avrett, E. H., & Loeser, R. 1976, *ApJS*, 30, 1 [ADS](#)
- Vernazza, J. E., Avrett, E. H., & Loeser, R. 1981, *ApJS*, 45, 635 [ADS](#)
- Vissers, G. J. M., Roupe van der Voort, L. H. M., & Rutten, R. J. 2013, *ApJ*, 774, 32 [ADS](#)
- Vissers, G. J. M., Roupe van der Voort, L. H. M., & Rutten, R. J. 2019, *A&A*, 626, A4 [ADS](#)
- Vissers, G. J. M., Roupe van der Voort, L. H. M., Rutten, R. J., Carlsson, M., & De Pontieu, B. 2015, *ApJ*, 812, 11 [ADS](#)
- Vitas, N., Viticchiè, B., Rutten, R. J., & Vögler, A. 2009, *A&A*, 499, 301 [ADS](#)
- Vitense, E. 1951, *Z. Astrophys.*, 28, 81 [ADS](#)
- Vögler, A., Shelyag, S., Schüssler, M., et al. 2005, *A&A*, 429, 335 [ADS](#)
- von Steiger, R. & Geiss, J. 1989, *A&A*, 225, 222 [ADS](#)
- Vourlidis, A., Sánchez Andrade-Nuño, B., Landi, E., et al. 2010, *SoPh*, 261, 53 [ADS](#)
- Wang, Y. M., Sheeley, N. R., Dere, K. P., et al. 1997, *ApJL*, 484, L75 [ADS](#)
- Watanabe, H., Vissers, G., Kitai, R., Roupe van der Voort, L., & Rutten, R. J. 2011, *ApJ*, 736, 71 [ADS](#)
- Whitaker, W. A. 1963, *ApJ*, 137, 914 [ADS](#)
- White, O. R. & Cha, M. Y. 1973, *SoPh*, 31, 23 [ADS](#)
- Wiersma, J., Rutten, R. J., & Lanz, T. 2003, in *Astron. Soc. Pacific Conf. Series*, Vol. 288, Stellar Atmosphere Modeling, ed. I. Hubeny, D. Mihalas, & K. Werner, 130–136 [ADS](#)
- Wijbenga, J. W. & Zwaan, C. 1972, *SoPh*, 23, 265 [ADS](#)
- Wilson, O. C. & Vainu Bappu, M. K. 1957, *ApJ*, 125, 661 [ADS](#)
- Withbroe, G. L. 1978, *ApJ*, 225, 641 [ADS](#)
- Wolff, C. L. 1972, *ApJL*, 177, L87 [ADS](#)
- Wolff, C. L. 1973, *SoPh*, 32, 31 [ADS](#)
- Young, P. R., Tian, H., Peter, H., et al. 2018, *Space Sci. Rev.*, 214, 120 [ADS](#)
- Zirin, H. & Popp, B. 1989, *ApJ*, 340, 571 [ADS](#)